Ultrafast Photoinduced Electron Transfer in Bimolecular Donor-Acceptor Systems

Dissertation by

Qana Abed Alsulam

In Partial Fulfillment of the Requirements

For the Degree of

Doctor of Philosophy

King Abdullah University of Science and Technology

Thuwal, Kingdom of Saudi Arabia

The dissertation of Qana Abed Alsulami is approved by the examination committee.

Committee Chairperson: Prof. Omar F. Mohammed

Committee Member: Prof. Dongping Zhong

Committee Member: Prof. Osman M. Bakr

Committee Member: Prof. Kazuhiro Takanabe

ABSTRACT

Ultrafast Photoinduced Electron Transfer in Bimolecular Donor-Acceptor Systems

Qana Abed Alsulami

The efficiency of photoconversion systems, such as organic photovoltaic (OPV) cells, is largely controlled by a series of fundamental photophysical processes occurring at the interface before carrier collection. A profound understanding of ultrafast interfacial charge transfer (CT), charge separation (CS), and charge recombination (CR) is the key determinant to improving the overall performances of photovoltaic devices. The discussion in this dissertation primarily focuses on the relevant parameters that are involved in photon absorption, exciton separation, carrier transport, carrier recombination and carrier collection in organic photovoltaic devices. A combination of steady-state and femtosecond broadband transient spectroscopies was used to investigate the photoinduced charge carrier dynamics in various donor-acceptor systems.

Furthermore, this study was extended to investigate some important factors that influence charge transfer in donor-acceptor systems, such as the morphology, energy band alignment, electronic properties and chemical structure. Interestingly, clear correlations among the steady-state measurements, time-resolved spectroscopy results, grain alignment of the electron transporting layer (ETL), carrier mobility, and device

performance are found. In this thesis, we explored the significant impacts of ultrafast charge separation and charge recombination at donor/acceptor (D/A) interfaces on the performance of a conjugated polymer PTB7-Th device with three fullerene acceptors: $PC_{71}BM$, $PC_{61}BM$ and $IC_{60}BA$. Time-resolved laser spectroscopy and high-resolution electron microscopy can illustrate the basis for fabricating solar cell devices with improved performances. In addition, we studied the effects of the incorporation of heavy metals into π-conjugated chromophores on electron transfer by monitoring the triplet state lifetime of the oligomer using transient absorption spectroscopy, as understanding the mechanisms controlling intersystem crossing and photoinduced electron transfer dynamics is required to improve the device performance of solar cells. Here, we evaluated the effects of incorporating Pt(II) on intersystem crossing and photoinduced electron transfer by comparing and analyzing the photoexcited dynamics of DPP-Pt(II)(acac) and metal-free DPP with different acceptors such as TCNE, TMPyP, and TPyP.

ACKNOWLEDGEMENTS

First and foremost, I would like to express my deep and sincere gratitude to my supervisor **Prof. Dr. Omar F. Mohammad**, whose advice, guidance and support from the initial to the final level enabled me to fully understand, develop, and fulfill this study. He has become more than a supervisor to me. Thank you for always believing in me.

My appreciation also goes to **Dr. Shawkat Aly** who has greatly assisted me, and without his effort, my study would have been more difficult. I am greatly indebted to **Dr. Banavoth Murali** who helped me with device characterization and fabrication. I was really fortunate to have the chance to learn various aspects of science from him that I was never taught. Additionally, great thanks to **Dr. Riya Bose** and **Dr. Ahmed El-Zohry** for their suggestions and help. I am really grateful to all of the postdocs and students for their support throughout the years.

My heartfelt gratitude is extended to my husband **Eng. Meshal M. Alsolami** who is one of my biggest supporters for pursuing and achieving my goals in this study. I am very grateful for his understanding of my busy life with a full schedule of research and study. Not only has he supported my PhD, he has become the motivation and energy for me towards bigger dreams and contributions afterward. Thanks for always being there in every step I take.

Finally, my parents siblings, and lovely children **Mohammad**, **Khaled**, **Talal** and **Farah** are the source of my joy and happiness. There is nothing I want in this life other than to make them happy and proud of me. I thank them for their endless love and support.

TABLE OF CONTENTS

LIST OF ABBREVIATIONS

A	acceptor
Abs	absorbance
CR	charge recombination
CS	charge separation
CT	charge transfer
D	donor
DCM	dichloromethane
DMF	dimethylformamide
DPP	diketopyrrolopyrrole
EA	electron affinity
EDA	electron donor-acceptor
ESA	excited state absorption
ETL	electron transporting layer
FAs	fullerene acceptors
FF	fill factor
fs	Femtosecond
GSB	ground state bleach
HTL	hole transporting layer
$IC_{60}BA$	indene-C60 bis-adduct
IP	ionization potential energy

I-V	current-voltage
ISC	intersystem crossing
ITO	tin-doped indium oxide
MLCT	metal-to-ligand charge transfer
NIR	near-infrared
Ns	nanosecond
OD	optical density
OPV	organic photovoltaic
$PC_{61}BM$	phenyl-C61-butyric acid methyl ester
$PC_{71}BM$	[6,6]-phenyl-C71-butyric acid methyl ester
PCE	power conversion efficiency
PET	photoinduced electron transfer
PL	Photoluminescence
ps	Picosecond
PV	Photovoltaic
RT	room temperature
SE	stimulated emission
SEM	scanning electron microscopy
SV	stern-volmer plot
TA	transient absorption
TCNE	tetracyanoethylene
TCSPC	time-correlated single-photon counting

TMPyP	tetra(N-methyl-4-pyridyl)porphyrin tetrachloride
TPyP	tetra(4-pyridyl)porphyrin
TEM	transmission electron microscopy
UV-Vis	Ultraviolet-Visible

LIST OF SYMBOLS

Eg	bandgap
ε	molar absorption coefficient
C	molar concentration
L	optical path length
τ	carrier lifetime
λ	Wavelength
t	Time
µs	microsecond
V_{oc}	open-circuit voltage
I_{sc}	short-circuit current
ϕ_A	work functions for anode
ϕ_C	work functions for cathode
φ_{ISC}	intersystem crossing efficiency
ΔG	Gibbs free energy
ΔA	change in absorption

LIST OF ILLUSTRATIONS

LIST OF TABLE

CHAPTER 1

INTRODUCTION

1.1. Photophysical Processes: An Overview

1.1.1. Photoinduced Electron Transfer

Photoinduced electron transfer (PET) is one of the growing research areas in bimolecular systems. It is motivated primarily by the need for solar energy conversion. In the 20th and 21st centuries, there have been extensive studies on PET presented in the literature due to its potential to meet the global demand for energy.[1-4] In fact, the increase in the global demand for energy along with declining fossil fuel resources and a goal of minimizing the expenses associated with traditional energy conversion methods have prompted substantial governmental, industrial, and academic interest in renewable energy resources such as solar energy.[5] Recently, the conversion of sunlight into energy has been achieved through solar photovoltaic (PV) technologies, which have experienced tremendous growth and become the focus of considerable research interests. PVs based on organic polymer solar cells (PSCs) have emerged as promising low-cost devices that rely on sunlight for electricity generation. Over the past 40 years, organic solar cell (OSC) research has grown and attracted scientific and economic interest by displaying promising properties such as (i) favorable electronic properties and component flexibility; (ii) low production and installation costs, as the active materials are solution processable; and (iii) plausible fabrication of lightweight, large area and flexible devices. [5] Thus, fruitful progress on OSCs will help to utilize solar energy in a sustainable and reasonable way, moving the universal energy portfolio towards viable and low-carbon emission sources. Here, a particular emphasis has been given to realizing and understanding the interfacial photoinduced processes in donor-acceptor systems in PSCs.

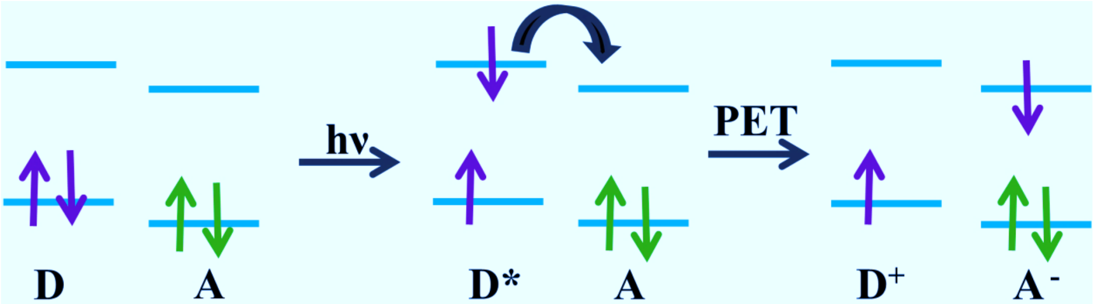

Figure 1.1 Schematic of the photoinduced electron transfer process at a typical donor-acceptor interface.

PET in bimolecular systems involves the absorption of visible (Vis) or ultraviolet (UV) light to initiate electron transfer from a donor (D) molecule to an acceptor (A) molecule, resulting in the formation of radical ions ($A^{-\bullet}$, $D^{+\bullet}$),[6] as shown in Figure 1.1**.** To facilitate electron transfer (ET), the energy level alignment of the highest occupied and lowest unoccupied molecular orbitals (HOMO and LUMO, respectively) of the donor and the acceptor, respectively, is one of the most important factors. Thus, the D-A systems should be selected very carefully to promote the photoinduced electron transfer. A general electronic structure diagram used to describe OPVs is shown in Figure 1.2. From this figure, it is clear that the electron affinity (EA) and the ionization potential energy (IP) of the organic semiconductors under investigation are critically important. The EA shows the ability of a material to act as an electron acceptor and is commonly estimated as the LUMO level relative to the vacuum in an organic material, while the IP of a neutral organic compound is the amount of energy desirable to expel an electron from its HOMO. In a conjugated organic material, the HOMO–LUMO gap describes the minimum energy required to excite an electron from its HOMO to its LUMO. Figure 1.2B displays the typical work functions ϕ_A and ϕ_C for anode and cathode materials in OPVs, respectively, further emphasizing the energetic offsets between the D and A levels, i.e., the HOMO (ΔIP) and LUMO (ΔEA), respectively, which are essential for understanding charge transport mechanisms.[5] To realize a high charge extraction efficiency, the potential barrier at the active layer/electrode interface has to be minimized. Thus, ϕ_A is ideally expected to match the HOMO level of the D, whereas ϕ_C is expected to match the LUMO level of the A.[7]

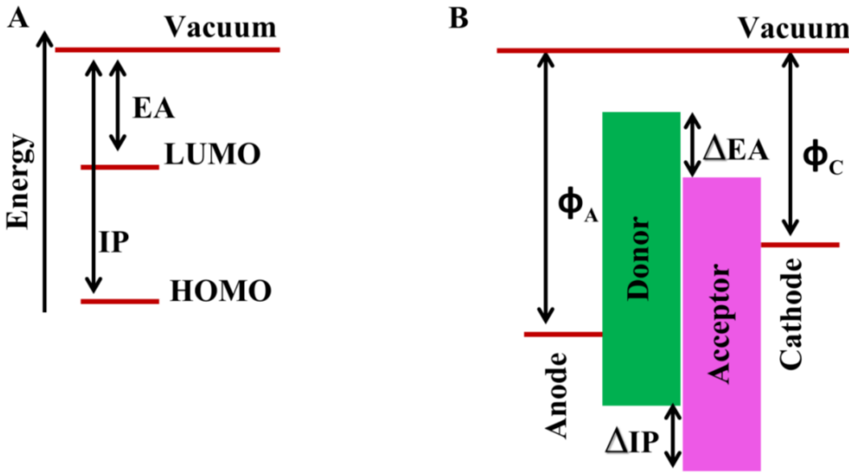

Figure 1.2 Basic energy level diagram schematics of an organic semiconductor (A) and a heterojunction solar cell (B).

1.1.2. Photoconversion Processes of an OPV: Donor-Acceptor System

Understanding and controlling photoconversion processes have long been the subjects of intense research activities. Recently, many studies have been dedicated to the characterization of the mechanisms of long-range charge-transfer processes taking place from π-electron donating groups to electron accepting moieties.[8-9] Figure 1.3 provides a simplified schematic of the photovoltaic procedures in D/A systems, which includes four steps: exciton generation, diffusion, and dissociation, as well as carrier collection.[5, 10] In the first step, an electron can be excited from the donor HOMO to its LUMO upon photoabsorption and form an exciton. A crucial molecular requirement for this step is a high molar absorptivity covering a wide range of the solar spectrum. Once an exciton in the donor material is created, this exciton should then diffuse to a D/A interface (step 2) by means of a chemical potential gradient where the electron can transfer to the acceptor material LUMO level, resulting in the formation of a charge transfer (CT) complex, which will occur favorably when the energy difference between the LUMO levels of the D and A are greater than the exciton binding energy. The CT state can be depicted as having charge carriers that are Coulombically bound through a D/A interface. Thus, the energy of the CT state is highly reliant on the Coulombic attraction forces between of the charge carriers and, thus, on the distance that isolates these species. If the distance between the electron and hole becomes greater than the Coulomb capture radius, the CT state can then be considered a charge separated (CS) state or free charge carriers, as illustrated by step 3 in the photovoltaic process. Importantly, if the exciton is not able to dissociate within its lifetime, the exciton will lose the absorbed energy and decay back to its ground state (GS). Finally, dissociated charges can be transported through p-type or n-type domains to the respective electrodes, as shown in step 4, where they can be used to do work in an external circuit. Thus, charge carrier mobility should be high to facilitate the movement of the charges rapidly from the D-A interface. Additionally, the charge collection at the molecule-electrode interface must occur rapidly (faster than the CR).

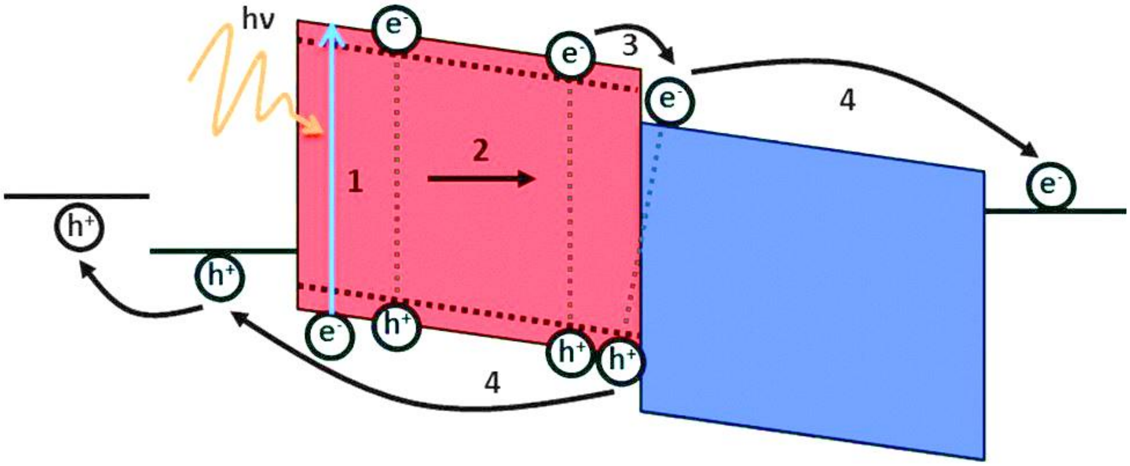

Figure 1.3 Schematic diagram of the operating principles of the planar heterojunction OPV devices, emphasizing the favorable transport of charge pairs through the donor (red) and acceptor (blue) materials.[5]

To enhance the efficiency of devices, a key target in OPVs is to minimize energy and charge loss processes. Though these processes are far more complicated than described, these simplified diagrams are suitable for creating a conceptual understanding of the photoconversion processes in OPV devices.[5, 10]

The work described here is aimed at understanding the charge carrier movement through a system network, which creates a series of transient processes occurring after photoexcitation of the molecules. Thus, it is essential to address the processes involved in the excited state (ES) in order to understand how an electron may absorb and then dispel photon energy of a specific wavelength.

1.2. Excited State Dynamics

The essential electronic transitions involved in the absorption and emission of light by a fluorophore after photoexcitation of the molecule are traditionally displayed by a Jablonski energy diagram (see Figure 1.4).[11]

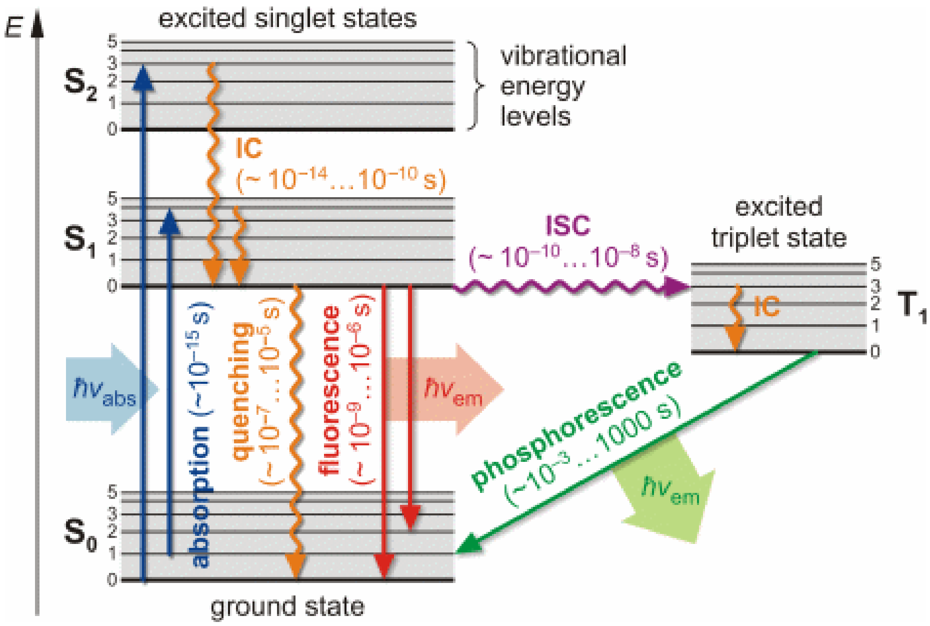

Figure 1.4 Jablonski energy diagram.[12]

In the above figure, the symbols S_0, S_1, S_2, and T_1 indicate the ground electronic state, first excited singlet state, second excited singlet state, and first excited triplet state, respectively. The horizontal lines indicate the vibration levels of every electronic state. Straight arrows represent radiative transitions, and curved arrows represent non-radiative transitions. In the Jablonski diagram, numerous different pathways display how an electron may absorb and then dissipate photon energy of a certain wavelength, which are as follows.[11, 13]

A. Absorbance

The first transition is photon absorption by the photoactive material. The photon energy is transferred to a certain electron, which then triggers a different energy state according to the amount of energy transferred. Importantly, only particular wavelengths of light can potentially be absorbed, i.e., the wavelengths that have energies that match the difference between two energy states of the particular molecule. Absorbance is a very fast transition on the order of 10^{-15} s.[11]

B. Vibrational Relaxation and Internal Conversion

Once an electron is excited, energy can be dissipated in various ways. The first is through a non-radiative process called vibrational relaxation. This process is shown in the Jablonski diagram as a curved arrow between vibrational levels. Vibrational relaxation occurs when the energy deposited by the photon into the electron is given away to other vibrational modes as kinetic energy. This process is very fast, taking place between 10^{-14} and 10^{-11} s. Thus, it is extremely likely to occur immediately following absorbance. However, if vibrational energy levels strongly overlap electronic energy levels, a probability exists that the excited electron can move from a vibration level in one electronic state to another vibration level in a lower electronic state (for example, from S_2 to S_1); this phenomenon is known as internal conversion (IC). As energies increase, the IC occurs in the same time frame as vibrational relaxation; therefore, it is a very likely way for molecules to dissipate energy from light perturbation.[13]

C. Fluorescence

An excited molecule exists in the lowest S_1 for periods on the nanosecond (ns) time scale. After this time period, typically known as the excited state lifetime, final relaxation to the ground state is accompanied by the emission of a photon, which is known as fluorescence. It is outlined on a Jablonski diagram as a straight line moving down between electronic states on the energy axis. It is a slow process with a time scale on the order of 10^{-9} to 10^{-7} s. While this transition is slow, it is a spin-allowed process that obeys the selection rule $\Delta S = 0$, in contrast to phosphorescence, where a forbidden transition occurs between the first excited triplet state T_1 to the ground state S_0 after a non-radiative transition from S_1 to an isoenergetic vibrational level of a triplet state T_1 with a change in spin multiplicity. Fluorescence is most commonly observed between (S_1) and (GS) because at higher energies, it is expected that the energy will disappear through internal conversion (IC) and vibrational relaxation. Hence, the energy of fluorescent photons is always less than that of the exciting photons. This difference is due to energy loss via internal conversion and vibrational relaxation.[13]

D. Intersystem Crossing

Intersystem crossing (ISC) occurs when the electron changes its spin multiplicity and is transferred from an S_n to a T_n. It is shown by a horizontal, curved arrow from one column to another in a Jablonski diagram, and it is the slowest process at several orders of magnitude slower than fluorescence. This slow transition is a forbidden transition, that is, a transition that should not happen based only on selection rules. Similar to the singlet state, the populated triplet states will undergo relaxation via a radiative transition process called phosphorescence, where a radiative transition from T_1 to S_0 occurs after the non-radiative process called IC, where the transition from a higher vibration level to the lowest vibration level in the triplet state occurs.

E. Time Scale

Understanding the time scales of each of these possible transitions is essential to understanding the feasibility of these processes. Table 1.1 summarizes the time scales for basic radiative and non-radiative processes.

Table 1-1 The approximate timescales for basic radiative and non-radiative transitions processes.[13-14]

Process	**Transition**	**Time Scale**	**Radiative Process**
Absorption	$S_0 \rightarrow S_n$	10^{-15} s	No
Internal Conversion	$S_n \rightarrow S_1$	10^{-14} - 10^{-11} s	No
Vibrational Relaxation	$S_n^* \rightarrow S_n$	10^{-14} - 10^{-11} s	No
Fluorescence	$S_1 \rightarrow S_0$	10^{-9} - 10^{-6} s	Yes
Intersystem Crossing	$S_1 \rightarrow T_1$	10^{-11} - 10^{-6} s	No
Phosphorescence	$T_1 \rightarrow S_0$	10^{-3} - 100 s	Yes

where $Sn^* \rightarrow S_n$ indicates that relaxation occurs between vibrational levels, so generally, electrons will not move from one electronic level to another through this process.

In OPV devices, the forward CT and competing paths, such as charge recombination, occur at time scales on the order of femto- to milliseconds.[15] To follow these transient processes in real time, ultrafast spectroscopic measurement methods are needed to provide information about the charge migration via the materials. Hence, time-resolved spectroscopy (TRS) can be a useful way to monitor these transient species.

1.3. Time-Resolved Spectroscopy

Time-resolved spectroscopy (TRS) offers a broad range of applications in various areas of research including chemistry, physics, materials science and nanotechnology. TRS allows us to probe in real time the very early dynamical events (such as excitons and charge carriers generated by photoexcitation) occurring on the femtosecond (one femtosecond = 10^{-15} s) and picosecond (1 picosecond = 10^{-12} s) time scales. The current TRS techniques have been advanced dramatically by the development of modern spectroscopic appliances. For example, the application of time-resolved optical spectroscopy has developed from a modest beginning with the (flash) photolysis technique, which has millisecond resolution; this technique was designed by Norrish and Porter,[16-17] who in 1967 were awarded the Nobel Prize in Chemistry for their finding.[18] Their study opened a new world of research in the microsecond time domain, allowing the direct detection of short-lived transient species. Subsequently, this technique has been further improved with the emergence of short-pulsed lasers with a resolution of femtoseconds. In 1999, Zewail was awarded the Nobel Prize in Chemistry for his studies on the transition states of chemical reactions using femtosecond spectroscopy.[19]

1.3.1. Time-Resolved Fluorescence Spectroscopy

Another way for a molecule to lose its excited state energy is fluorescence (emission of a photon). In time-resolved fluorescence spectroscopy, the molecules are usually excited using a laser pulse, and their fluorescence spectrum is recorded as a function of time by using, for example, time-correlated single photon counting (TCSPC).

TCSPC is the most sensitive electronic method to measure the luminescence lifetime. It has a limited time resolution of at best a few picoseconds (ps), which is usually determined by measuring the duration of the light pulse that is elastically scattered by the sample. Furthermore, TCSPC is a single-wavelength method. At each given time, the fluorescence kinetics are only registered at one detection wavelength. TCSPC has significant advantages, such as not requiring intense excitation light. The fundamental assumption of this technique is that each excitation pulse causes only one fluorescence photon to be detected. TCSPC is also completely insensitive to the stability of the laser pulse energy (even if these energies fluctuate by a factor of two, the method still works).[20]

1.3.2. Pump-Probe Spectroscopy: Transient Absorption Measurements

Pump–probe experiments, such as the ones described and broadly used within this dissertation, are some of the most powerful techniques for detecting transient species and providing direct measurements of the charge carrier dynamics by monitoring the evolution of charge-separated states in donor-acceptor systems.[21] Understanding the photophysical and photochemical processes in donor-acceptor systems, such as CT, CS and CR processes, can clearly support the improvement of solar device performance by providing fundamental information required for device optimization and fabrication.[22] The idea behind transient absorption (TA) measurements is simple. It is based upon two ultra-short laser pulses. One serves as a pump light used to excite a system into an excited state (from S_0 to S_n), and subsequently, the second pulse works as a probe light. The basic design of all pump-probe experiments follows the schematic shown in Figure 1.5 to monitor CT, CS, and recombination dynamics in real time, providing essential information about the mechanistic and kinetic details of the major events that occur on very short time scales. The time resolution of the ultrafast pump-probe experiments depends on both the durations of the ultrafast pump and probe pulses and the resolution of the time delay generated between them.[23]

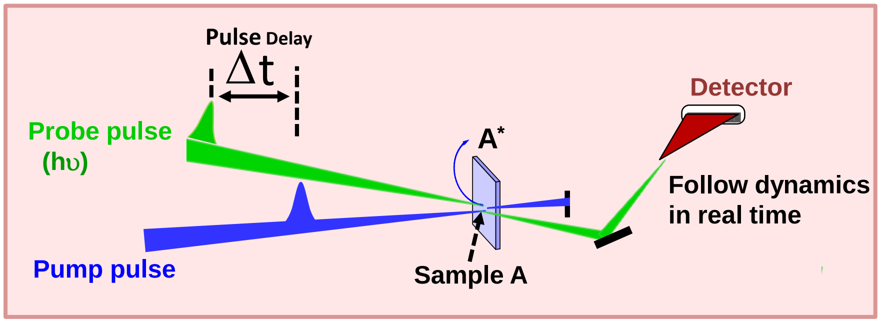

Figure 1.5 Schematic depiction of the basic pump-probe experimental arrangement: pump pulse excites the sample, and the probe is used to measure the transmittance. The variable delay between the pump and probe pulses provides the time dependence of the difference absorption signal.

Obviously, the pump pulse should be more intense than the probe pulse because it produces the changes in the molecules, whereas the probe only interrogates them, and for ideal measurements, the probe should not have any influence on the sample under investigation.

1.3.3. Femtosecond and Nanosecond Transient Absorption Spectroscopy

fs and ns TA spectroscopies are unique broadband pump-probe TA techniques designed to work with highly amplified laser resolutions. fs-TA and ns-TA measurements are performed using the HELIOS and EOS setups (Ultrafast Systems), respectively. For the fs-TA experiments, the HELIOS system will produce outstanding spectral and kinetic data that are desirable for investigations of photoexcitation events with ultrafast time resolutions throughout its broad spectral coverage and long-time window. For the ns-TA measurements, the EOS system is designed to work with almost any ~1 kHz repetition rate laser to allow the collection of broadband TA spectra over a greatly extended time regime ranging from several ns to hundreds of ms after the photoexcitation. The instrumental setup of the ultrafast systems (HELIOS and EOS) will be discussed later in appendix A, section A3(II). In this technique, the pump and probe beams are adjusted to overlap spatially and temporally on the sample. The chosen spectrometer collects the probe beam after passing through filters that reduce the white light around the Spitfire fundamental at 800 nm. The TA spectra are usually averaged until the desired signal-to-noise ratio is achieved. For both the fs- and ns-TA, only the total absorption signals obtained are recorded. Finally, global analysis fitting procedures are applied to extract the kinetics of dynamical processes from the TA spectra.

1.4. Transient Absorption Spectrum

TA spectroscopic signature signals reveal invaluable information about several dynamical processes upon the occupation of the excited state (*e.g.,* charge separation, trapping, radiative recombination, Auger recombination). From positive and/or negative signal contributions within the absorbance change (ΔA) spectra as illustrated in Figure 1.6, we can extract useful information about different processes as follows.[24]

Ground State Bleach (GSB): corresponds to the depletion of the ground state (GS) population upon interaction with a pump pulse. Consequently, a negative signal is observed in the wavelength region of the GS absorption due to the reduction in the concentration (c) of the chromophore in its GS. Accordingly, the repopulation of the GS can be detected as the recovery of the negative GSB signal.

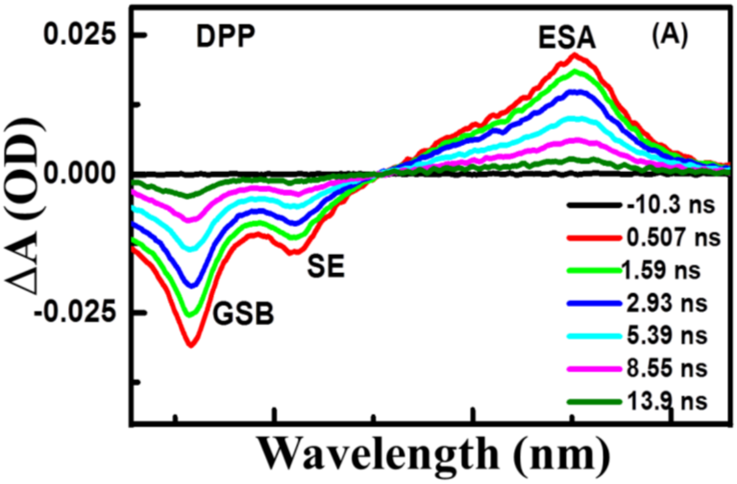

Figure 1.6 TA spectrum illustration; a ΔA: ground-state bleach (GSB), stimulated emission (SE), and excited-state absorption (ESA).[25]

Excited State Absorption (ESA): represents the promotion of charge carriers that were previously excited by a pump pulse to an energetically higher excited state upon interaction with the probe pulse. Accordingly, a positive signal is obtained in the wavelength region of the excited state absorption with a decrease in the intensity of the detected light (i.e*.,* photons are absorbed by the sample in a spectral region where they were previously transmitted). The positive signal due to ESA decays with the lifetime of the excited state (ES).

Photoproduct Absorption: results from the interaction of newly formed chemical species or long lived ES (*e.g.,* charge-separated states, triplet states) with the probe pulse, which promotes them to the ES. Since photons are absorbed by the sample in a spectral region where they were previously transmitted, the absorption of such a (transient) product will appear as a positive signal in the ΔA spectrum. The kinetics of the signal can show rise and decay characteristics of this product.

Stimulated Emission (SE): If the energy of the subsequent probe pulse matches the $S_1 \rightarrow S_0$ transition energy of a chromophore in its ES, it can force the excited chromophore back to its GS, and a second photon with the same energy and in phase with the first (probe) photon is emitted ("stimulated emission").

In the TA measurement, the intensity of the probe light transmitted through a sample is detected before (I_0) and after (I) the photoexcitation. From the intensity ratio, the absorbance change is given by the following equation:

$$\Delta OD = \log\left(\frac{I_0}{I}\right) \tag{1}$$

From this relation, photoproducts provide positive signals in the ΔOD while photobleaching results in negative signals in the ΔOD due to the decrease in the ground state as schematically indicated in Figure 1.6. Using TRS techniques, it is possible to detect absorbance changes on the order of as small as 10^{-5} to 10^{-6} depending on the measuring time domain after appropriate accumulation. However, according to Lambert–Beer's law, the absorbance change is given by the following equation:

$$\Delta OD = \varepsilon \mathrm{cl} \tag{2}$$

where (ε) is the molar absorption coefficient ($\mathrm{mol^{-1}\ dm^{3}\ cm^{-1}}$), (c) is the molar concentration ($\mathrm{mol\ dm^{-3}}$), and (l) is the optical path length (cm). Based on this law, it is therefore technically difficult to detect a small absorbance change of 10^{-5}, in which the photoactive layer is typically as thin as 100 nm.[26]

1.5. Objective and Outline of the Thesis

1.5.1. Objective

Since an efficient PV device requires fast CT and a long-lived CS state, understanding the CT dynamics at D-A interfaces is essential to improving PV performance. Herein, we employ ultrafast broadband time-resolved spectroscopy, which is a useful technique that provides direct information on the fundamental photovoltaic processes (charge carrier dynamics) at D-A interfaces, allowing monitoring of the evolution of charge-separated states in D-A systems. This work is aimed at investigating the effects of the incorporation of heavy metals into π-conjugated chromophores for the exploration of triplet states and their impacts on solar cells using a combination of steady-state measurements and femtosecond (fs) broadband transient absorption spectroscopy. In addition, this work explores the significant impact of ultrafast CS and CR at D/A interfaces on the device performance of conjugated polymers.

1.5.2. Outline

First, a detailed introduction will be given at the beginning of each chapter to understand the background, perspective and aim of the work reported, which is a comprehensive study of photoinduced CT in D-A systems using fs broadband TA spectroscopy as a superior technique to investigate the ES charge carrier dynamics.

In chapter 2, we study the ultrafast interfacial CT between PTB7-Th and three FAs, $PC_{71}BM$, $PCB_{61}BM$ and $IC_{60}BA$. Time-resolved TA experiments exhibit a long-lived CS state between PTB7-Th and $PC_{71}BM$ and $PC_{61}BM$, while that between PTB7-Th and $IC_{60}BA$ produces short-lived charges at the D/A interface. Interestingly, a good correlation between steady-state and time-resolved results and device performance is presented. We report high power conversion efficiencies (PCEs) of 9.22% and 8.66% in the presence of $PC_{71}BM$ and $PC_{61}BM$, respectively, while we measure a low performance value of 2.16% for $IC_{60}BA$.

In chapter 3, we investigate the bimolecular PET from DPP-Pt(II)(acac) to tetracyanoethylene (TCNE) as an electron acceptor. We predict that the DPP-

Pt(II)(acac)/TCNE system can form CT complexes, thereby displaying interesting photophysical properties including ultrafast PET, rapid CS, and slow CR. We show how the incorporation of Pt(II) can control ISC and PET dynamics from the oligomer to TCNE. The influence of Pt(II) unit incorporation has been evaluated by comparing and analyzing the photoexcited dynamics of DPP-Pt(II)(acac)/TCNE and DPP/TCNE systems.

In chapter 4, we monitor the interactions between (TMPyP) and (TPyP) with DPP-Pt(acac) in dichloromethane (DCM):dimethylformamide (DMF) mixtures. We report for the first time the ultrafast on/off charge transfer between a new platinum-containing oligomer as an electron donor and different porphyrin structures as an electron acceptor. We found that both the metallic center in the DPP-Pt(acac) oligomer and the positive charge on the porphyrin are required to switch on the reaction.

Chapter 5 provides a summary and outlook of this work.

CHAPTER 2

REMARKABLY HIGH CONVERSION EFFICIENCY OF INVERTED BULK HETEROJUNCTION SOLAR CELLS: FROM ULTRAFAST LASER SPECTROSCOPY AND ELECTRON MICROSCOPY TO DEVICE FABRICATION AND OPTIMIZATION

2.1. Introduction

2.1.1. Polymer Solar Cell Background

At the beginning of the 20th century, photoconductivity was first observed in the organic moiety anthracene, which was intensively studied.[27] One of the most studied photoconductive polymers is poly(vinyl carbazole) (PVK), and the first report came in 1958 by Hoegel et al.[28] Among the dye molecules, the first real PV examinations were done on porphyrins and in polymer solar cell (PSC), and this class of compounds has remained among the most studied dyes. They have highly attractive features. For example, they are easy to prepare, highly colored, and form crystalline films with high semiconducting properties by vacuum sublimation.[29] While PSC research has grown over the past 40 years, it has attracted significant attention from both academic and industrial communities, especially in the last decade, with a rapid increase in power conversion efficiency. This accomplishment was achieved by the introduction of new

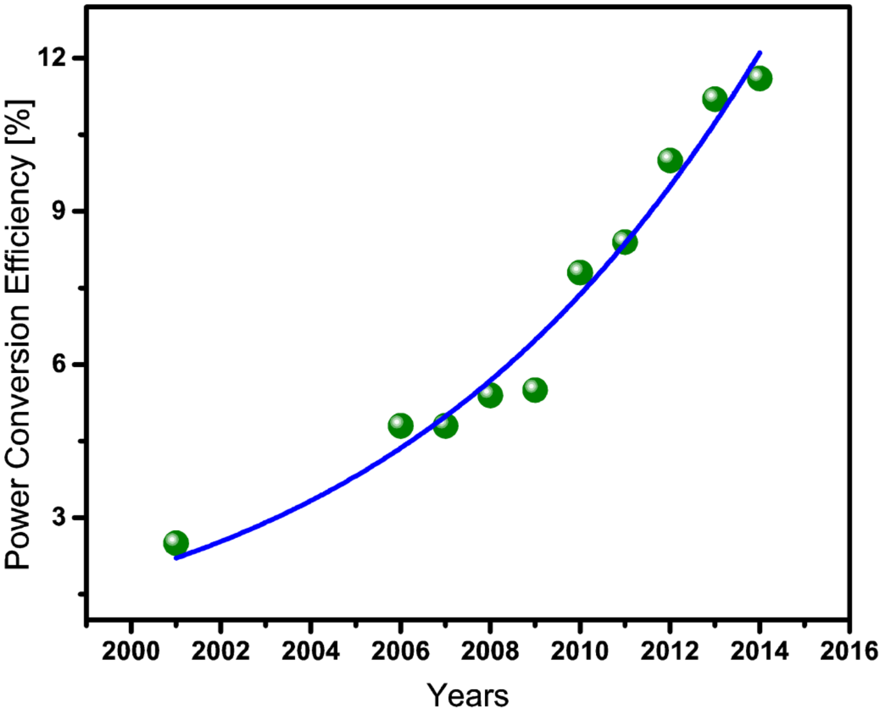

Figure 2.1 Trend of the change of power conversion efficiency (PCE) of PSCs from 2001 to 2014.

materials, improved materials engineering, and more sophisticated device structures. In addition, PSCs offer a suite of promising properties, such as tunable molecular energy levels and large-scale, low-cost production[30-32] via solution processing methods that are appropriate for flexible devices and large areas.[5] In the last few years, the solar power conversion efficiencies (PCE) of PSCs have progressively increased from ca. 1% in 1995 to ~9% recently for single junction devices and ~11% for tandem devices with good stability[33-36] fabricated with several device concepts with low bandgap semiconducting polymers.[37-41] Figure 2.1 summarizes the growing trend of the PCEs of PSCs from 2001 to 2014.[42] A significant portion of these high-performance semiconducting polymers have D−A structures, and their optical bandgaps are controlled successfully by an appropriate blend of D and A units. The absorption bandwidth, charge carrier mobility, and morphology of the active layer are the other factors that control the photocurrents of PSCs.[43] In addition, molecular engineering of conjugated polymers has become one of the main driving forces to promote PSC development. A high-performance conjugated polymer as a donor material in the PSCs should have at least the following three essential features: (a) a broad and strong absorption band to ensure the efficient harvest of solar light, (ii) appropriate highest occupied molecular orbital (HOMO) level and lowest unoccupied molecular orbital (LUMO) level to realize efficient charge separation with low energy loss, and (iii) high hole mobility for facilitating charge transport.[10] In addition to these features, they should have good solubility in organic solvents. Up to now, most of the D units in semiconducting polymers representing the high PCEs are thiophene derivatives, which exhibit strong electron-donating characteristics along with effective π−π stacking and high hole mobility.[44-45] In contrast to the D units, a wider variety of A units have been created owing to the fact that the electron insufficient nature of A units can be tuned adequately via the substitution of electron withdrawing or electron releasing groups on the A unit.

2.1.2. Motivation

PSCs involving conjugated polymer donor and fullerene derivative acceptor materials are a promising alternative for producing clean and renewable energy.[46] Numerous significant milestones in PSC studies have been established on the way to the realization of practical applications. However, their relative power conversion efficiencies (PCEs) are limited by the non-ideal selectivity of the donor/acceptor (D/A) components and reduced ordering of polymer chains in the blend, which hinders transport in the electron transport layer (ETL). Although significant efforts have been made towards interface engineering and morphology control, devices continue to undergo carrier trapping at their interface and, more importantly, a low open-circuit voltage due to the thermalization of charge carriers, causing poor efficiency. To improve the PCEs of devices, we need a fundamental understanding of the CT processes at D/A interfaces in the photoactive layer, the morphological tunability, and the grain alignment of the ETL and the hole transport layer (HTL).[47-48] In other words, the performances of PSC devices are determined by a series of fundamental photophysical processes occurring at the interface before carrier collection. As stated above, the PCEs of devices are determined by the photoinduced CS that follows the interfacial CT and the subsequent CR.[49-51] Thus, controlling the transfer of electrons from the (HOMO) level located in the donor to the (LUMO)level situated in the acceptor and the CS that leads to radical ions ($D^{+\bullet}$ and $A^{-\bullet}$) are central to optimizing the PCEs of solar cell devices.[52] In high-performance PSCs, the molecular acceptors and the morphology and grain alignment of the ETL are as important as the electron donors; however, fewer characterizations have been made for the impact of electron acceptors and ETLs on device operation. Because of their high electron mobilities and large electron affinities, the majority of the molecular acceptors used in PSCs continue to be the fullerene derivatives $PC_{60}BM$ and $PC_{71}BM$, although some n-type conjugated polymers with stronger visible absorption have also been applied.[53-57] More specifically, the degree of CS is correlated with the mobility and molecular structure of fullerene derivatives.[58] In fullerene-based devices, the carrier concentration in the fullerene layer can be increased by transfer of electrons from the donor. This, consequently, leads to minor hysteresis and high performance of the device via effective reduction of the interfacial energy barrier for charge extraction at the donor-fullerene interface.[58-60]

2.1.3. PSCs Based on BDT Units

Among various types of electron donor conjugated polymers, polymers based on benzo[1,2-*b*:4,5-*b*′]dithiophene (BDT) units reveal promising photovoltaic properties and have shown excellent device performance.[61-63] More excitingly, many recent advancements in PCEs have been linked to BDT-based polymers, and polymers based on BDT have become one of the main families of OPV materials.[64-66] Recently, a new polymer, poly[4,8-bis(5-(2-ethylhexyl)thiophen-2-yl)benzo[1,2-*b*;4,5-*b*′]dithiophene-2,6-diyl-alt-(4-(2-ethylhexyl)-3-fluorothieno[3,4-*b*]thiophene-)-2-carboxylate-2-6-diyl)], which is commonly known as PTB7-Th/PCE10/PBDTTT-EFT, has been developed, and its structure is shown in Figure 2.2. Indeed, an efficiency greater than 9 has been reported for solar cells based on this polymer as illustrated in Figure 2.3. [67-68]

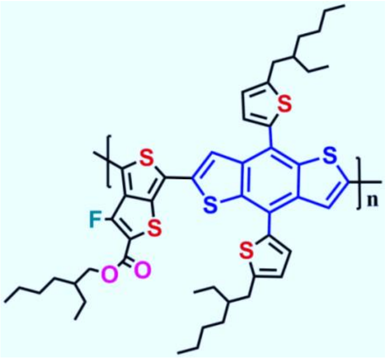

Figure 2.2 Molecular structure of the PTB7-Th polymer based on the BDT unit (blue structure).

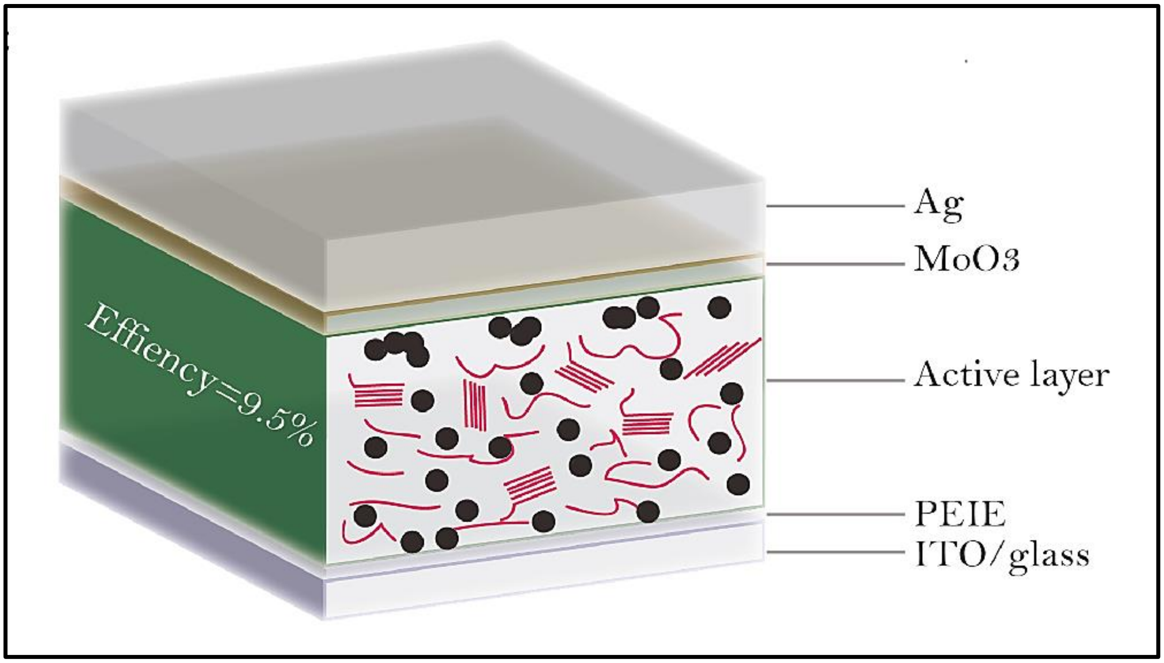

Figure 2.3 Schematic of the inverted PTB7-Th/PCBM device showing a high efficiency.[68]

In this work, the photoinduced charge transfer and the bulk heterojunction (BHJ) solar cell performances with PTB7-Th as the electron donor were investigated using a series of fullerene acceptors (FAs): [6,6]-phenyl-C71-butyric acid methyl ester ($PC_{71}BM$); [6,6]-phenyl-C61-butyric acid methyl ester ($PC_{61}BM$); and indene-C60 bis-adduct ($IC_{60}BA$). The molecular structures of these materials are shown in Figure 2.4.

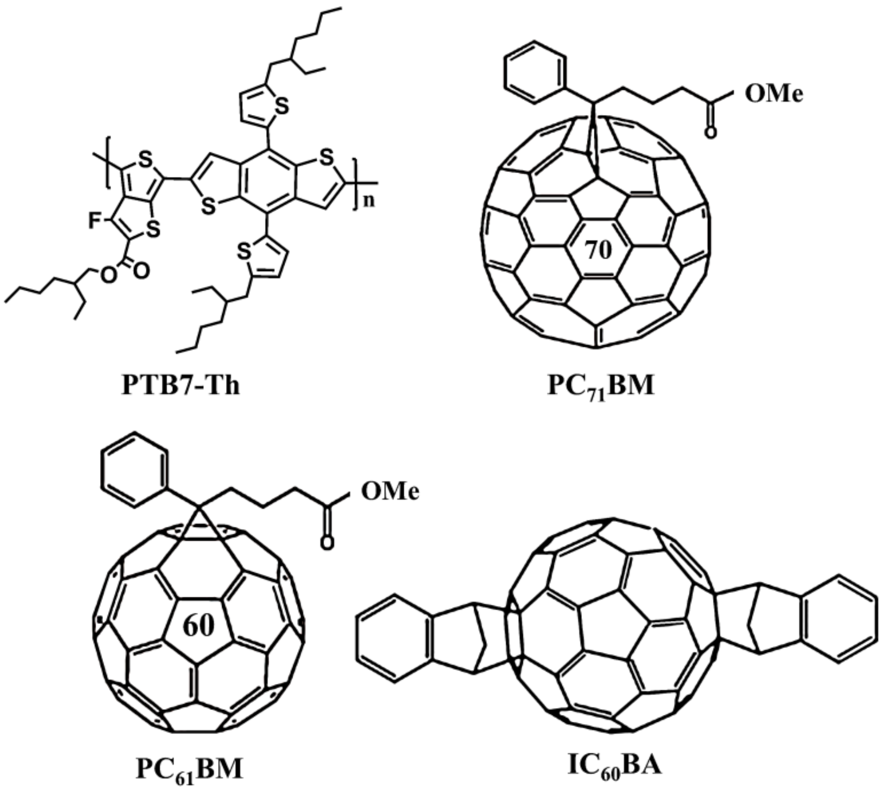

Figure 2.4 Molecular structures of the PTB7-Th donor polymer and the three FAs ($PC_{71}BM$, $PC_{61}BM$, and $IC_{60}BM$) used in this study.

Although PTB7-Th is a striking absorber layer for application in organic photovoltaics due to its π-electron rich units, thermal stability, and low HOMO-LUMO levels with an optical band gap of 1.58 eV,[69] no progress has been made in the study of the ultrafast photophysical processes at PTB7-Th/FA interfaces. In this work, steady-state photoluminescence (PL) experiments reveal efficient quenching of PTB7-Th fluorescence upon addition of the FAs $PC_{71}BM$, $PC_{61}BM$, and $IC_{60}BA$, clearly indicating an excited-state interaction between PTB7-Th and the electron acceptors. An estimated 97% quenching of PTB7-Th was accomplished upon addition of ~2.6 mM $PC_{71}BM$, while 91 and 81%

quenching were realized upon addition of ~5 mM $PC_{61}BM$ and $IC_{60}BA$, respectively. Time-resolved TA experiments exhibit long-lived charge-separated states, as indicated by the slower ground-state bleach (GSB) recovery of PTB7-Th/$PC_{71}BM$ and PTB7-Th/$PC_{61}BM$ compared to free PTB7-Th. In sharp contrast, the GSB recovery of PTB7-Th/$IC_{60}BA$ is much faster compared to that of free PTB7-Th, indicating an insufficient driving force for photoinduced electron transfer and CS.[70] Moreover, a good correlation between steady-state and time-resolved results and device performance is presented. High PCE performance values of 9.22% and 8.66% are realized in the presence of $PC_{71}BM$ and $PC_{61}BM$, respectively, and a low-performance value of 2.16% is measured for $IC_{60}BA$. Finally, grain alignment and morphological control of the ZnO ETL as indicated from high-resolution electron microscopy experiments are prepared via a simple, scalable method and optimized to improve solar PCEs.

2.2. Results and Discussions

2.2.1. Steady State Measurements

In the absence of FAs, the absorption spectrum of PTB7-Th exhibits two peaks centered at 638 nm and 703 nm, as shown in Figure 2.5. The steady-state absorption and photoluminescence spectra of PTB7-Th are shown with successive additions of $PC_{71}BM$, $PC_{61}BM$ and $IC_{60}BA$ in Figure 2.6 (A-C). The experimental apparatus and details of the conditions are provided in appendix A, section A3(I). Increasing the amount of added FA causes the absorption to increase in the region below 685 nm due to the absorption of the FAs in this spectral region. Photoexcitation of PTB7-Th at 680 nm yields a fluorescence spectrum in the visible and near-infrared (NIR) spectral region between 680-850 nm, with a maximum peak at 753 nm. From the photoluminescence spectra of PTB7-Th, it is apparent that the polymer emission is strongly quenched by approximately 97%, 91% and 81% upon addition of 2.61 mM $PC_{71}BM$, 5 mM $PC_{61}BM$ and 5 mM $IC_{60}BA$, respectively. This result provides clear experimental evidence of photoinduced electron transfer from the polymer donor to the FAs. Note that energy transfer can be overruled due to the lack of spectral overlap between the absorption of the FAs and the emission of the PTB7-Th polymer (see Figure SB.1 in appendix B). Additionally, based on the extinction coefficients of this polymer (ε on the order of 10^5-10^6 $M^{-1}cm^{-1}$), which is a few orders of magnitude higher than those fullerenes, the inner filter effect on fluorescence quenching can be ignored. The highest quenching efficiency achieved by $PC_{71}BM$ indicates the effectiveness of the excited-state interaction between PTB7-Th and $PC_{71}BM$.

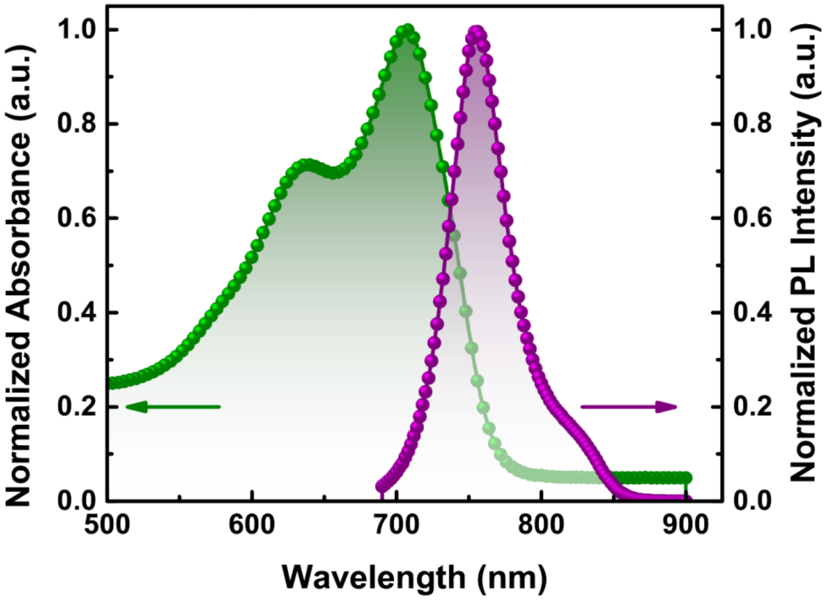

Figure 2.5 Normalized absorbance and photoluminescence spectra of the PTB7-Th polymer.

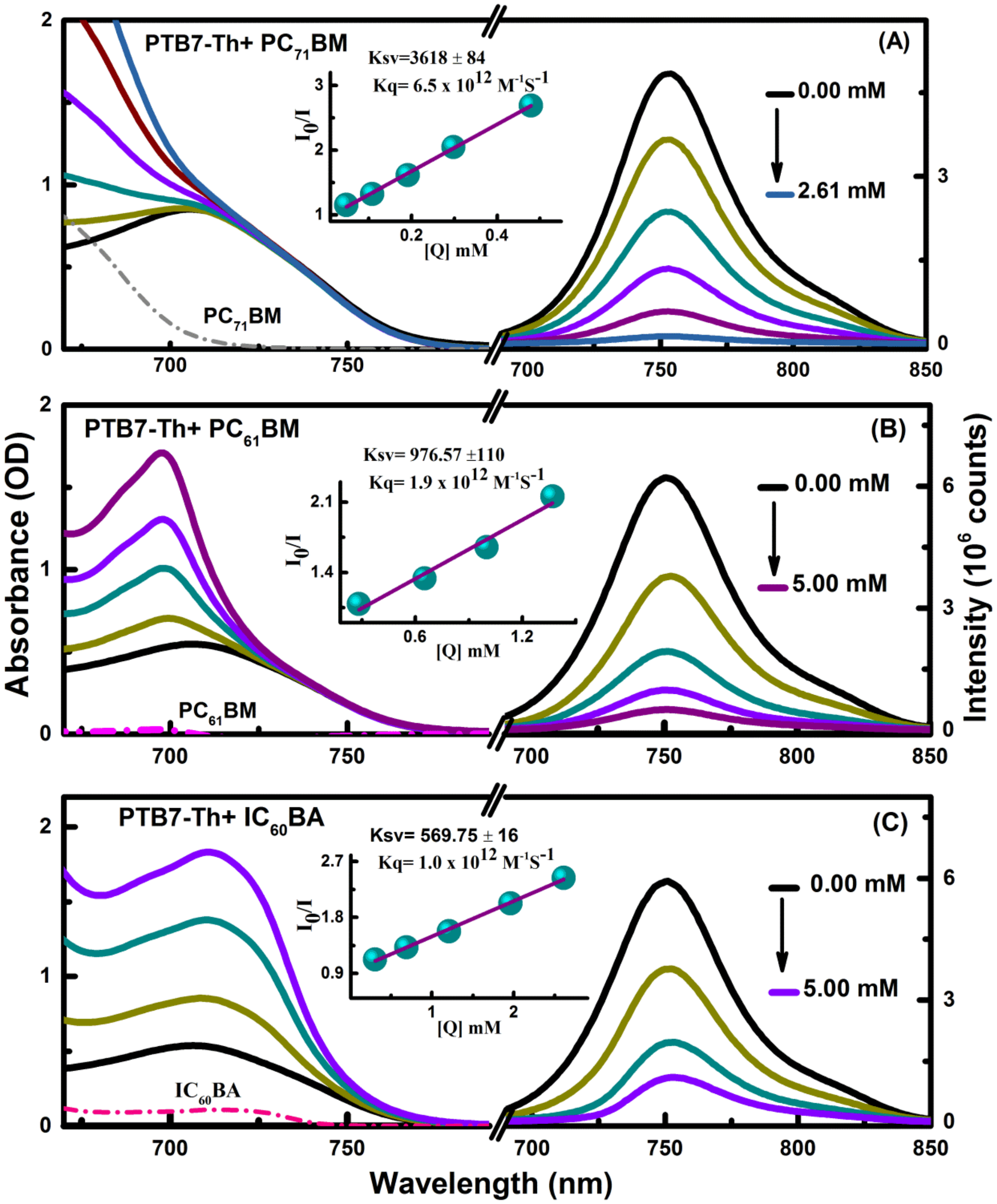

Figure 2.6 Steady-state absorption (left) and emission (right) after excitation at 680 nm of the donor polymer/FA systems. (A) PTB7-Th with different concentrations of PC$_{71}$BM, (B) PTB7-Th with various concentrations of PC$_{61}$BM and (C) PTB7-Th in various concentrations of IC$_{60}$BA. Insets represent the respective Stern-Volmer plots.

Stern-Volmer Method

The most common method to study PET reactions is through fluorescence quenching.[71] Studies of the quenching process and mechanism for a donor/acceptor system leads to the estimation of the quenching rate constant (kq) through the Stern–Volmer method.[72] Consequently, one can obtain a total rate constant for the PET process. Utilizing this method, individuals have investigated the bimolecular PET reaction in neat solvent (intrinsic donor) media to find a detailed mechanistic and dynamical understanding, where the ET rate is faster than solvation and diffusion.[73-76] Thus, the occurrence of electron transfer should diminish both the fluorescence quantum yield and lifetime. There are, however, other mechanisms that can contribute to fluorescence quenching, such as energy transfer, hydrogen bonding and the external heavy atom effect. To establish the cause of fluorescence quenching, careful examination of the experimental conditions and chosen variations are required. From the absorption and emission characteristics, it can be determined whether energy transfer is possible. The presence of hydrogen bonds can likewise be a channel for a non-radiative deactivation path. The heavy atom effect is produced by enhanced spin-orbit coupling, which is more efficient in heavier atoms. The rate of intersystem crossing is enhanced by this mechanism, and thus, the lifetime of the excited singlet state is reduced.

In this present contribution, in order to explore the nature of the kinetics of photoinduced electron transfer we constructed a Stern-Volmer plot using the following equation:

$$I_0/I = 1 + K_{SV}[Q] \tag{3}$$

where (I_0) and (I) are the fluorescence intensity of PTB7-Th in the absence and presence of quenchers, respectively, and K_{SV} is the Stern-Volmer quenching constant. [77] The insets in Figure 2.6(A-C) illustrate the Stern-Volmer plots, quenching constants and bimolecular quenching rate constant (K_q) of all three quenchers. The quenching rates are estimated to be 6.5×10^{12} $M^{-1}S^{-1}$, 1.9×10^{12} $M^{-1}S^{-1}$ and 1×10^{12} $M^{-1}S^{-1}$ for $PC_{71}BM$, $PC_{61}BM$ and $IC_{60}BA$, respectively. In chlorobenzene (CB), the quenching rate constant for the diffusion-controlled limit is 8.77×10^{9} $M^{-1}S^{-1}$, indicating that the quenching of PTB7-Th is expected to be static in nature, a result that is conclusively supported by our fs-TA experiments, as will be discussed in a later section.

2.2.2. Time-Resolved Spectroscopy

To gain further insight into the excited-state dynamics,[25, 78-81] we conducted fs time-resolved TA spectroscopy with broadband capabilities for PTB7-Th with and without the three FAs in CB as the solvent. The details of the TA experimental apparatus and conditions are reported in appendix A, section A3(II). Figure 2.7 shows the TA spectra of PTB7-Th in the absence and presence of 3 mM FAs ($PC_{71}BM$, $PC_{61}BM$ or $IC_{60}BA$). The spectra were measured following a 760-nm laser pulse excitation to excite PTB7-Th selectively. Figure 2.7A shows a clear optical excitation of the polymer immediately resulting in ground-state bleach (GSB) at 638 and 738 nm, corresponding to ground-state absorption. Time-resolved TA experiments show 77% recovery of GSB for free PTB7-Th over ~2 ns. Although the changes in the GSB recovery were not significant in the presence of FA (see Figure 2.7 b-d), some slight differences in behavior were noted. When either $PC_{71}BM$ or $PC_{61}BM$ are added, the GSB recovery proceeds more slowly than that of free PTB7-Th, while in the presence of $IC_{60}BA$, the recovery proceeds more quickly. After a few nanoseconds, $PC_{71}BM$ and $PC_{61}BM$ have the lowest percentage of GSB recovery (70% and 75%, respectively), while adding $IC_{60}BA$ results in the greatest percentage of GSB recovery (82%) (within two ns). The observed changes in the percentage recovery rates of GSB verify that successful photoinduced CT, CS and CR strongly depend on the mobility and the molecular structure of the fullerene derivatives. The efficient charge dissociation observed for the $PC_{71}BM$-based device compared to that of $PC_{61}BM$- or $IC_{60}BA$-based devices is fully supported by the relatively higher electron mobility of $PC_{71}BM$, in line with the established correlation between carrier mobility and CS.[58] Thus, a slower and less complete GSB recovery by $PC_{71}BM$ and $PC_{61}BM$ indicated a longer-lived CS. Meanwhile, the faster GSB in the presence of $IC_{60}BA$ suggests faster CR and short-lived CS; the kinetic profile (Figure 2.8) also confirms this finding, as we will discuss in the following section.

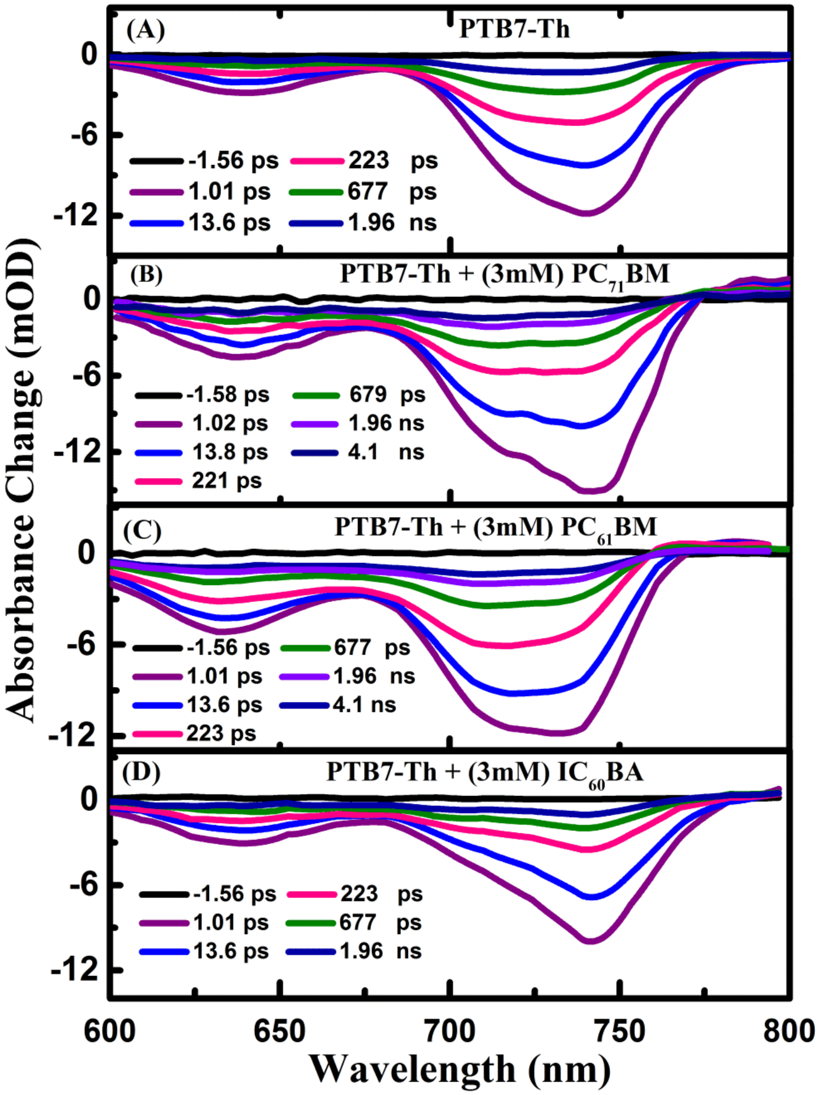

Figure 2.7 TA spectra of the PTB7-Th solution in the (A) absence and (B, C and D) presence of 3 mM FAs pumped at 760 nm. Delay times are as indicated in the Figures.

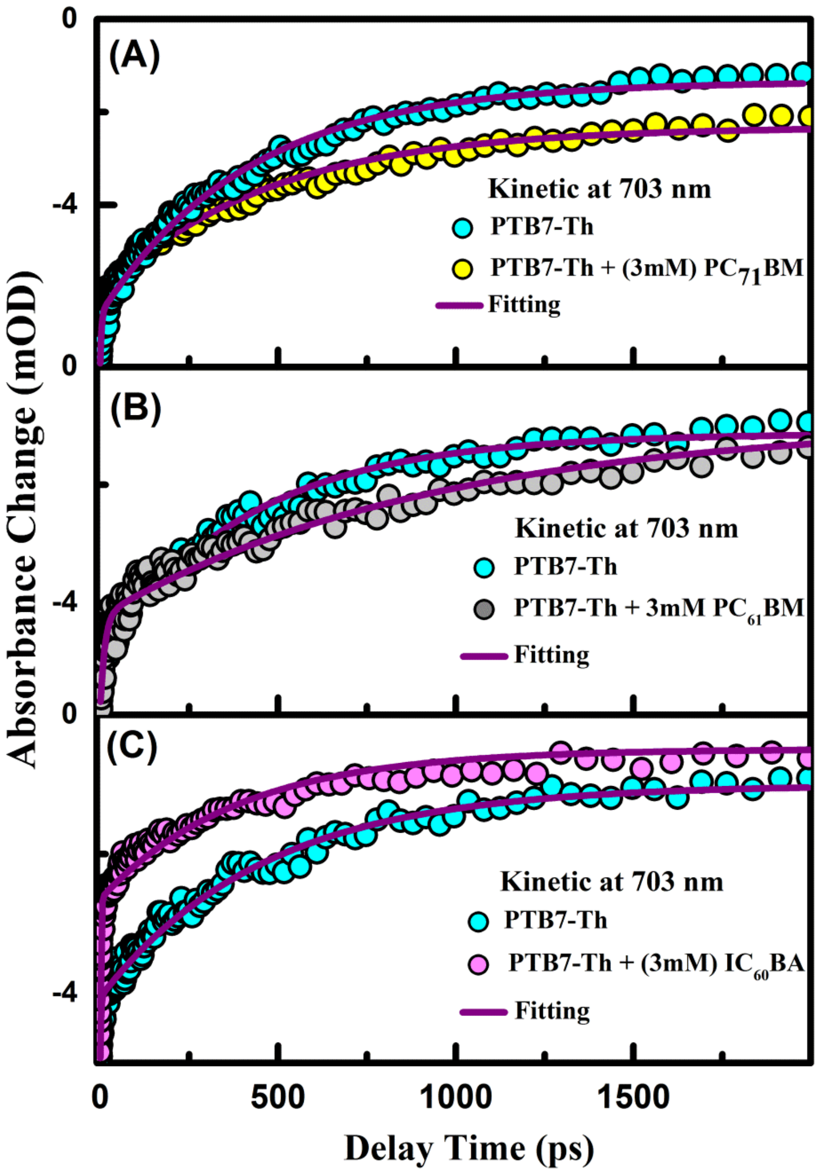

Figure 2.8 A rescaled kinetic profile (up to 2 ns) derived from fs-TA spectra at 703 nm of the donor polymer PTB7-Th in the absence (blue circles) and the presence of 3 mM $PC_{71}BM$ (A), $PC_{61}BM$ (B) or $IC_{60}BA$ (C). The solid lines represent best fits to the data obtained.

Figure 2.8 illustrates the kinetic profiles of the GSB of PTB7-Th at 703 nm in the absence and presence of FAs. Each time profile for GSB recovery of PTB7-Th shows a considerable difference in the presence of FAs compared to free PTB7-Th solutions. Compared to the free polymer, the GSB recovery with either $PC_{71}BM$ or $PC_{61}BM$ is slower, whereas the recovery with $IC_{60}BA$ is faster. These findings suggest that the CR of charge-separated ions is faster between PTB7-Th and $IC_{60}BA$ than the corresponding interaction with the other two FAs. This may be explained by the change in electron affinity, molecular structure, and carrier mobility as well as by the differences between the Fas in the LUMO and HOMO levels.[70] Global fitting analysis of the kinetic curves allows us to estimate the time constant for GSB recovery for the free polymer donor and that with the FAs. In addition to the fast CR of a few ps for a polymer with and without FAs, a long component of 563±18 ps for the free polymer, 881 ±23 ps in the presence of 3 mM $PC_{71}BM$, 815 ±37 ps in the presence of 3 mM $PC_{61}BM$ and 386 ±22 ps in the presence of 3 mM $IC_{60}BA$ is measured. In $PC_{71}BM$- and $PC_{61}BM$-based devices, CS and subsequently the formation of charge-separated ions is therefore considerably more efficient. In other words, excited-state CT between PTB7-Th and $PC_{71}BM$ and $PC_{61}BM$ produces long-lived charges, while that between PTB7-Th and $IC_{60}BA$ produces short-lived charges at the D/A interface. Note that the TA measurements at 760 nm are similar for polymer-fullerene solutions and polymer-fullerene-blended films as illustrated in Figure 2.9. The dynamics of the GSB recovery in PTB7-Th thin films at 720 nm are shown in the absence and presence of $PC_{71}BM$ and $IC_{60}BA$ in appendix B, Figure SB.2.

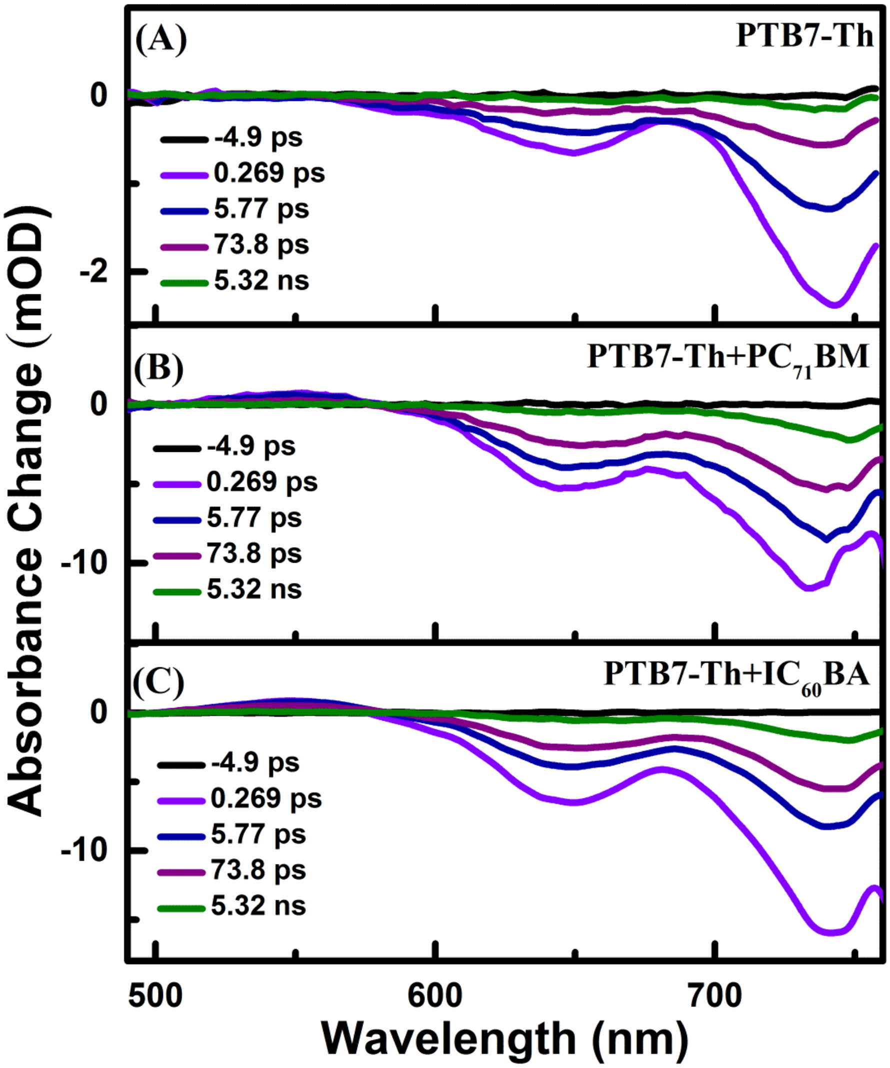

Figure 2.9 TA spectra of the PTB7-Th thin film in the (A) absence and (B and C) presence of FAs $PC_{71}BM$ and $IC_{60}BA$, respectively, excited at 760 nm. Delay times are as indicated in the figure.

Subsequently, we performed TA measurements within the NIR range for PTB7-Th in the presence and absence of $PC_{71}BM$ and each independent FA (Figure 2.10). The TA data for PTB7-Th shows a broad spectral feature between 1000 and 1350 nm in the presence of $PC_{71}BM$, which is in good agreement with that reported for their radical anions in the literature: 1347 nm for $PC_{71}BM$, [82] 1030 nm for $PC_{61}BM$ [83] and 1010 nm for $IC_{60}BA$[70].

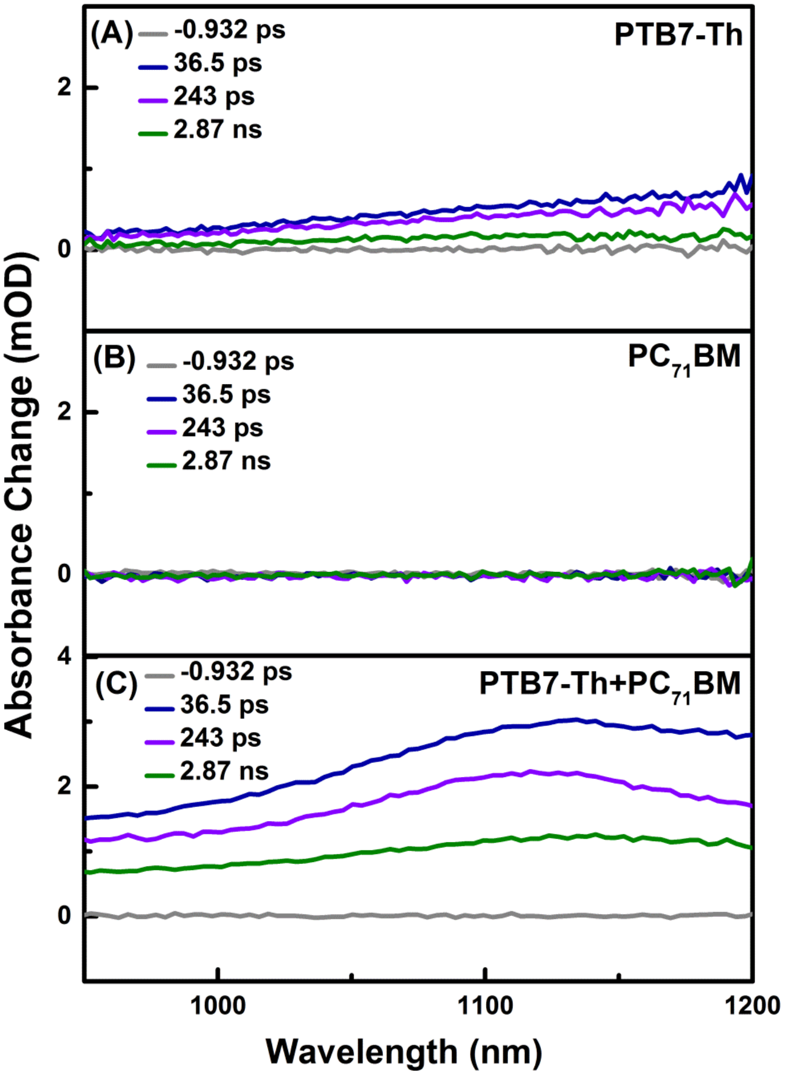

Figure 2.10 Transient absorption spectra of (A) PTB7-Th, (B) $PC_{71}BM$ and (C) PTB7-Th/ $PC_{71}BM$ pumped at 760 nm within the IR range. Delay times are as indicated in the figure.

According to the LUMO and HOMO energy levels of all the PTB7-Th/FA (as shown in Figure 2.11) complexes investigated here, the photoexcited polymer is expected to transfer an electron to all three fullerenes because the binding energy of the excitons is ca. 0.3-0.5 eV[84] after CS. Thus, a solar cell based on fullerenes as the molecular acceptor will considerably improve the performance of the device. We will test this hypothesis in the following section and discuss the good correlation obtained when we examined the performance of the device using each of the PTB7-Th/FAs studied here via electron/hole transfer in blended films.

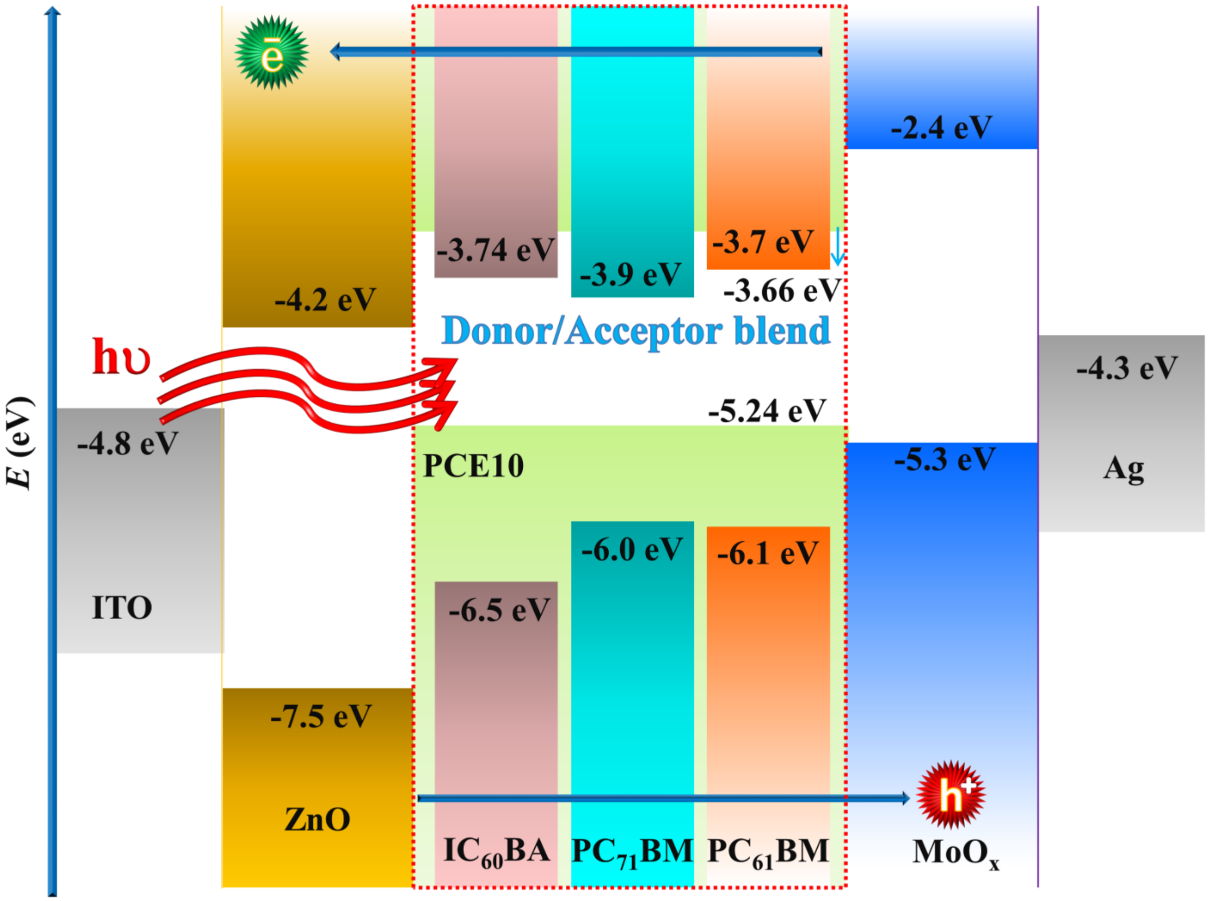

Figure 2.11 Schematic energy level diagram of the complete solar cell used in this study.

2.2.3. Morphology of the Electron Transporting Layer

Grain alignment of the ZnO electron transporting layer (ETL) is one factor that can improve device performance. Figure 2.12 shows scanning electron microscopy (SEM) and transmission electron microscopy (TEM) images from the morphological investigations performed on the ETL grown by radio frequency (RF) sputtering and used in the fabrication of solar cells. Further details of the experimental conditions and tools are reported in appendix A, section A4. A very smooth ZnO surface (rms roughness ≤ 2 nm) (Figure 2.12A) ensures a sharp interface between the ETL and the active layer, reducing leakage currents at the interfaces and thereby reducing the parasitic resistances in the overall performances of the devices.

SEM cross-sectional imaging is a unique tool to provide information about the sample, including the chemical composition, external morphology (texture), and crystalline structure and orientation of materials making up the sample. SEM clearly shows the densely packed vertical alignment of the grains (Figure 2.12B), an alignment that has been shown to boost the performances of solar cells by facilitating one-dimensional charge carrier transport. [85] We will explain this effect in upcoming sections.

TEM is a useful technique to provide fundamental structural and crystallographic information about the sample. Bright field (Figure 2.12C) and dark-field (Figure 2.12D) transmission electron microscopy (TEM) images demonstrate the highly crystalline, vertically aligned grains between 90 and 100 nm.

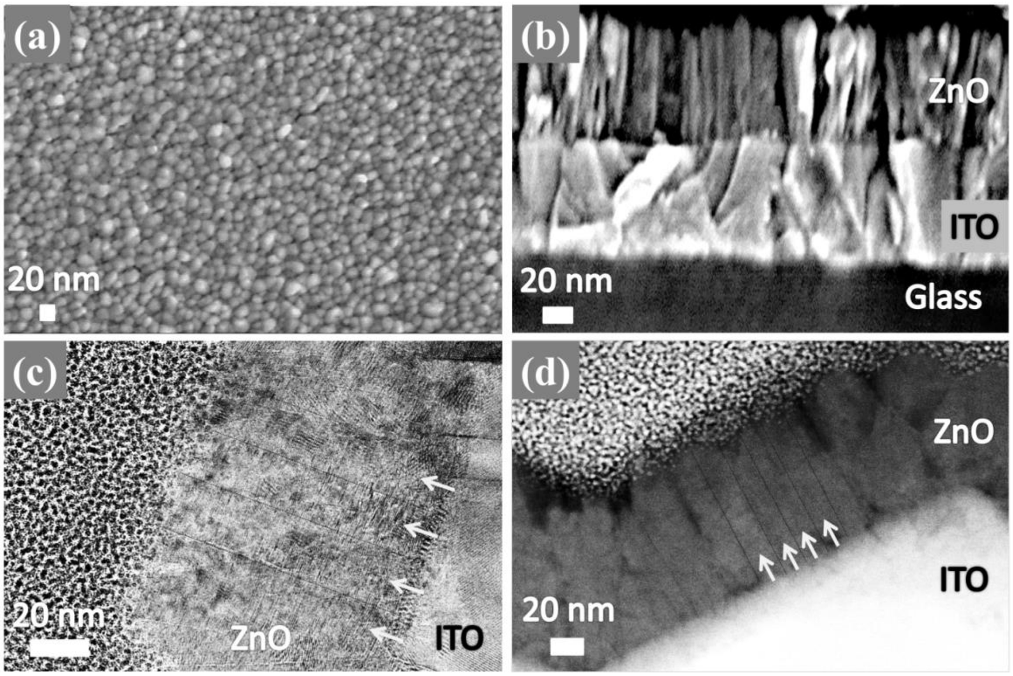

Figure 2.12 Electron microscopy images of the ZnO ETL. (A) An SEM image of the surface morphology, (B) an SEM cross-sectional image, (C) a bright-field TEM cross-sectional image and (D) a dark-field TEM cross-sectional image. The cross-sectional images show the vertically aligned nanorod-like grains of ZnO.

2.2.4. Device Fabrication

Based on the fact that organic materials require a suitable energetic offset to dissociate excitons, attempts at using single layer architectures have been comparatively ineffective, giving efficiencies on the order of 0.1% or less.[86] In 1979, based on layers of thermally evaporated small molecules, Tang reported the concept of a two component D/A that acted as the active layer for organic photovoltaics.[87] These systems were mainly controlled by the exciton diffusion length, and only excitons generated close the D/A interface lived long enough to dissociate at this interface.[88] In

1995, Yu et al. produced the first attempt at improving the D/A architectures by increasing the interfacial area of the D/A active layer, resulting in the solution-processed bulk-heterojunction (BHJ), which is considered the state of the art active layer morphology.[89] The BHJ architecture depends primarily on finding a balance between charge generation and transport, which is controlled by the lifetimes of the charge carriers.

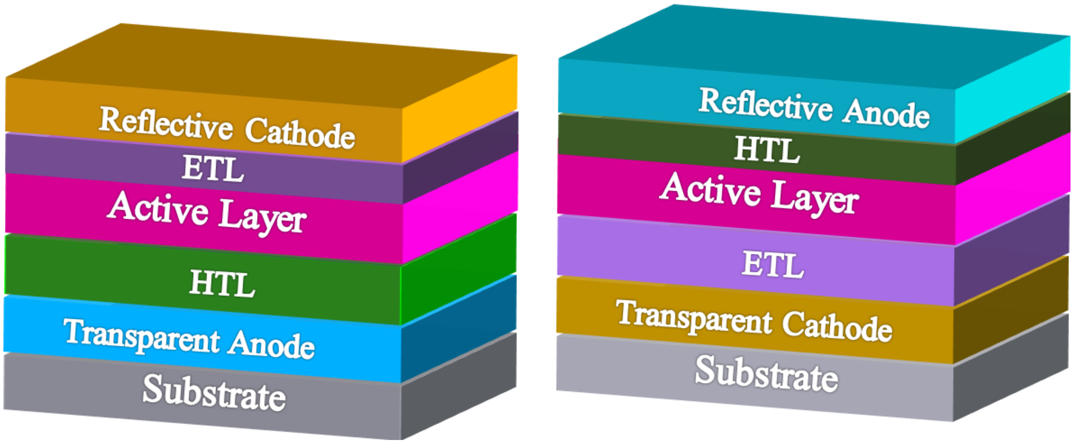

Figure 2.13 Schematic of BHJ device architectures. Typical (left) and inverted architecture (right).

Figure 2.13 illustrates the common device architectures of OPVs, comprising standard BHJs and inverted BHJs. Briefly, in a standard BHJ SC,[90] the active layer is sandwiched between an anode and a cathode, as drawn in Figure 2.13 (left). In this architecture, holes are transported to the anode, which consists of a substrate that is coated with a high work function transparent conducting electrode and improved with an interfacial hole selective/electron blocking layer between the electrode and the active layer. Tin-doped indium oxide (ITO) modified with a poly(ethylenedioxythiophene):poly(styrene sulfonic acid) (PEDOT:PSS) interfacial layer is the most common experimental material used in the OPV field for these electrodes. On the other side, electrons are transported to the cathode, which normally consists of a metal with a low work function beside a selective ETL between the active layer and the metal electrode. Alternatively, the inverted BHJ architecture was produced to help relieve device degradation. This architecture depends on the reverse of the electrodes roles of the charge collecting nature as a useful method to reduce the necessity for a low work function. In this technique, ITO is typically coated with a transition metal oxide, such as ZnO, which is known for its low work function, to make it suitable as the cathode by reducing its work function. On the other side, the anode typically is comprised of a stable metal, such as Ag or Au, that is functionalized with a high work function material, such as MoO_3 or other transition metal oxide interlayer, to improve stability.[5] In this work, the inverted BHJ configuration of glass/ITO/ZnO/PTB7-Th: FA/MoO_x/Ag was fabricated via the fabrication methods discussed in appendix A, section A5.

2.2.5. Device Characterization

The PCE of a PSC is proportional to the short circuit current (J_{sc}), open circuit voltage (V_{oc}), and fill factor (FF). The J_{SC} is mainly dependent on factors related to the efficiencies of every phase in the photovoltaic process, including the effectiveness of the light absorption of the active layer, exciton diffusion and dissociation at the D/A interface, charge transportation in the active layer, and charge collection transportation in the active layer. The V_{OC} in the OPV is mainly proportional to the energy level difference between the LUMO of the acceptor and the HOMO of the donor. Lower HOMO levels of the polymers would afford a higher V_{oc}.[91-92]

Here, the current density-voltage measurements were carried out with a Keithley 2400 source measurement unit and an Air Mass 1.5 G solar simulator with an illumination intensity of 100 mW cm^{-2}. The experimental details are discussed in appendix A, section A6. The current density-voltage characteristics of three D/A systems were studied in the bulk heterojunction solar cell configuration (i.e., glass/ITO/ZnO/PTB7-Th:FA/MoO_x/Ag) (Figure 2.14). The PTB7-Th/$PC_{71}BM$ system had better performance than PTB7-Th/$PC_{61}BM$ or PTB7-Th/$IC_{60}BA$ systems, supporting our spectroscopic investigations. Variations in device parameters for different D/A systems are shown and tabulated in the inset of Figure 2.14A. Comparative device statistics of various D/A system based solar cells used in the current study are summarized in Table 2.1. In this study there are some variables are considered such as (i) the active layer rotation speed, typically used three 600 rpm, 800 rpm, 1000 rpm. 800 rpm gave better results, (ii) drying the active layer PTB7: FAs under ultrahigh vacuum for 1 hr prior to evaporation of HTL and Ag layers, and (iii) ZnO sputter optimization at various temperatures for nanorod based morphology. The PTB7-Th/$PC_{71}BM$ system had the highest fill factor (FF) and current density (J_{sc}) compared to other D/A solar cell systems. However, the open circuit voltages (V_{oc}) of the $PCB_{71}M$ and $PCB_{61}M$ systems were slightly lower than that of the $IC_{60}BA$ system (Figure 2.14B), indicating the possibility of different interfacial recombination at D/A junctions. The prevalence of this recombination depends on the band alignments and space-charge distributions. The global basis for the high efficiency of the $PC_{71}BM$ system lies in its suitable frontier energy levels with PTB7-Th, which facilitates efficient photocharge generation compared to the $PC_{61}BM$ and $IC_{60}BA$ systems. The schematic band alignment [93-94] indicates a 1.26 eV energy level difference between the HOMO of the donor (PTB7-Th) and the FA ($ICB_{60}A$), suggesting the inefficient transfer of the hole back to the positive electrode. Additionally, spectroscopic kinetic traces show that the optimal complementary absorption spectra of the active layer increased the amount of light harvested.

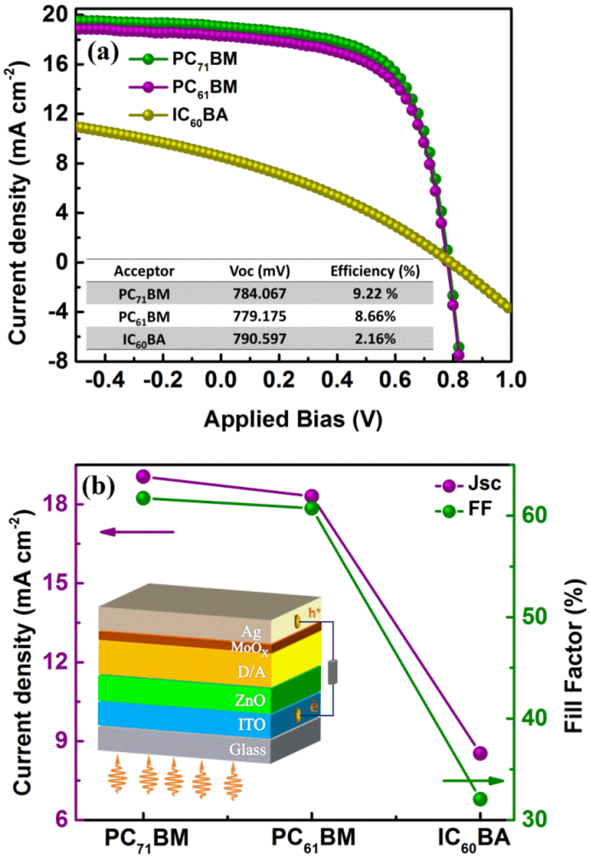

Acceptor	Voc (mV)	Efficiency (%)
$PC_{71}BM$	784.067	9.22 %
$PC_{61}BM$	779.175	8.66%
$IC_{60}BA$	790.597	2.16%

Figure 2.14 (A) The current density-voltage characteristic of the three different FAs and (B) variation of the device parameters as a function of various FAs. The highest efficiencies correspond to the champion cells in the current study for each D/A system.

Table 2-1 Comparative device statistics of various D/A system based solar cells used in the current study.

Device ID	J_{sc} (mA/cm^2)	V_{oc} (V)	FF (%)	Efficiency (%)
ITO/ZnO/ PTB7-Th:PC$_{71}$BM/MoO$_x$/Ag				
Device-1	19.565	0.785	59.9	9.20
Device-2	18.856	0.783	61.7	9.12
Device-3	19.333	0.783	58.8	8.89
Device-4	19.181	0.784	59.1	8.88
Device-5	19.057	0.784	61.7	9.22
ITO/ZnO/ PTB7-Th:PC$_{61}$BM/MoO$_x$/Ag				
Device-1	19.176	0.779	57.3	8.57
Device-2	18.854	0.775	57.2	8.37
Device-3	19.207	0.773	56.5	8.39
Device-4	18.358	0.782	60.3	8.66
Device-5	18.309	0.779	60.7	8.66
ITO/ZnO/ PTB7-Th:IC$_{60}$BA/MoO$_x$/Ag				
Device-1	8.022	0.712	31.4	1.79
Device-2	8.491	0.751	32.2	2.06
Device-3	8.610	0.760	32.4	2.12
Device-4	8.614	0.660	36.2	2.06
Device-5	8.533	0.791	32.1	2.16

2.3. ZnO Grain Effect

The grain growth of ZnO-sputtered films depends on a variety of factors, including the working deposition pressure, the partial pressure of argon and the temperature of the substrate. At temperatures above 200 °C, we observed the coalescence of adjacent grains by sintering to form a densely packed thin film with randomly oriented grains. Preliminary measurements yielded poor performance of the devices fabricated with ETLs deposited at higher temperatures.[85] However, by optimizing the deposition pressure and rate, columnar grains of ZnO could be obtained. Devices fabricated with ZnO grown at room temperature (RT) performed better than those with ZnO grown at higher temperatures. When ZnO grains are aligned vertically, the FF of the device improves because less CR occurs.[85] The faster unidirectional carrier transport of the carriers from the active layer (D/A) system through the ETL reduces dispersive losses in the J_{sc} characteristics. Thus, device statistics supported by spectroscopic traces further strengthen the photophysics-morphology-performance relationship that is urgently needed for further device optimization.

2.4. Conclusion

We have explored the significant impact of ultrafast CS and CR at D/A interfaces on device performance of a conjugated polymer PTB7-Th with three FAs: $PC_{71}BM$, $PC_{61}BM$ and $IC_{60}BA$. All D/A systems showed efficient ultrafast electron transfer from the donor to the acceptor. More specifically, the results from fs-TA demonstrated that the photoinduced CT from the PTB7-Th polymer to the FAs occurs on the sub-picosecond timescale, leading to the formation of long-lived radical ions. The speed of the CR at the

D/A interface strongly depends on the molecular acceptor. Here, we found increasing speed in the following order: $PC_{71}BM$ to $PC_{61}BM$ and $IC_{60}BA$. We also found that the PCE improves from 2% in $IC_{60}BA$-based solar cells to $>$ 9% in $PC_{71}BM$-based devices, supporting both the steady-state and time-resolved results. Additionally, we identified clear correlations among the grain alignment of the ETL, the carrier mobility of the FA, the CS, the CR and the device performance. These results clearly demonstrate that time-resolved laser spectroscopy and high-resolution electron microscopy can elucidate the basis for fabricating optimized solar cell devices.

CHAPTER 3

ULTRAFAST EXCITED-STATE DYNAMICS OF DIKETOPYRROLOPYRROLE (DPP)-BASED MATERIALS: STATIC VERSUS DIFFUSION-CONTROLLED ELECTRON TRANSFER PROCESS

3.1. Introduction

The expanding interest in flexible, lightweight, and cost-effective OPV cells as an alternative renewable energy resource has encouraged the scientific community to develop novel materials. Effective photocurrent generation requires materials to perform all of the essential steps efficiently, i.e., light absorption, exciton diffusion, charge separation, and charge transport.[95] One effective approach to increase solar spectrum absorption is to develop donor–acceptor π-conjugated chromophores as the donor materials for OPV devices. In this way, a π-electron-rich donor is combined with a π-electron deficient acceptor, resulting in a reduction in the bandgap compared to their individual bandgaps due to the interaction of their frontier orbitals. Using this approach, the efficiency of polymer solar cells has been improved up to 10%.[96] For instance, benzothiadiazole (BTD), diketopyrrolopyrrole (DPP), and naphthalenediimide (NDI)[97] have attracted particular interest in the OPV community.[97] Farnum et al.[98] were the first to introduce the DPP chromophore in 1974. This compound soon attracted considerable attention due to its bright red color, high melting point, high thermal stability, and promising photophysical properties.[99-100] In addition, DPP dyes are among the most common multipurpose π-conjugated molecular chromophores investigated for their potential for applications in optoelectronic devices including several techniques, such as dye-sensitized solar cells,[101] bulk heterojunction solar cells,[102] and organic field effect transistors.[103] However, while most studies on DPP have focused on its singlet excited state properties,[104] the triplet excited states are comparatively less investigated due to the low efficiency of the transition from singlet to triplet states (S_1–T_1 intersystem crossing (ISC)).[105] Considering the significance of triplet excited states in optoelectronic systems, it is vital to realize the properties of the triplet states in DPP chromophores. One approach to enhance the efficiency of the triplet excited state formation is to incorporate heavy metals in π-conjugated electronic systems to induce efficient singlet–triplet ISC by virtue of spin–orbit coupling brought by the mixing of the metal centered dπ orbitals with the π-electron system.[106-107] This technique has generally been utilized both to manage the cost of crucial knowledge about triplet chromophore properties and as a way to enhance the effectiveness of fundamental emission in phosphorescent light emitting diodes.[108] Even though heavy-metal complexes have been the focus of intense research activities devoted to the fields of light-emitting devices,[109-110] bioimaging,[111-112] sensing,[113-114] and sensitization, [115-116] there are very few studies on heavy-metal-substituted DPP complexes. Langhals et al. introduced numerous transition metals, such as Au(I) and Pt(II), that were coordinated to the DPP amide nitrogens with the goal of improving the fluorescence quantum yield of the DPP chromophores;[117] nevertheless, the photophysics of the complexes were controlled by the ligand singlet excited state, indicating the comparatively poor interaction between the π-conjugated electronic system of DPP and the central metal. Recently, Ziessel, Castellano and co-workers published an interesting study with platinum- and iridium-containing DPP oligomers that revealed efficient ISC resulting in a long-lived triplet excited state.[105, 118]

Platinum acetylide π-conjugated polymers and oligomers have been broadly researched because of the ability of the central metal to prompt strong-spin orbit coupling, which frequently induces effective phosphorescence and enhances triplet yield.[106, 119] Because the triplet exciton shows a longer lifetime compared to the singlet exciton, materials consisting of platinum acetylide and polymers have been investigated in photovoltaic devices as the active materials with the goal of improving the exciton diffusion.[120] In particular, square-planar coordinations of Pt(II) complexes have attracted considerable interest due to their high ISC efficiencies (φ_{ISC}) facilitated by strong interactions between the dπ orbitals of the metal and pπ orbitals of the chromophore.[106, 121-125] The photophysical properties of Pt(II) complexes strongly depend on the chemical structures of the cyclometalated ligands, where the emission energies of the complexes are related to the planarity and π-conjugation of the chromophoric ligands.[126] Pt(II) complexes bearing π-conjugated polymers and oligomers are promising for use in organic photovoltaic (OPV) applications due to their efficient light harvesting, structural versatility, and intrinsic charge-transport behavior.[127-128] Specifically, extending the polymer chain or the π-conjugation of the ligand π-conjugation mostly affects the intra-ligand excited states, leading to a red shift in absorption and emission spectra and thus controlling the higher-lying metal-to-ligand charge transfer (MLCT) state and the HOMO−LUMO gap. The combination of low-energy MLCT transitions of these complexes with their long excited-state lifetimes makes them valuable for photosensitization applications.[129-130] The effects of the π-conjugation length of the oligomers and the incorporation of Pt(II) as a metal center on ISC, singlet−triplet and triplet−triplet energy transfer, and OPV cells have been explored.[131]

Recently, Schanze and co-workers reported a comparative photophysical and electrochemical study of platinum acetylide and cyclometalated platinum complex auxochromes with diketopyrrolopyrrole π-conjugated chromophores.[125] The cyclometalated platinum auxochromes showed stronger spin–orbit coupling and increased excited state delocalization compared to the platinum acetylide system.

In addition, Gould and Rosspeintner reported valuable information about bimolecular electron transfer reactions by studying the interactions in solution between Pt(II) complexes and porphyrins, which act as electron acceptor molecules, forming electron donor-acceptor (EDA) systems.[132-134] Vertical excitation of the EDA system generates a substantial vibrational energy with various active modes that facilitate photoinduced electron transfer (PET) processes.[135-136] The rate constant of the dynamic PET mechanism is determined by diffusion of the reactants,[134] limiting the rate constant of diffusion. In contrast, the PET process is ultrafast (i.e., on the picosecond time scale), and no diffusion is needed for an entirely static quenching mechanism.[134] Understanding the underlying mechanisms controlling ISC and PET dynamics is, therefore, central to fundamental studies.[125]

Recently, a new class of Pt(II)(acac) (acac = acetylacetonato) complexes bearing π-conjugation-rich diketopyrrolopyrrole (DPP) oligomers has been synthesized, and their photophysical properties have been explored in the absence and presence of a porphyrin compound using ultrafast time-resolved absorption spectroscopy.[22]

In this work, we continue our investigation of the bimolecular PET from DPP-Pt(II)(acac) to an electron acceptor in DMF/DCM (4:1) mixtures by focusing on tetracyanoethylene (TCNE) as the electron acceptor. The chemical structures of the materials used in this study are shown in Figure 3.1. TCNE was selected due to its strong electron-accepting ability, unique relaxation processes, lack of spectral overlap with the donor, CT-state lifetimes in TCNE-based electron donor-acceptor systems,[137-138] and ability to form different complex geometries.[139] Here, we predict that the DPP-Pt(II)(acac)/TCNE system can form CT complexes, thereby displaying interesting photophysical properties including ultrafast PET, rapid CS, and slow CR. In particular, the incorporation of Pt(II) can control the ISC and PET dynamics from the oligomer to TCNE. We evaluated the effect of incorporating Pt(II) in ISC and PET processes by comparing and analyzing the photoexcited dynamics of DPP-Pt(II)(acac)/TCNE and DPP/TCNE systems.

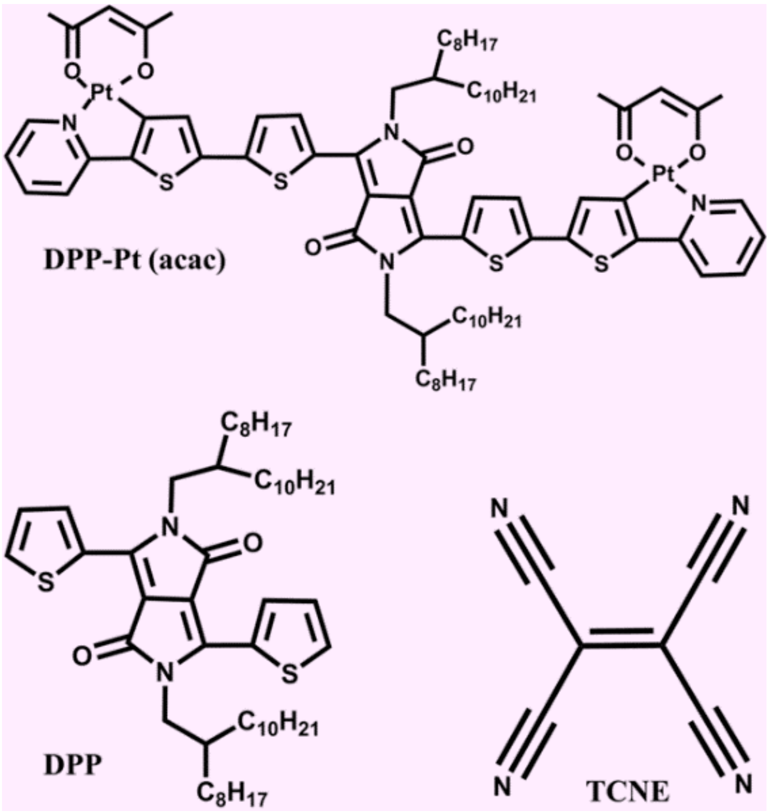

Figure 3.1 Chemical structures of the materials used in this study, DPP-Pt(acac), DPP and TCNE.

3.2. Results and Discussions

3.2.1. Steady-State Absorption and Emission Spectra

The absorption and fluorescence spectra of DPP-Pt(acac) with the successive addition of TCNE are recorded. The experimental details with conditions are provided in appendix A, section A3(I).

A. DPP-Pt(acac) Oligomer/TCNE System

As shown in Figure 3.2 A, the absorption spectrum of DPP-Pt(acac) has two peaks at 620 and 670 nm. The spectral absorption feature is modified significantly upon the addition of TCNE: the initial 670 nm band suffers from a successive decrease with increasing TCNE concentration, and a new shoulder develops at 725 nm. Note that TCNE is transparent in the visible region with an absorption in the range 250–400 nm in the applied solvent, thus indicating a ground-state interaction between DPP-Pt(acac) and TCNE likely due to the formation of a CT complex. This CT complex is expected to have a broad absorption spectrum that overlaps with the absorption of free DPP-Pt(acac). We recorded the excitation spectrum to better assign this CT band (see the inset in Figure 3.2). From the recorded excitation spectrum, we anticipate the CT band to be a broad band in the 500–700 nm range with a maximum at 595 nm. Indeed TCNE, as an acceptor with modest oxidation[140] and reduction potentials of -0.26 V vs Ag/Ag$^+$,[141-142] has the potential for application as an acceptor to a divalent group of 10 transition-metal complexes.[143-144] Excitation of the CT complex gives rise to an emission feature extending over the range of 640−850 nm centered at 700 nm with a vibrionic shoulder at 760 nm.

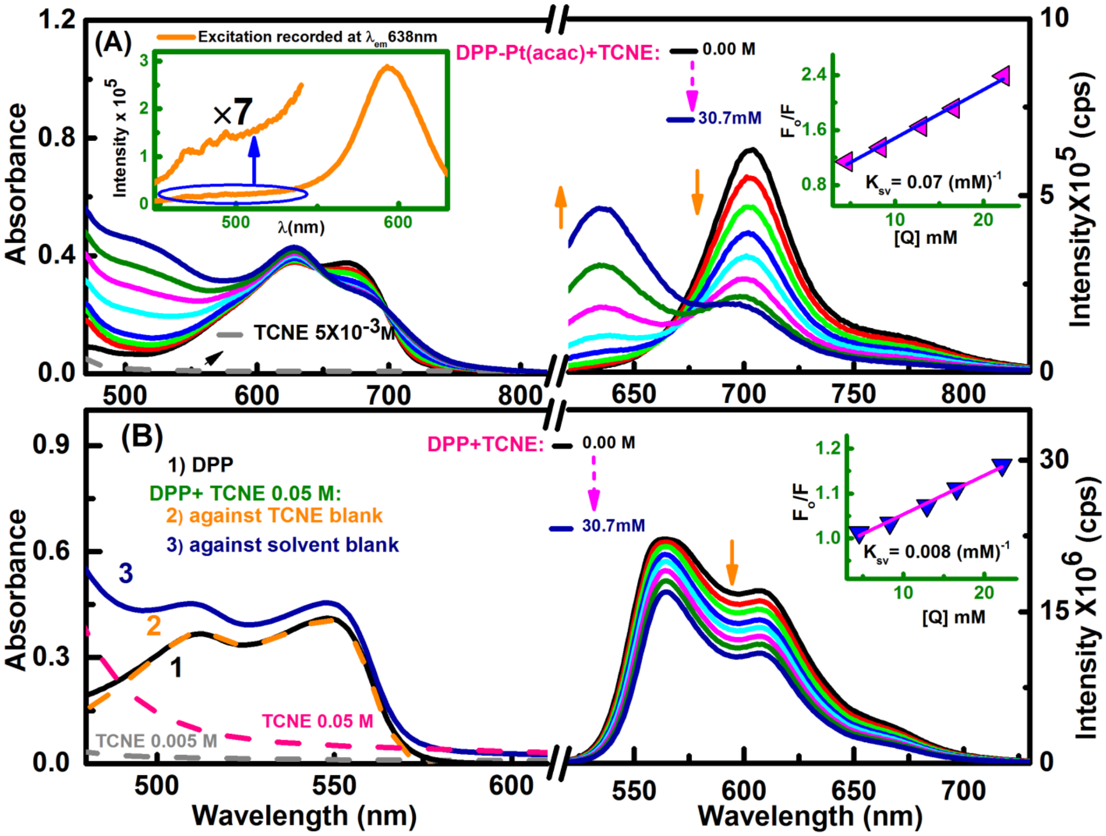

Figure 3.2 (A) Steady-state absorption (left) and emission (right) spectra after excitation at 600 nm of the DPP-Pt(II)(acac) complex. (B) Steady-state absorption (left) and emission (right) after excitation at 490 nm of DPP at different indicated concentrations of TCNE. Insets are (A) excitation spectrum of DPP-Pt(acac)/TCNE recorded using λ_{em} = 638 nm (left), Stern-Volmer plot (right), and (B) Stern-Vomer plot (right).

Successive addition of TCNE results in quenching of the DPP-Pt(acac) fluorescence, suggesting that the PET from the photoexcited DPP-Pt(acac) to the TCNE is followed by the development of a new emission band centered at 635 nm. The blue-shifted emission of the CT complex of DPP-Pt(acac)/TCNE indicates its slightly higher emission energy than that of DPP-Pt(acac). The impact of planarization of the π-electron system on the frontier orbital energy in the DPP-Pt(acac) is depicted in the literature.[125] Structural changes are known to have the potential to be induced by interacting with TCNE.[145-146] This implies that DPP-Pt(acac) and TCNE interact predominantly via static interaction, as supported by the quenching process, and leads to the expectation that less conjugation of the DPP units with the two Pt(II) centers is typical of the excited state.

B. DPP Oligomer/TCNE System

Figure 3.2B illustrates our efforts to evaluate the effects of incorporating Pt(II). It shows absorption and fluorescence spectra of the Pt oligomer metal-free DPP with successive addition of TCNE. In the absence of TCNE, the absorption peaks of DPP in DMF/DCM (4:1) are located at 512 and 548 nm. The absorption of DPP shows no change upon addition of TCNE; hence, the formation of a CT complex is unlikely. Moreover, as discussed below, the rate of PET from the excited DPP to TCNE is very slow (on the few ns time scale), which allows us to rule out the formation of a static ground state complex. Emissions are in the range of 530−700 nm with two peaks at 564 and 607 nm. TCNE induces slight quenching (~30%) in DPP emission, which is in support of the absence of a static ground state complex. This suggests that the quenching of DPP emissions that occurs upon TCNE interaction may be caused by dynamic or diffusion controlled mechanisms. In a later section, we discuss the ISC and PET from excited DPP-Pt(acac) and DPP to TCNE.

C. Stern Volmer Plot

To explore the nature of the kinetics of the PET, we constructed a Stern-Volmer plot using the equation $I_0/I = 1 + K_{SV}[Q]$,[77] where (I_0) and (I) are the fluorescence intensity of the corresponding oligomers under investigation in the absence and presence of quenchers, respectively, and (K_{SV}) is the SV quenching constant. The insets in Figure 3.2(A, B) illustrate SV plots and constants where the estimated quenching rate constants (K_q) are found to be 5.3×10^{11} M^{-1} s^{-1} and 1.3×10^{9} M^{-1} s^{-1} for DPP-Pt(acac) and DPP, respectively. Thus, with the diffusion limit in DMF at $\sim 10^{9}$ M^{-1} s^{-1}, it is clear that DPP quenching is within the diffusion limit, whereas DPP-Pt(acac) is much faster than the diffusion limit, which agrees with the anticipated mechanisms of interaction.

3.2.2. Excited-State Dynamics

A. DPP-Pt(acac) Oligomer/TCNE System

To gain further insight into the excited-state dynamics of DPP-Pt(acac), time-resolved TA spectroscopy of DPP-Pt(acac) was performed in DMF/DCM(4:1) in the presence and absence of TCNE as illustrated in Figure 3.3. The spectra were measured following a 560 nm laser pulse excitation. Further experimental details are provided in appendix A, section A3(II). In the absence of TCNE (Figure 3.3A), excitation of DPP-Pt(acac) resulted in a strong negative absorbance band corresponding to the ground state bleach (GSB) and a broad excited-state absorption (ESA) at 670−820 nm. The broad ESA was assigned to the DPP-Pt(acac) triplet state as a result of ISC on a time scale of 130 ps.[22] In the presence of 0.05 M TCNE, in addition to the GSB of the DPP-Pt(acac)/TCNE system, the formation of a new featureless band over the range of

700−800 nm with a shoulder at 715 nm appears rapidly after excitation (Figure 3.3B). This new featureless band can be attributed to the radical cation of DPP-Pt(acac)[22] in response to the PET from the excited DPP-Pt(acac) to TCNE. This band becomes more obvious in the presence of higher TCNE concentrations, as shown in Figure 3.3C. This shoulder at approximately 715 nm is in good agreement with that reported for the radical cation of the oligomer.

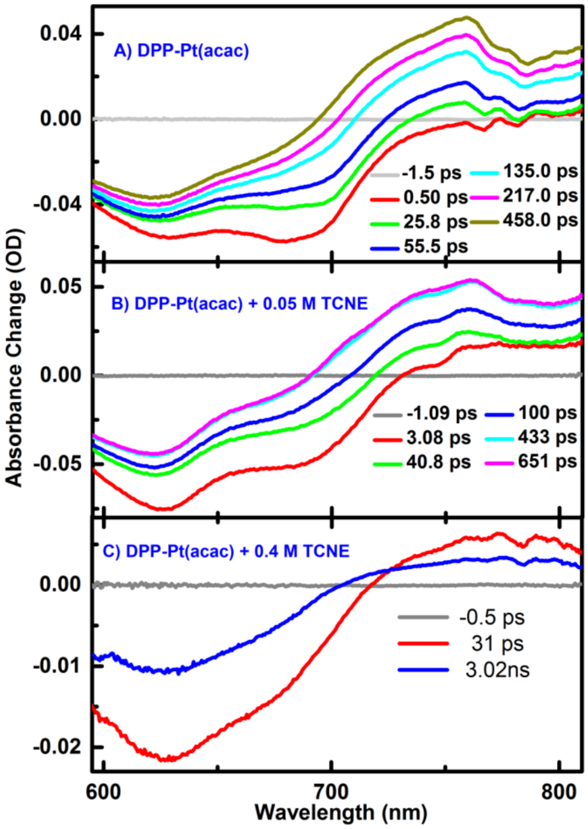

Figure 3.3 Transient absorption spectra (ΔA) observed at time delays from sub-ps to a few hundred ps for DPP-Pt(II)(acac) in the absence of TCNE (A), in the presence of 0.05 M TCNE (B), and in the presence of 0.4 M TCNE (C) after excitation at 560 nm.

Moreover, the dynamics of this band appeared to show a significant change over a 3 ns time window, which is much shorter than the triplet state lifetime, which is known to be 0.16 μs.[17] This new band is observed at a very early time delay (~3 ps), which is in favor of an ultrafast PET mechanism. The thermodynamic feasibility of the excited-state electron transfer is estimated by the change in the Gibbs free energy (ΔG^o), which is an important parameter that pertains to the driving force of electron transfer reactions.[147] From the reduction potential of TCNE (-0.26 V vs Ag/Ag+)[141-142], the oxidation potential, and the singlet excited-state energy of DPP-Pt(acac) (+0.79 V vs Ag/Ag+ and 1.82 eV, respectively),[22, 125] the ΔG^o is estimated to be -0.77 eV, indicating that PET is thermodynamically feasible.

The results shown in Figure 3.4 for the kinetics of ESA and GSB at different TCNE concentrations clearly shows the rise of the triplet state of DPP-Pt(acac) in the absence of TCNE and the ultrafast PET from the excited DPP-Pt(acac) to TCNE in the presence of an electron acceptor. The exponential fit to the ESA data shown in Figure 3.4 (A) suggests that the rate of singlet-to-triplet ($S_1 \rightarrow T_1$) ISC of DPP-Pt(acac) is ~130 ps, in agreement with that reported earlier.[22] On the other hand, analyses of the kinetic traces collected in the presence of TCNE reveal the presence of two kinetic components of 3.32 (44%) and 128.84 (56%) and 4.19 (70%) and 123.69 (30%) for 0.02 and 0.05 M TCNE, respectively.

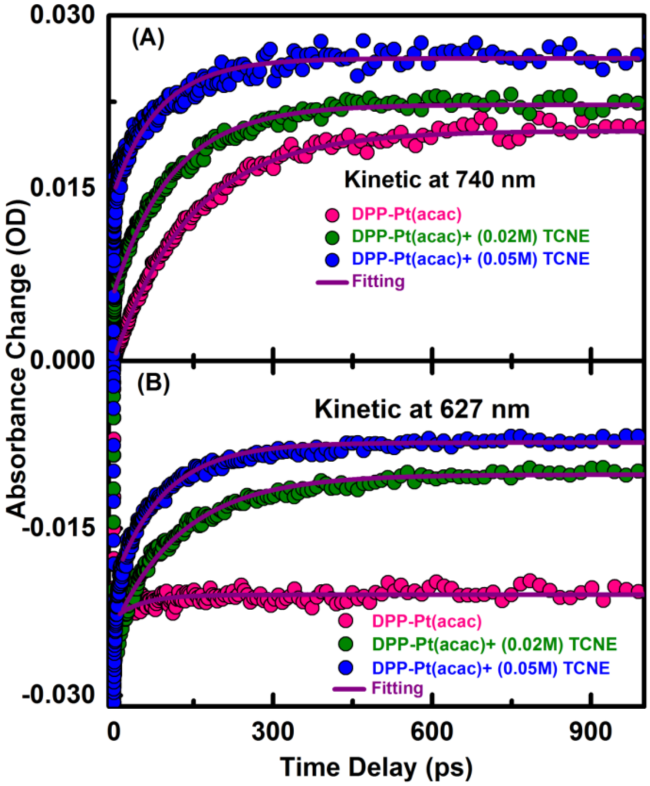

Figure 3.4 A rescaled time profile (up to 1 ns) of ESA kinetics at 740 nm (A) and GSB at 627 nm of the DPP-Pt(II)(acac) complex in the presence and absence of TCNE (B). The solid lines represent the best fits to the obtained data.

Taking the above discussed steady-state measurements and the radical cation formation in the area of TA into consideration, we can assign the fast component for the PET from the DPP-Pt(acac) to TCNE. This indicates that PET from the excited DPP-Pt(acac) to TCNE is ultrafast (i.e., 3-4 ps), similar to that of DPP-Pt(acac) to the positively charged porphyrin[22] but much faster than the ISC of DPP-Pt(acac) or the PET processes in bimolecular systems without metal centers.[148-150] An ultrafast electron transfer that is much faster than ISC indicates that the PET reaction occurs from the singlet excited state rather than the triplet state. In addition, an ultrafast PET is evidence for a strong electronic coupling between DPP-Pt(acac) and TCNE. In addition, the longer lifetime component may be due to free DPP-Pt(acac), which decreases with increasing TCNE concentration, as indicated by the amplitudes. As shown in Figure 3.4 (B), in the absence of TCNE, the GSB is dominated by a slow component of recovery, where the time constant is much longer than the observation time window (1 ns). In the presence of TCNE, in addition to the existence of a long time component, we observed a short time component within a few hundred ps, which can be assigned to fast CR from the TCNE$^{-\bullet}$ to DPP-Pt(acac)$^{+\bullet}$. The long-lived component is due to the long-lived radical cation and the triplet state of DPP-Pt(acac).

B. DPP Oligomer/TCNE System

I. fs-Transient Absorption Spectroscopy

To evaluate the role of Pt(II), we monitored the excitation dynamics of the un-metallated chromophore, DPP. Figure 3.5A shows TA spectroscopy of DPP after a 560 nm laser pulse excitation in the absence of TCNE. The excitation of the DPP oligomer results in a GSB below 650 nm and a broad ESA between 670 and 820 nm immediately after excitation. The broad ESA could be assigned to the DPP singlet state, as indicated by the very fast formation at a temporal resolution of 120 fs. Figure 3.5B shows the comparison of the excitation dynamics of DPP in the presence and absence of TCNE during the early time delays. The presence of TCNE causes a slight increase in the rates of both ESA decay and GSB recovery. The absence of ultrafast PET from the excited DPP to TCNE indicates the lack of a CT complex in the DPP/TCNE system, which is consistent with the results of steady-state absorption and fluorescence measurements. Thus, communication between DPP and TCNE in the solution is expected to occur through dynamic interactions. As seen in Figures 3.3 and 3.4, a clear and fast change in the transient spectra and its dynamics are observed for the DPP-Pt(acac)/TCNE system compared to the DPP metal-free system.

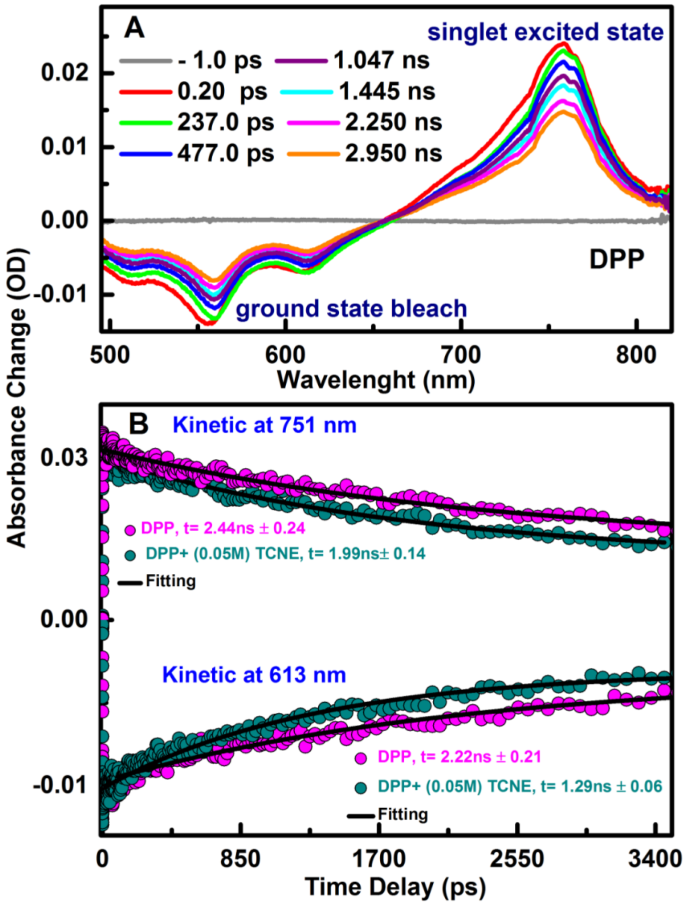

Figure 3.5 Transient absorption spectra (ΔA) observed at time delays from sub-ps to a few ns for DPP in the absence of TCNE after excitation at 560 nm (A). A rescaled time profile (up to a few ns) of the transient absorption kinetics of an ESA at 751 nm and GSB at 613 nm for DPP in the presence and absence of 0.05 M TCNE (B). The time constants extracted from the fitting are indicated.

II. ns-Transient Absorption Spectroscopy

To evaluate the PET from the photoexcited DPP to TCNE through dynamic interactions, we monitored the TA spectra at long time delays from sub-ns to approximately 14 ns, as shown in Figure 3.6. In the absence of TCNE (Figure 3.6A), DPP shows GSB at 559 nm, stimulated emission (SE) at 610 nm, and an ESA centered at 751 nm. The ESA decay, which can be safely ascribed to the depopulation of the singlet state with a time constant of 6.07 ns, simultaneously with the GSB recovery, indicates the relaxation of the singlet state to the ground state. Even though the spectral shape of the DPP/TCNE system in early time delays are similar to those of DPP, a new broad positive band centered at 600 nm arises in the ns time delays in the presence of TCNE (see Figure 3.6B). This new band is most likely due to the long-lived DPP cation radical. This indicates that there is PET from the excited DPP to TCNE. The PET caused a more than 4-fold increase in the rate of ESA decay and GSB recovery of the DPP/TCNE system than those of DPP in the absence of TCNE, as indicated in Figure 3.7A for DPP in the presence of 0.10 M TCNE.

III. Time-correlated single-photon counting (TCSPC)

The dynamic nature of the interaction mechanism between DPP and TCNE is also concluded from the TCSPC measurements given in Figure 3.7B. The fluorescence lifetime for DPP in the absence of TCNE is clearly decreased after adding TCNE, confirming the dynamic nature of the interaction.[151] By fitting the data with a single exponential decay function, the lifetimes of DPP in the presence and absence of 0.10 M TCNE were found to be 1.52 and 6.08 ns, respectively. We extracted the PET rate from the fluorescence lifetime change and estimated it at ≈5×10^{8} s^{-1}. This rate is slower than the diffusion rate of TCNE, which was calculated using Stokes-Einstein equation to be 7.02×10^{9} M^{-1} s^{-1}, supporting the suggested dynamic mechanism of interaction. Further experimental details are provided in appendix A, section A3(III).

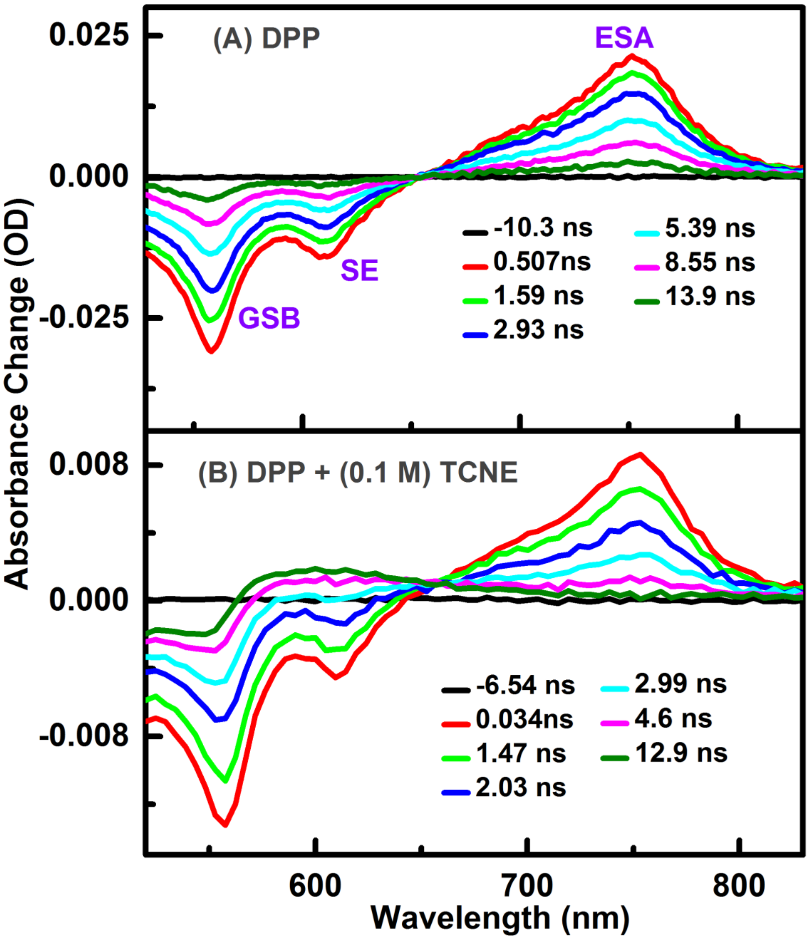

Figure 3.6 Transient absorption spectra (ΔA) observed at different time delays from sub-ns to approximately 14 ns for DPP in the absence of TCNE (A) and in the presence of 0.1 M TCNE after excitation at 500 nm (B).

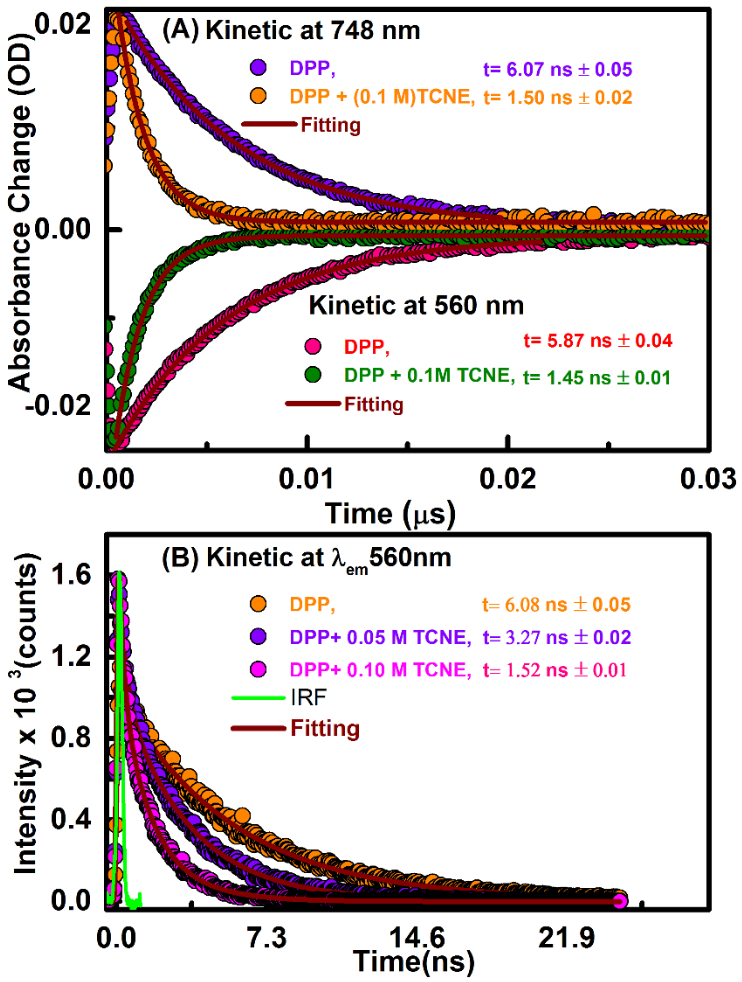

Figure 3.7 A rescaled time profile (up to 30 ns) of the transient absorption kinetics of ESA at 748 nm and GSB at 560 nm of DPP in the presence and absence of 0.1 M TCNE after laser excitation at 500 nm (the time constants extracted from the fitting are indicated) (A); TCSPC of DPP in the presence and absence of 0.05 and 0.1 M TCNE after laser excitation at 500 nm (the time constants extracted from the fitting are indicated) (B).

3.3. Effect of Pt(II)

The above observations clearly indicate the effects of incorporating Pt(II) on the excitation dynamics, ISC, and PET of DPP. We propose that the incorporation of Pt(II) increases the planarity and π-conjugation of the DPP moiety, thus reducing the HOMO−LUMO gap energy, as is evidenced by a red-shift of the absorption bands (Figure 3.2). The most influential role of Pt(II) is how it facilitates interactions with TCNE by forming a CT complex and enhancing electronic coupling between the DPP-Pt(acac) complex and TCNE; it is usually assumed that the electronic coupling strength increases exponentially with an inverse distance between the electron donor and acceptor.[152] The acceleration of ISC from ns domain to 130 ps is a central Pt(II) role in this system. Although the redox properties and energy levels of singlet and triplet excited states of DPP are modified by the incorporation of Pt(II), the low reduction potential of TCNE allows electron transfer from the excited DPP-Pt(acac) or DPP to TCNE. The oxidation potentials of DPP and DPP-Pt(acac) are 0.53 and 0.28 vs Fc/Fc^+, respectively.[125] Given that the singlet excited-state energy of DPP and DPP-Pt(acac) are at the same level (1.9 and 1.8 eV, respectively), the driving force for the electron transfer (ΔG^o) from the excited DPP or DPP-Pt(acac) to TCNE are comparable on the same order of magnitude. Thus, the ultrafast PET in the case of DPP-Pt(acac) to TCNE is likely to be facilitated by the Pt centers, which may increase the planarity and π -conjugation. While interaction between DPP and TCNE appear to be diffusion controlled, as indicated by the steady-state and time-resolved measurements, incorporation of Pt(II) induces the CT complex with TCNE in the ground state and facilitates ultrafast PET from DPP-Pt(acac) in the singlet excited state to TCNE.

3.4. Conclusion

In this work, we present a detailed study of the excited-state dynamics of DPP-Pt(acac)/TNCE and DPP/TCNE systems in DMF:DCM (4:1) using time-resolved broadband transient absorption and emission spectroscopies. The results indicate that a Pt(II) center is essential to controlling the PET mechanism from the donor (DPP-Pt(acac) or DPP) to the TCNE electron acceptor. Steady-state and time-resolved data demonstrate that the most influential role of incorporated Pt(II) is to facilitate interactions between DPP-Pt(acac) with TCNE, resulting in the formation of a CT complex, which, in contrast, is absent from the DPP/TCNE system. The temporal evolutions of the TA spectra were analyzed to elucidate the PET from the excited DPP-Pt(acac) and DPP to the TCNE. The TA results show the possibility of switching the reaction mechanism from a diffusion-controlled process to a static process by incorporation of a Pt metal center into the DPP.

CHAPTER 4

ULTRAFAST PHOTOINDUCED ELECTRON TRANSFER IN A π-CONJUGATED OLIGOMER/PORPHYRIN COMPLEX

4.1. Introduction

In 1986, Tang reported the construction of the first bilayer organic photovoltaic (OPV) cell using copper phthalocyanine and perylene tetracarboxylic derivatives.[153] The key photophysical processes in this type of device are exciton generation in the light-absorbing phase, exciton dissociation at the interface, and free charge carrier migration and collection at opposite electrodes.[154,155] Since this first report, the search for donor and acceptor candidates for solar cells has rapidly expanded.[156-158] In this respect, porphyrins, the essential chromophores in nature's most efficient energy conversion device,[159] have received particular attention due to their excellent thermal stabilities, strong visible light absorptions, and remarkable photoelectrochemical properties.[160-162] In addition, a vast array of research pertaining to π-conjugated polymers and oligomers has been motivated by their efficient light harvesting, structural versatility, and intrinsic charge transport behavior.[127-128] As we discussed in chapter 3, there has been recent specific interest in diketopyrrolopyrrole (DPP)-based donor-acceptor-donor oligomers in OPV applications due to the excellent light harvesting properties of this chromophore. Stemming from our special interest to observe the effect of the incorporation of heavy metals into π-conjugated chromophores for the exploration of the triplet state and its impact on solar cells, we tried to explore metallated DPP derivatives.[131, 163-165]

In this chapter, we extended our investigation to study the interaction between 5,10,15,20-tetra(1-methyl-4-pyridino)porphyrin tetra(chloride) (TMPyP) and 5,10,15,20-tetra(4-pyridyl)porphyrin (TPyP) with DPP-Pt(acac) in dichloromethane (DCM):dimethylformamide (DMF) mixtures. The chemical structures of all materials used in this study are shown in Figure 4.1. Interestingly, unique ground- and excited-state charge transfer (CT) interactions between cationic porphyrin and the organometallic π-conjugated oligomer are observed. The TMPyP/DPP-Pt(acac) system exhibits a specific ground state interaction that brings the chromophores into close molecular proximity, allowing ultrafast photoinduced CT to occur, which is then probed by femtosecond (fs) transient absorption spectroscopy. Interestingly, unlike many other charge transfer systems,[148-150, 166] the CT from DPP-Pt(acac) to TMPyP is ultrafast, and the CR is very slow, which makes the current donor-acceptor system promising for potential applications in organic solar cells.

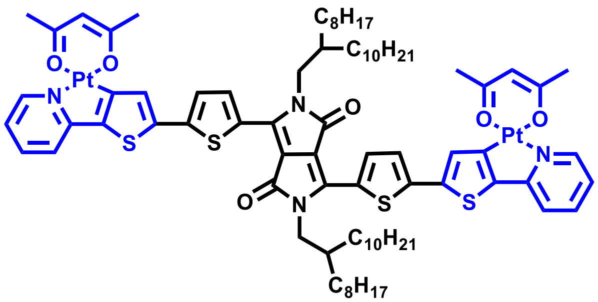

DPP-Pt(acac)

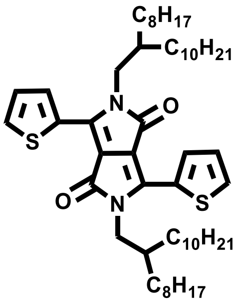

DPP

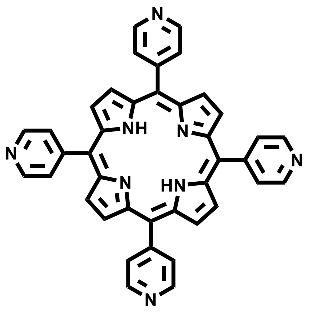

TPyP

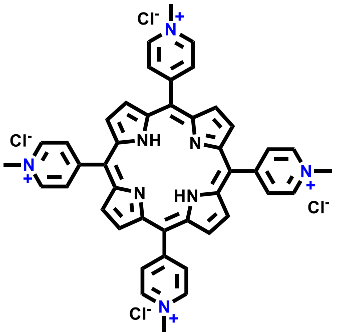

TMPyP

Figure 4.1 Schematics of the chemical structures of DPP, DPP-Pt(acac), TPyP, and TMPyP, which are used in this study.

4.2. Results and Discussions

4.2.1. UV-Visible Absorption and Photoluminescence Spectroscopy

The absorption and fluorescence of DPP-Pt(acac) during the successive addition of TMPyP were recorded. The experimental apparatus and conductions are described in appendix A, section A3(I). As shown in Figure 4.2A, the ground state absorption of DPP-Pt(acac) features a 0-0 transition band with λ_{max} ~ 670 nm (ε ~ 42,000 $M^{-1}cm^{-1}$).[125] Free-base TMPyP exhibits an intense Soret-band (S_0-S_2) at 424 nm and four Q-bands (S_0-S_1) over the range 500-630 nm**.**[167-168] No significant change is observed in the absorption of DPP-Pt(acac) upon the addition of TMPyP, while only a slight red-shift of approximately 5 nm is observed in the ground state absorption of TMPyP, indicating a ground-state interaction between the DPP-Pt(acac) and TMPyP chromophores. Photoluminescence spectroscopy (see Figure 4.2B) of DPP-Pt(acac) reveals a broad fluorescence band extending over the range 600-850 nm with a maximum and vibrionic shoulder at 707 and 750 nm, respectively. Successive addition of TMPyP resulted in efficient quenching of the DPP-Pt(acac) fluorescence with a Stern-Volmer constant K_{SV} ~ 2.2 x 10^4 M^{-1} (extrapolated from the low quencher concentration).

Stern-Volmer Plot

As seen in the inset of Figure 4.2B, the Stern-Volmer plot exhibits upward curvature, suggesting a mixed dynamic and static quenching mechanism for the DPP-Pt(acac) fluorescence by TMPyP. However, a straight line is obtained for a modified Stern-Volmer equation (see Figure S1-3), supporting the idea that the quenching occurs

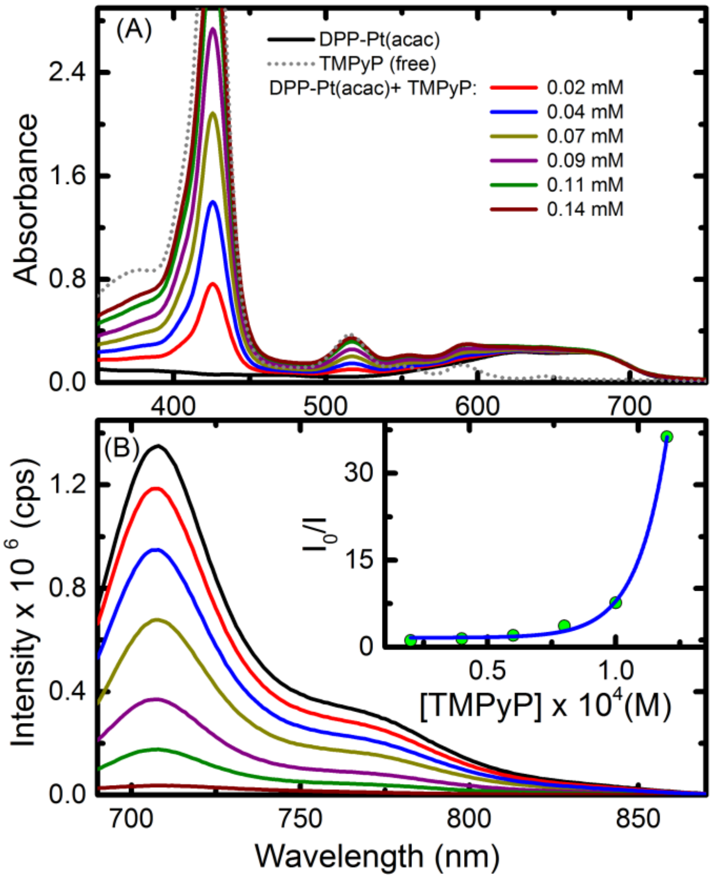

Figure 4.2 (A) Absorption and (B) fluorescence spectra of DPP-Pt(acac) using λ_{ex} = 660 nm in DCM:DMF (1:1) mixture with varying concentrations of TMPyP as indicated in the figure. Inset: Stern-Volmer plot. In the fluorescence quenching experiment, DPP-Pt(acac) is selectively excited at 660 nm, precluding any contribution from inner filter effects due to increased absorption by TMPyP.

predominantly via a static mechanism.[169] This quenching of DPP-Pt(acac) fluorescence upon the addition of TMPyP suggests that photoinduced CT occurs between DPP-Pt(acac) as the donor and TMPyP as acceptor. It is worth mentioning that Cl^- ion can quench the phosphorescence but not the short-lived fluorescence.[170] In addition, the concentration of Cl^- present as a counter-ion is extremely low. Knowing that the SV constant K_{SV} and bimolecular quenching K_q rate are described by the equation

$$K_{SV} = K_q \tau^0 \tag{4}$$

where K_q is the bimolecular quenching rate constant and τ^o is the fluorescence lifetime of DPP-Pt(acac) (130 ps), we compute $K_q \approx 1.6 \times 10^{14}$ M^{-1} s^{-1}. This quenching rate is well in excess of the diffusion controlled limit (estimated rate for TMPyP diffusion ~ 4.5×10^9 using the Stokes-Einstein equation in DMF under the current experimental conditions),[171] establishing the fact that the quenching is due to the formation of a ground state complex between the two chromophores.

To explore the influence of the porphyrin molecular structure and charge localization on the interaction with DPP-Pt(acac), we selected a closely related neutral porphyrin, TPyP. In this case, the absorption and fluorescence of DPP-Pt(acac) are unchanged upon TPyP addition, clearly indicating the absence of electronic interaction or CT complex formation between DPP-Pt(acac) and TPyP. This observation raises an important question regarding the impact of the molecular structure on the ground- and excited-state TMPyP/DPP-Pt(acac) interactions. First, it is very likely that the cationic charge on TMPyP is crucial for the ground-state complex formation with DPP-Pt(acac). However, it is interesting that mixing TMPyP with a solution of DPP oligomer also results in no change in either the steady-state absorption or the fluorescence spectra. This result indicates that the molecular structure and cationic charge on the porphyrin are not the only requirements for the interaction; the ortho-metallated Pt(acac) unit is also key for switching the interaction on/off. Based on these results, we suggest that the interaction involves a charge transfer interaction between TMPyP (acceptor) and DPP-Pt(acac) (donor) in which one of the ortho-metallated Pt(acac) units is directly involved. This ground-state complex formation brings the TMPyP and DPP-Pt(acac) units into close proximity, allowing ultrafast photoinduced CT to occur.

4.2.2. Femtosecond Transient Absorption Spectroscopy

Since fs-TA spectroscopy provides direct information regarding excited-state CT and charge-recombination (CR),[172-173] we utilized this method to probe the events that occur upon photoexcitation of the DPP-Pt(acac)/TMPyP complex. Figure 4.3 shows the TA spectra of DPP-Pt(acac) after 680 nm pulse excitation without and with TMPyP (c = 0.05 and 0.4 mM). First, Figure 4.3A shows the transient absorption spectra of DPP-Pt(acac) in the absence of porphyrin following 680 nm excitation. As can be clearly seen, in addition to the strong bleaching over the range 550-700 nm due to ground state depletion (GSB), a broad excited-state absorption extending over the range 670-820 nm grows in over a 400 ps timescale. The rising absorption feature is attributed to the DPP-Pt(acac) triplet state. The growth of the triplet follows a single exponential with τ = 130 ps. This relatively rapid rate of intersystem crossing is attributed to the influence of the cyclometallated Pt(acac) units, which enhance spin-orbit coupling.[131, 163-164] Second, as shown in Figures 4.3(B and C), the addition of TMPyP to the DPP-Pt(acac) solution resulted in the formation of a new absorption feature with a peak at 760 nm and a shoulder at 715 nm. The rise-time of this new band is approximately 1.5 ps, considerably faster than the intersystem crossing of DPP-Pt(acac) in the absence of porphyrin. This new spectral feature was more clearly resolved as the TMPyP concentration increased from 5 x 10^{-5} M to 4 x 10^{-4} M. Based on the literature, the band at 760 nm can be attributed to the reduced form of TMPyP (which is technically a radical trication).[174-176]

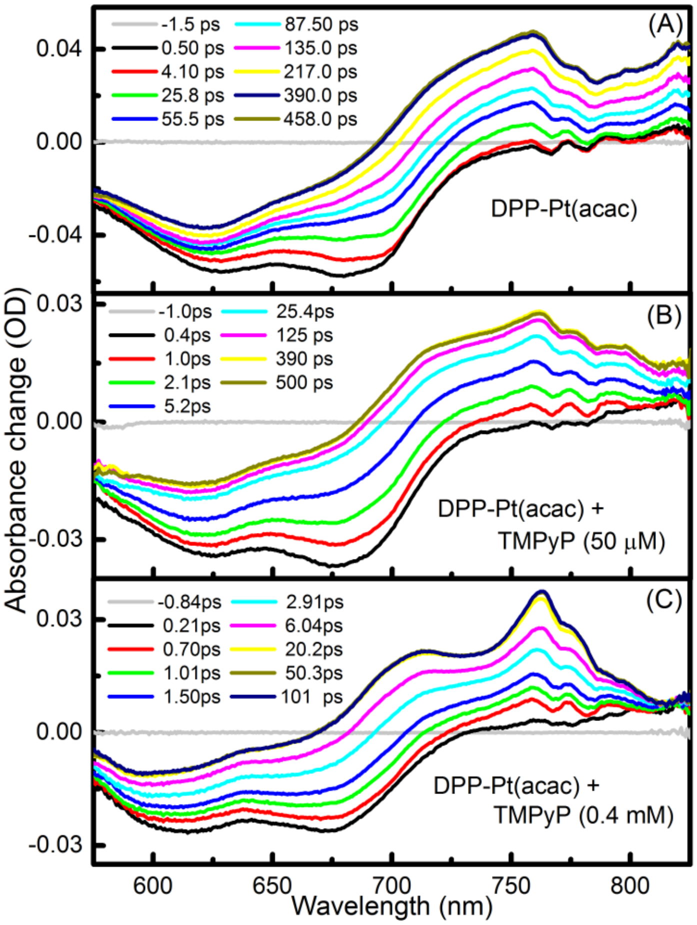

Figure 4.3 Transient absorption spectra after 680 nm pulse excitation collected in DCM:DMF mixtures at different delay times (indicated on the graph) of (A) DPP-Pt(acac), (B) DPP-Pt(acac) + TMPyP [50 μM] and (C) DPP-Pt(acac) + TMPyP [0.4 mM]. Note the different spread of probe delay times used in A, B and C (decreasing A to C).

To confirm the suggested DPP-Pt(acac) to TMPyP electron transfer, it is important to determine the absorption of the DPP-Pt(acac) radical cation. In control experiments, the DPP-Pt(acac) radical cation was produced by pump-probe experiments using two different common electron acceptors, i.e., tetracyanoethylene (TCNE), as we discussed in chapter 3, and [6,6]-phenyl-C61-butyric acid methyl ester (PCBM).[177-181] The resulting transient difference-absorption spectra are displayed in Figures SB(4 and 5), revealing a featureless band over the range 700-800 nm with a well-resolved shoulder at 715 nm. Further support for the suggested CT arises from the formation of the ground-state bleach of TMPyP at 417 nm after DPP-Pt(acac) selective excitation (see Figure 4.4). Based on this finding, it is very likely that the shoulder at 715 nm in the DPP-Pt(acac)/TMPyP system is due to the radical cation of DPP-Pt(acac), supporting the premise for photoinduced CT. On the basis of the TMPyP reduction potential (-1.01 V)[182] and the oxidation potential and singlet excited state energy of DPP-Pt(acac) (+0.79 V and 1.82 eV, respectively, electrochemical potentials are in V vs Ag/Ag^+), we estimate that photoinduced DPP-Pt(acac) to TMPyP CT is weakly exoergic (further evidence for the CT process arises from the observation of the GSB of TMPyP at 417 nm after DPP-Pt(acac) selective excitation).

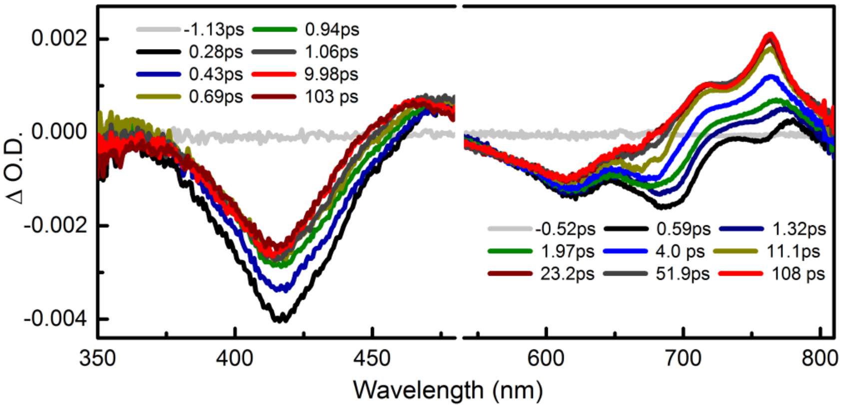

Figure 4.4 TA collected at different delay times (indicated on the graph) after 560 nm pulse excitation of DPP-Pt(acac) + TMPyP [0.1 mM] in (DMF) /(DCM) [1:1].

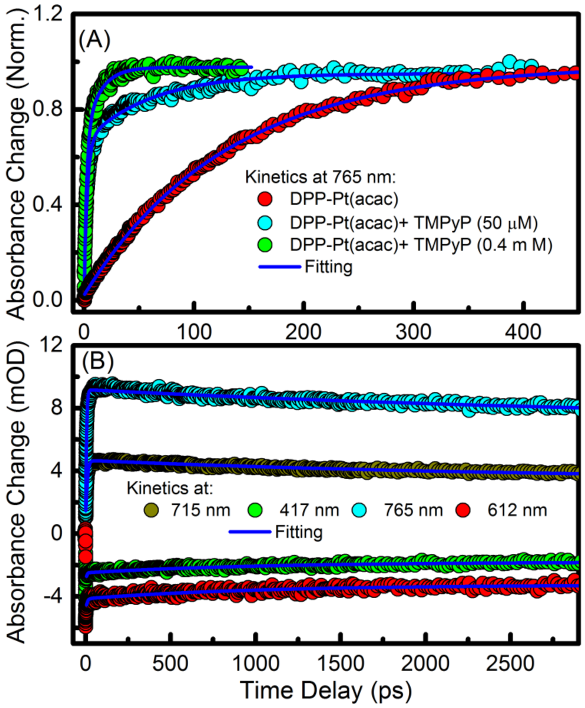

Figure 4.5 (A) Kinetic traces at 765 nm of DPP-Pt(acac) + TMPyP [0, 0.05, 0.4 mM] after 680 nm pulse excitation in DCM:DMF mixtures. (B) Kinetic traces at 417, 612, 715 and 765 nm of DPP-Pt(acac) + TMPyP [0.4 mM] after 560 nm pulse excitation in DCM:DMF.

4.2.3. Excited State Dynamics

To probe the dynamics of the DPP-Pt(acac) to TMPyP photoinduced CT, the TA kinetics were measured at specific wavelengths as a function of TMPyP concentration (Figure 4.5). Inspection of Figure 4.3 reveals that, by probing at 765 nm, it is possible to follow the rise of the triplet state (for DPP-Pt(acac) alone) or the CT state (for DPP-Pt(acac)/TMPyP). As shown in Figure 4.5A, with DPP-Pt(acac) alone, the rise follows a single exponential $\tau = 130$ ps. As noted above, this rise corresponds to the rate of $S_1 \rightarrow T_1$ intersystem crossing. By contrast, the rise kinetics at the same wavelength for the DPP-Pt(acac)/TMPyP complex are more than an order of magnitude faster than ISC, providing clear evidence for a strong electronic coupling between the chromophores giving rise to ultrafast CT. The CT rate in DPP-Pt(acac)/TMPyP is faster than observed in porphyrin-Pt(terpyridine) dyads[183] and comparable to that of a linked Pt-acetylide-PCBM assembly.[184] As shown in Figure 4.5B, the absorption of the CT state persists throughout the timescale accessible with our TA system (~ 3 ns), and GSB recovery reached a plateau (no further recovery), providing evidence for long-lived CS likely due to the dissociation of the contact radical ion pair into free ions. In this regard, the long-lived charge-separated state in this system is promising for organic solar applications.[185-187] As shown in Figure 4.5B, the cation and anion radical lifetimes are much longer than the maximum time window of our TA setup, and accurate time constants from these fits can be extracted or discussed.

4.2.4. The Effect of Molecular Structure on CT

The impact of the molecular structure on the oligomer/porphyrin CT interaction was examined by performing TA on DPP-Pt(acac) in the presence and absence of TPyP (neutral porphyrin), as shown in Figure 4.6, as well as on DPP with TMPyP; the spectra are given in Figure 4.7. In these cases, no changes are detected, and the kinetic traces in the two solutions are identical, providing a clear indication of the absence of photoinduced CT in either the DPP-Pt(acac)/TPyP or DPP/TMPyP systems. This result is consistent with the conclusion derived from the study of the ground-state absorption and fluorescence spectra. Interestingly, the TA results show that the CT process is switched off when DPP-Pt(acac) is replaced by DPP or when TMPyP is replaced by TPyP. This result is important because it indicates that both the positive charge on the porphyrin and the orthometallated Pt units in the oligomer are needed for CT complex formation. While the exact nature of the interaction is unknown, it is likely that the CT complex between TMPyP and DPP-Pt(acac) involves the square-planar Pt(II) units in the oligomer.

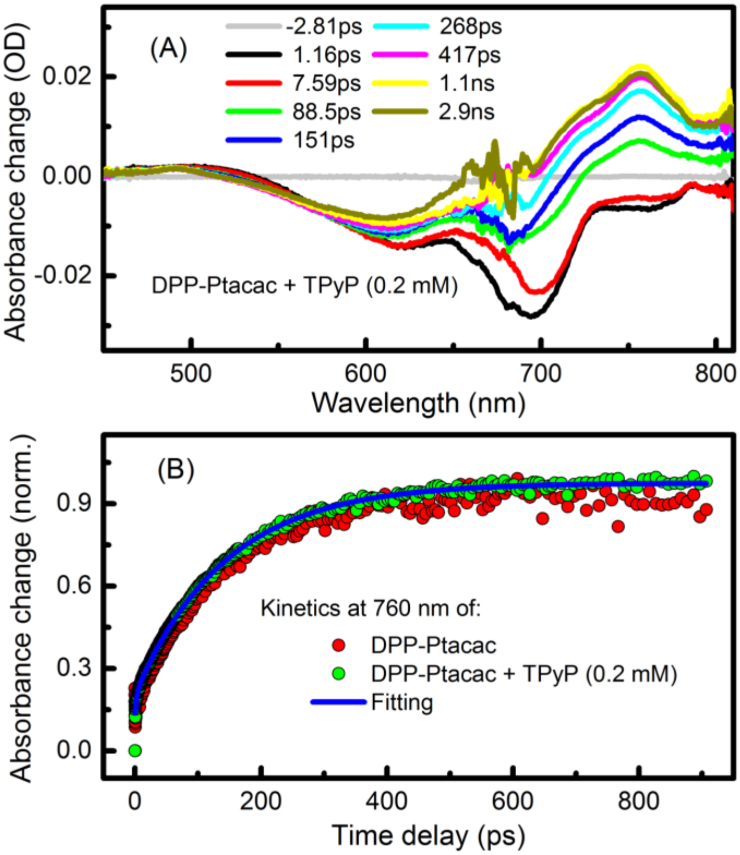

Figure 4.6 (A) Transient Absorption of DPP-Pt(acac) + TPyP [0.2 mM] after 680 nm pulse excitation and (B) kinetic traces collected at 760 nm in dichloromethane (DCM).

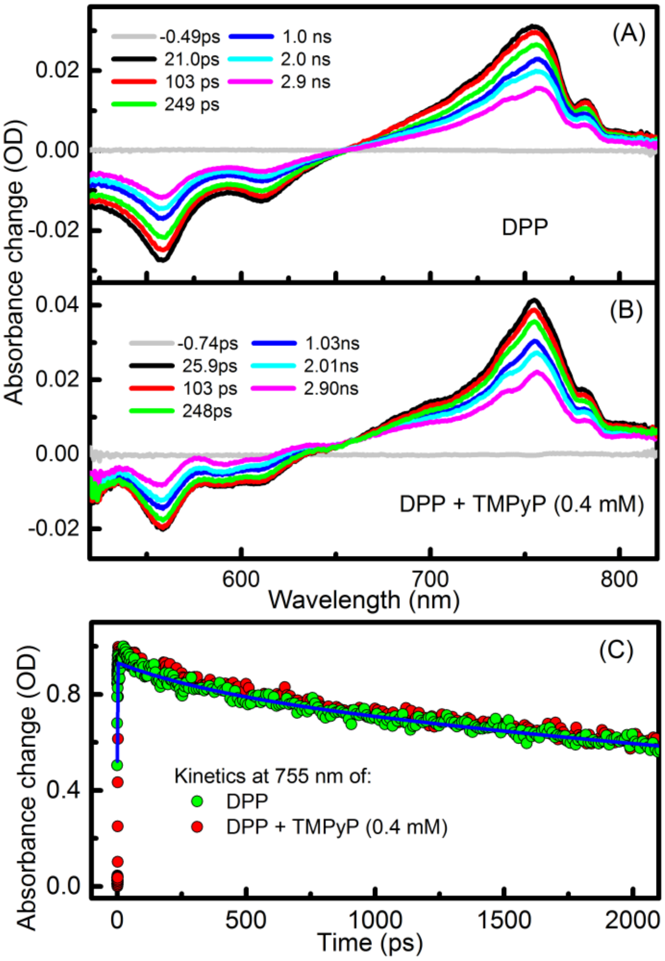

Figure 4.7 Averaged transient absorption spectra of DPP at the indicated delay time windows after 480 nm pulse excitation (A) without and (B) with TMPyP [0.4 mM] in DCM:DMF mixtures. (C) Kinetic traces at 755 nm of DPP with (green) and without TMPyP (red); the solid blue line is the calculated fit.

4.3. Conclusion

We report for the first time the ultrafast on/off charge transfer between a new platinum-containing oligomer as the electron donor and different porphyrin structures as the electron acceptors. We found that both the metallic center in the DPP-Pt(acac) oligomer and the positive charge on the porphyrin are required to switch on the reaction. In addition, turning the CT on/off can also be achieved by replacing DPP-Pt(acac) with structurally similar organic oligomers with no metal centers regardless of the structure of the porphyrins. This finding provides additional support indicating that the metal center and the positive charge of the porphyrin are the keys to turning the process on/off. Finally, the measured fast CT and slow CR make the current donor-acceptor system promising for potential applications in organic solar cells.

CHAPTER 5

SUMMARY AND OUTLOOK

In organic donor–acceptor systems, controlling charge transfer (CT), charge separation (CS), and charge recombination (CR) at interfaces is extremely important to optimize the power conversion efficiency in solar cell devices. In general, a profound understanding of these photophysical processes at device interfaces is extremely important, but they have been studied only superficially, creating a major bottleneck that circumvents advancements and the optimization of solar cells.

In chapter 2, we explored the significant impact of ultrafast CS and CR at D/A interfaces on device performance of a conjugated polymer PTB7-Th with three FAs: $PC_{71}BM$, $PC_{61}BM$ and $IC_{60}BA$. The results from time-resolved laser spectroscopy and high-resolution electron microscopy are examined to provide the fundamental information necessary to fabricate and optimize the performances of organic solar cell devices. CT and CS are monitored in real time at the interface between three fullerene acceptors (FAs: $PC_{71}BM$, $PC_{61}BM$, and $IC_{60}BA$) and PTB7-Th as the donor polymer. The femtosecond transient absorption (fs-TA) data demonstrate that photoinduced electron transfer from the PTB7-Th polymer to each FA occurs on the sub-picosecond time scale, leading to the formation of long-lived radical ions. The power conversion efficiency improves from 2% in $IC_{60}BA$-based solar cells to >9% in $PC_{71}BM$-based devices, in support of our time-resolved results (see Figure 5.1). The insights reported in this work provide a clear understanding of the key variables involved at the device interfaces, paving the way for the exploitation of efficient CS and subsequently improving the photoconversion efficiency.

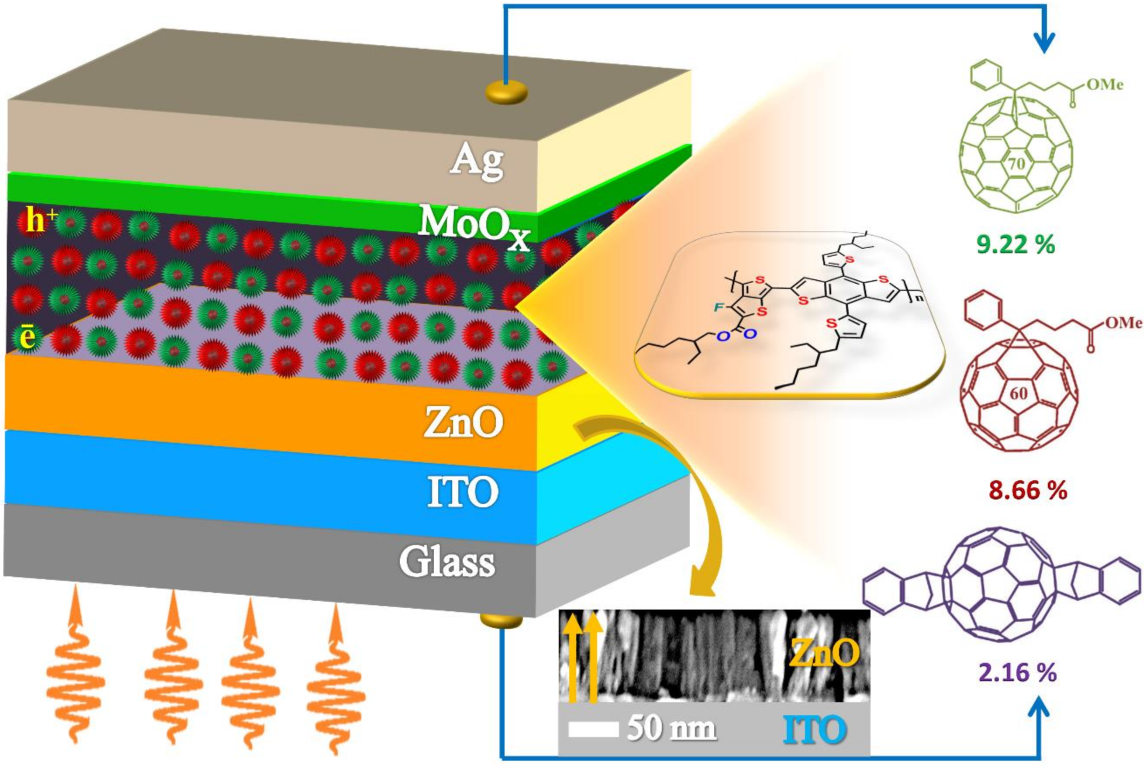

Figure 5.1 Schematic diagram of the device fabrication process for the D/FAs active layer.

In chapter 3, we continued our investigation of the bimolecular PET from the donor polymer to an electron acceptor in solution by focusing on tetracyanoethylene (TCNE) as the electron acceptor. Here, singlet-to-triplet intersystem crossing (ISC) and photoinduced electron transfer (PET) of platinum(II)-containing diketopyrrolopyrrole

(DPP) oligomers in the presence and absence of tetracyanoethylene (TCNE) were investigated using femtosecond and nanosecond transient absorption spectroscopies with broadband capabilities. The effect of incorporating platinum(II) on the photophysical properties of DPP molecule was evaluated by comparing the excited-state dynamics of DPP with and without Pt metal centers. The detailed study indicates that a Pt(II) center is essential to controlling the PET mechanism from the donor (DPP-Pt(acac) or DPP) to the TCNE electron acceptor (see Figure 5.2). Steady-state and time-resolved data demonstrate that the most influential role of the incorporated Pt(II) is to facilitate interactions between DPP-Pt(acac) with TCNE, resulting in the formation of a CT complex, which, in contrast, is absent in the DPP/TCNE system. The TA results show the possibility of switching the reaction mechanism from a diffusion-controlled process to a static process via incorporation of a Pt metal center into DPP.

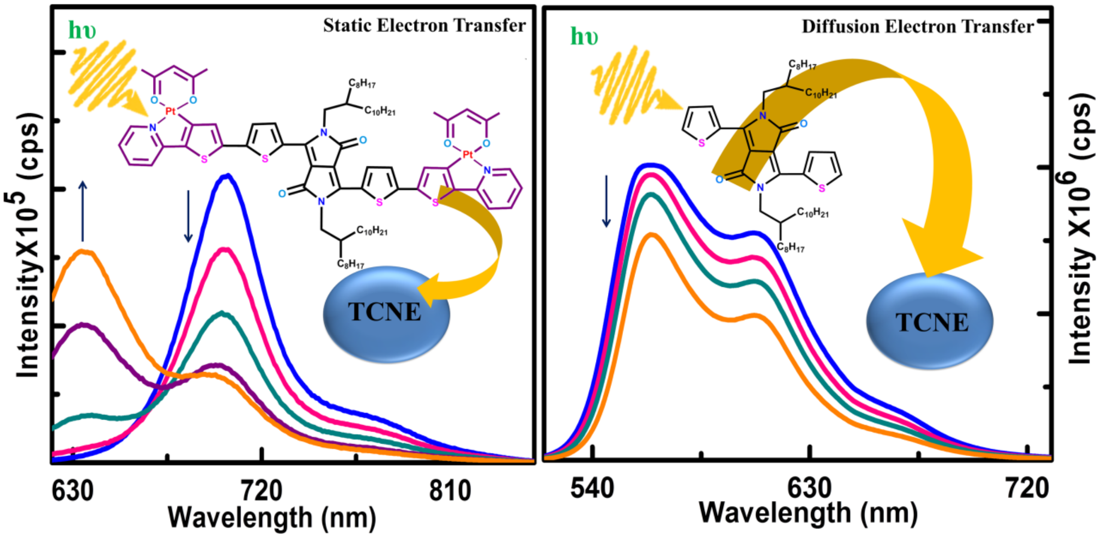

Figure 5.2 Schematic diagram showing the static and diffusion-controlled mechanisms of PET from the DPP-Pt(acac) and DPP oligomers to TCNE.

In chapter 4, the ultrafast excited-state CT between the platinum oligomer (DPP-Pt(acac)) as an electron donor and porphyrin as an electron acceptor was monitored for the first time using femtosecond (fs) transient absorption (TA) spectroscopy with broad-band capability and 120 fs temporal resolution. Turning the CT on/off has been shown to be possible either by switching from an organometallic oligomer to a metal-free oligomer or by controlling the charge density on the nitrogen atom of the porphyrin meso unit. Our time-resolved data show that the CT and CS between DPP-Pt(acac) and TMPyP are ultrafast (approximately 1.5 ps), and the CR is slow (ns time scale), as inferred from the formations and decays of the cationic and anionic species. The metallic center in the DPP-Pt(acac) oligomer and the positive charge on the porphyrin are the keys to switching on/off the ultrafast CT process. This finding provides additional support indicating that the metal center and the positive charge of the porphyrin are the keys to turning the process on/off as illustrated in Figure 5.3.

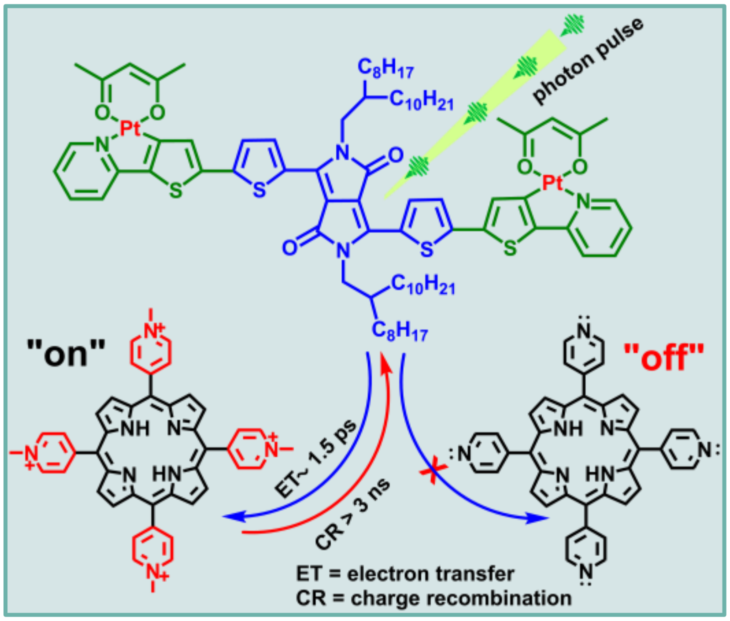

Figure 5.3 Scheme of on/off electron transfer from DPP-Pt(acac) to TMPyP and TPyP.

Outlook:

Photoinduced electron transfer is one of the most important chemical reactions in physical chemistry and solar cells communities. Therefore, the profound understanding of such dynamical processes in donor-acceptor systems will be helpful for ultimate optimization of solar-cell devices .We next hope to extend these experiments to different photoactive materials with a variety of different fullerene and non-fullerene-based acceptor materials to evaluate the effect of changes in the energy level alignments on charge transfer, charge recombination and subsequently the device performance. More specifically, the main goal is not only to provide essential information on the mechanistic and kinetic details of the charge transfer process, but also find a clear way to promote it at the D/A interfaces. In this case, we may provide key variable components to control the charge transfer dynamics and the transfer efficiency at such donor-acceptor systems.

REFERENCES

1. Noy, D.; Moser, C. C.; Dutton, P. L., Design and Engineering of Photosynthetic Light-Harvesting and Electron Transfer Using Length, Time, and Energy Scales. *Biochimica et Biophysica Acta (BBA) - Bioenergetics* **2006**, *1757*, 90-105.

2. Chan, W.-L.; Tritsch, J. R.; Zhu, X. Y., Harvesting Singlet Fission for Solar Energy Conversion: One- Versus Two-Electron Transfer from the Quantum Mechanical Superposition. *Journal of the American Chemical Society* **2012**, *134*, 18295-18302.

3. Krishnamurthy, S.; Kamat, P. V., Cdse–Graphene Oxide Light-Harvesting Assembly: Size-Dependent Electron Transfer and Light Energy Conversion Aspects. *ChemPhysChem* **2014**, *15*, 2129-2135.

4. Mattay, J., *Photoinduced Electron Transfer Iv*; Springer Verlag: Berlin, **1992**; Vol. 163.

5. Mazzio, K. A.; Luscombe, C. K., The Future of Organic Photovoltaics. *Chemical Society Reviews* **2015**, *44*, 78-90.

6. Marcus, R. A.; Sutin, N., Electron Transfers in Chemistry and Biology. *Biochimica et Biophysica Acta (BBA) - Reviews on Bioenergetics* **1985**, *811*, 265-322.

7. Choy, W. C. H., *Organic Solar Cells: Materials and Device Physics*; Springer London, **2012**.

8. Joran, A. D.; Leland, B. A.; Geller, G. G.; Hopfield, J. J.; Dervan, P. B., Models for Photochemical Electron Transfer at Fixed Distances. Porphyrin-Bicyclo[2.2.2]Octane-Quinone and Porphyrin-Bisbicyclo[2.2.2]Octane-Quinone. *Journal of the American Chemical Society* **1984**, *106*, 6090-6092.

9. Creager, S. et al., Electron Transfer at Electrodes through Conjugated “Molecular Wire” Bridges. *Journal of the American Chemical Society* **1999**, *121*, 1059-1064.

10. Clarke, T. M.; Durrant, J. R., Charge Photogeneration in Organic Solar Cells. *Chemical Reviews* **2010**, *110*, 6736-6767.

11. Jaffe, H. H.; Miller, A. L., The Fates of Electronic Excitation Energy. *Journal of Chemical Education* **1966**, *43*, 469.

12. Pawlizak, S. Fluorescence Microscopy University of Leipzig, **2009**.

13. Priestley, E. B.; Haug, A., Phosphorescence Spectrum of Pure Crystalline Naphthalene. *The Journal of Chemical Physics* **1968**, *49*, 622-629.

14. Frackowiak, D., The Jablonski Diagram. *Journal of Photochemistry and Photobiology B: Biology* **1988**, *2*, 399.

15. Kippelen, B.; Bredas, J.-L., Organic Photovoltaics. *Energy & Environmental Science* **2009**, *2*, 251-261.

16. Norrish, R. G. W.; Porter, G., Chemical Reactions Produced by Very High Light Intensities. *Nature* **1949**, *164*, 658-658.

17. Porter, G., Flash Photolysis and Spectroscopy a New Method for the Study of Free Radical Reactions. *Proceedings of the Royal Society of London Series a-Mathematical and Physical Sciences* **1950**, *200*, 284-308.

18. Norrish, R. G. W., Some Fast Reactions in Gases Studied by Flash Photolysis and Kinetic Spectroscopy. In *Spectroscopy of the Excited State*, Di Bartolo, B.; Pacheco, D.; Goldberg, V., Eds. Springer US: Boston, MA, **1976**, 117-160.

19. Zewail, A. H., Femtochemistry: Atomic-Scale Dynamics of the Chemical Bond Using Ultrafast Lasers - (Nobel Lecture). *Angewandte Chemie-International Edition* **2000**, *39*, 2587-2631.

20. Bastiaens, P. I.; Squire, A., Fluorescence Lifetime Imaging Microscopy: Spatial Resolution of Biochemical Processes in the Cell. *Trends in cell biology* **1999**, *9*, 48-52.

21. Selinsky, R. S.; Ding, Q.; Faber, M. S.; Wright, J. C.; Jin, S., Quantum Dot Nanoscale Heterostructures for Solar Energy Conversion. *Chemical Society Reviews* **2013**, *42*, 2963-2985.

22. Aly, S. M.; Goswami, S.; Alsulami, Q. A.; Schanze, K. S.; Mohammed, O. F., Ultrafast Photoinduced Electron Transfer in a Π-Conjugated Oligomer/Porphyrin Complex. *The Journal of Physical Chemistry Letters* **2014**, *5*, 3386-3390.

23. Mohammed, O. F.; Xiao, D.; Batista, V. S.; Nibbering, E. T. J., Excited-State Intramolecular Hydrogen Transfer (Esiht) of 1,8-Dihydroxy-9,10-Anthraquinone (Dhaq) Characterized by Ultrafast Electronic and Vibrational Spectroscopy and Computational Modeling. *Journal of Physical Chemistry A* **2014**, *118*, 3090-3099.

24. Berera, R.; van Grondelle, R.; Kennis, J. T. M., Ultrafast Transient Absorption Spectroscopy: Principles and Application to Photosynthetic Systems. *Photosynthesis Research* **2009**, *101*, 105-118.

25. Alsulami, Q. A.; Aly, S. M.; Goswami, S.; Alarousu, E.; Usman, A.; Schanze, K. S.; Mohammed, O. F., Ultrafast Excited-State Dynamics of Diketopyrrolopyrrole (Dpp)-Based Materials: Static Versus Diffusion-Controlled Electron Transfer Process. *The Journal of Physical Chemistry C* **2015**, *119*, 15919-15925.

26. Ohkita, H.; Tamai, Y.; Benten, H.; Ito, S., Transient Absorption Spectroscopy for Polymer Solar Cells. *Ieee Journal of Selected Topics in Quantum Electronics* **2016**, *22, 100-111.*

27. Sinclair, V. C.; Robertson, J. M.; McL Mathieson, A., The Crystal and Molecular Structure of Anthracene. Ii. Structure Investigation by the Triple Fourier Series Method. *Acta Crystallographica* **1950**, *3*, 251-256.

28. Cozzens, R. F., Electrical Properties of Polymer. D.A. Seanor, E., Ed. Academic Press New York, 1982; p 93.

29. Spanggaard, H.; Krebs, F. C., A Brief History of the Development of Organic and Polymeric Photovoltaics. *Solar Energy Materials and Solar Cells* **2004**, *83*, 125-146.

30. Li, G.; Zhu, R.; Yang, Y., Polymer Solar Cells. *Nature Photonics* **2012**, *6*, 153-161.

31. Krebs, F. C.; Espinosa, N.; Hösel, M.; Søndergaard, R. R.; Jørgensen, M., 25th Anniversary Article: Rise to Power – Opv-Based Solar Parks. *Advanced Materials* **2014**, *26*, 29-39.

32. Lee, C.; Kang, H.; Lee, W.; Kim, T.; Kim, K.-H.; Woo, H. Y.; Wang, C.; Kim, B. J., High-Performance All-Polymer Solar Cells Via Side-Chain Engineering of the Polymer Acceptor: The Importance of the Polymer Packing Structure and the Nanoscale Blend Morphology. *Advanced Materials* **2015**, *27*, 2466-2471.

33. He, Z.; Zhong, C.; Su, S.; Xu, M.; Wu, H.; Cao, Y., Enhanced Power-Conversion Efficiency in Polymer Solar Cells Using an Inverted Device Structure. Nature Photonics **2012**, 6, 591-595.

34. Sun, Y.; Welch, G. C.; Leong, W. L.; Takacs, C. J.; Bazan, G. C.; Heeger, A. J., Solution-Processed Small-Molecule Solar Cells with 6.7% Efficiency. *Nature materials* **2012**, *11*, 44-48.

35. You, J.; Dou, L.; Yoshimura, K.; Kato, T.; Ohya, K.; Moriarty, T.; Emery, K.; Chen, C.-C.; Gao, J.; Li, G., A Polymer Tandem Solar Cell with 10.6% Power Conversion Efficiency. *Nature communications* **2013**, *4*, 1446.

36. Zhan, X.; Tan, Z. a.; Domercq, B.; An, Z.; Zhang, X.; Barlow, S.; Li, Y.; Zhu, D.; Kippelen, B.; Marder, S. R., A High-Mobility Electron-Transport Polymer with Broad Absorption and Its Use in Field-Effect Transistors and All-Polymer Solar Cells. *Journal of the American Chemical Society* **2007**, *129*, 7246-7247.

37. Chun-Chao, C.; Wei-Hsuan, C.; Yoshimura, K.; Ohya, K.; Jingbi, Y.; Jing, G.; Zirou, H.; Yang, Y., An Efficient Triple-Junction Polymer Solar Cell Having a Power Conversion Efficiency Exceeding 11%. *Advanced Materials* **2014**, *26*, 5670-5677.

38. Jo, J. W.; Jung, J. W.; Wang, H.-W.; Kim, P.; Russell, T. P.; Jo, W. H., Fluorination of Polythiophene Derivatives for High Performance Organic Photovoltaics. *Chemistry of Materials* **2014**, *26*, 4214-4220.

39. Liu, Y.; Liu, F.; Wang, H.-W.; Nordlund, D.; Sun, Z.; Ferdous, S.; Russell, T. P., Sequential Deposition: Optimization of Solvent Swelling for High-Performance Polymer Solar Cells. *ACS Applied Materials & Interfaces* **2015**, *7*, 653-661.

40. Liu, Y.; Page, Z. A.; Russell, T. P.; Emrick, T., Finely Tuned Polymer Interlayers Enhance Solar Cell Efficiency. *Angewandte Chemie-International Edition* **2015**, *54*, 11485-11489.

41. Page, Z. A.; Liu, Y.; Duzhko, V. V.; Russell, T. P.; Emrick, T., Fulleropyrrolidine Interlayers: Tailoring Electrodes to Raise Organic Solar Cell Efficiency. *Science* **2014**, *346*, 441-444.

42. Wang, Q.; Xie, Y.; Soltani-Kordshuli, F.; Eslamian, M., Progress in Emerging Solution-Processed Thin Film Solar Cells – Part I: Polymer Solar Cells. *Renewable and Sustainable Energy Reviews* **2016**, *56*, 347-361.

43. Jung, J. W.; Jo, J. W.; Jung, E. H.; Jo, W. H., Recent Progress in High Efficiency Polymer Solar Cells by Rational Design and Energy Level Tuning of Low Bandgap Copolymers with Various Electron-Withdrawing Units. *Organic Electronics* **2016**, *31*, 149-170.

44. Cheng, Y.-J.; Yang, S.-H.; Hsu, C.-S., Synthesis of Conjugated Polymers for Organic Solar Cell Applications. *Chemical Reviews* **2009**, *109*, 5868-5923.

45. Chen, J.; Cao, Y., Development of Novel Conjugated Donor Polymers for High-Efficiency Bulk-Heterojunction Photovoltaic Devices. *Accounts of Chemical Research* **2009**, *42*, 1709-1718.

46. Sariciftci, N. S.; Heeger, A. J., Conjugated Polymer - Acceptor Heterojunctions; Diodes, Photodiodes, and Photovoltaic Cells. Google Patents: **1994**.

47. Campoy-Quiles, M.; Ferenczi, T.; Agostinelli, T.; Etchegoin, P. G.; Kim, Y.; Anthopoulos, T. D.; Stavrinou, P. N.; Bradley, D. D. C.; Nelson, J., Morphology Evolution Via Self-Organization and Lateral and Vertical Diffusion in Polymer:Fullerene Solar Cell Blends. *Nature Materials* **2008**, *7*, 158-164.

48. Perumal, A.; Faber, H.; Yaacobi-Gross, N.; Pattanasattayavong, P.; Burgess, C.; Jha, S.; McLachlan, M. A.; Stavrinou, P. N.; Anthopoulos, T. D.; Bradley, D. D. C., High-Efficiency, Solution-Processed, Multilayer Phosphorescent Organic Light-Emitting Diodes with a Copper Thiocyanate Hole-Injection/Hole-Transport Layer. *Advanced Materials* **2015**, *27*, 93-100.

49. Hagfeldt, A.; Boschloo, G.; Sun, L. C.; Kloo, L.; Pettersson, H., Dye-Sensitized Solar Cells. *Chemical Reviews* **2010**, *110*, 6595-6663.

50. Jennings, J. R.; Liu, Y.; Wang, Q.; Zakeeruddin, S. M.; Gratzel, M., The Influence of Dye Structure on Charge Recombination in Dye-Sensitized Solar Cells. *Physical Chemistry Chemical Physics* **2011**, *13*, 6637-6648.

51. Maggio, E.; Martsinovich, N.; Troisi, A., Evaluating Charge Recombination Rate in Dye-Sensitized Solar Cells from Electronic Structure Calculations. *Journal of Physical Chemistry C* **2012**, *116*, 7638-7649.

52. Guo, Z.; Manser, J. S.; Wan, Y.; Kamat, P. V.; Huang, L., Spatial and Temporal Imaging of Long-Range Charge Transport in Perovskite Thin Films by Ultrafast Microscopy. *Nature Communications* **2015**, *6, 7471*.

53. Granstrom, M.; Petritsch, K.; Arias, A. C.; Lux, A.; Andersson, M. R.; Friend, R. H., Laminated Fabrication of Polymeric Photovoltaic Diodes. *Nature* **1998**, *395*, 257-260.

54. Koetse, M. M.; Sweelssen, J.; Hoekerd, K. T.; Schoo, H. F. M.; Veenstra, S. C.; Kroon, J. M.; Yang, X. N.; Loos, J., Efficient Polymer: Polymer Bulk Heterojunction Solar Cells. *Applied Physics Letters* **2006**, *88*.

55. Zou, Y. P.; Hou, J. H.; Yang, C. H.; Li, Y. F., A Novel N-Type Conjugated Polymer Docn-Ppv: Synthesis, Optical, and Electrochemical Properties. *Macromolecules* **2006**, *39*, 8889-8891.

56. Tan, Z. A.; Zhou, E. J.; Zhan, X. W.; Wang, X.; Li, Y. F.; Barlow, S.; Marder, S. R., Efficient All-Polymer Solar Cells Based on Blend of Tris(Thienylenevinylene)-Substituted Polythiophene and Poly Perylene Diimide-Alt-Bis(Dithienothiophene). *Applied Physics Letters* **2008**, *93, 073309*.

57. Zhan, X. W. et al., Copolymers of Perylene Diimide with Dithienothiophene and Dithienopyrrole as Electron-Transport Materials for All-Polymer Solar Cells and Field-Effect Transistors. *Journal of Materials Chemistry* **2009**, *19*, 5794-5803.

58. Liang, P. W.; Chueh, C. C.; Williams, S. T.; Jen, A. K. Y., Roles of Fullerene-Based Interlayers in Enhancing the Performance of Organometal Perovskite Thin-Film Solar Cells. *Advanced Energy Materials* **2015**, *5,1402321*.

59. You, J. et al., Low-Temperature Solution-Processed Perovskite Solar Cells with High Efficiency and Flexibility. *ACS Nano* **2014**, *8*, 1674-1680.

60. Qi, W.; Yuchuan, S.; Qingfeng, D.; Zhengguo, X.; Yongbo, Y.; Jinsong, H., Large Fill-Factor Bilayer Iodine Perovskite Solar Cells Fabricated by a Low-Temperature Solution-Process. *Energy & Environmental Science* **2014**, *7*, 2359-65.

61. Liang, Y. Y.; Xu, Z.; Xia, J. B.; Tsai, S. T.; Wu, Y.; Li, G.; Ray, C.; Yu, L. P., For the Bright Future-Bulk Heterojunction Polymer Solar Cells with Power Conversion Efficiency of 7.4%. *Advanced Materials* **2010**, *22*, 135-138.

62. Guo, X.; Zhang, M. J.; Ma, W.; Ye, L.; Zhang, S. Q.; Liu, S. J.; Ade, H.; Huang, F.; Hou, J. H., Enhanced Photovoltaic Performance by Modulating Surface Composition in Bulk Heterojunction Polymer Solar Cells Based on Pbdttt-C-T/Pc71bm. *Advanced Materials* **2014**, *26*, 4043-4049.

63. Chen, H. Y.; Hou, J. H.; Zhang, S. Q.; Liang, Y. Y.; Yang, G. W.; Yang, Y.; Yu, L. P.; Wu, Y.; Li, G., Polymer Solar Cells with Enhanced Open-Circuit Voltage and Efficiency. *Nature Photonics* **2009**, *3*, 649-653.

64. Cabanetos, C.; El Labban, A.; Bartelt, J. A.; Douglas, J. D.; Mateker, W. R.; Fréchet, J. M. J.; McGehee, M. D.; Beaujuge, P. M., Linear Side Chains in Benzo[1,2-B:4,5-B′]Dithiophene–Thieno[3,4-C]Pyrrole-4,6-Dione Polymers Direct Self-Assembly and Solar Cell Performance. *Journal of the American Chemical Society* **2013**, *135*, 4656-4659.

65. Huo, L.; Hou, J., Benzo[1,2-B:4,5-B[Prime or Minute]]Dithiophene-Based Conjugated Polymers: Band Gap and Energy Level Control and Their Application in Polymer Solar Cells. *Polymer Chemistry* **2011**, *2*, 2453-2461.

66. Tan, Z. a.; Li, L.; Wang, F.; Xu, Q.; Li, S.; Sun, G.; Tu, X.; Hou, X.; Hou, J.; Li, Y., Solution-Processed Rhenium Oxide: A Versatile Anode Buffer Layer for High Performance Polymer Solar Cells with Enhanced Light Harvest. *Advanced Energy Materials* **2014**, *4,1*-7.

67. Kong, J.; Hwang, I. W.; Lee, K., Top-Down Approach for Nanophase Reconstruction in Bulk Heterojunction Solar Cells. *Advanced Materials* **2014**, *26*, 6275-6283.

68. Huang, W.; Gann, E.; Thomsen, L.; Dong, C.; Cheng, Y.-B.; McNeill, C. R., Unraveling the Morphology of High Efficiency Polymer Solar Cells Based on the Donor Polymer PBDTTT-EFT. *Advanced Energy Materials* **2015**, *5*, 1401259, DOI: 10.1002/aenm.201401259.

69. Zhang, S. Q.; Ye, L.; Zhao, W. C.; Liu, D. L.; Yao, H. F.; Hou, J. H., Side Chain Selection for Designing Highly Efficient Photovoltaic Polymers with 2d-Conjugated Structure. *Macromolecules* **2014**, *47*, 4653-4659.

70. Ren, G. Q.; Schlenker, C. W.; Ahmed, E.; Subramaniyan, S.; Olthof, S.; Kahn, A.; Ginger, D. S.; Jenekhe, S. A., Photoinduced Hole Transfer Becomes Suppressed with Diminished Driving Force in Polymer-Fullerene Solar Cells While Electron Transfer Remains Active. *Advanced Functional Materials* **2013**, *23*, 1238-1249.

71. Kavarnos, G. J.; Turro, N. J., Photosensitization by Reversible Electron-Transfer - Theories, Experimental-Evidence, and Examples. *Chemical Reviews* **1986**, *86*, 401-449.

72. Birks, J. B., *Photophysics of Aromatic Molecules*; Wiley-Interscience: London; New York, **1970**.

73. Nagasawa, Y.; Yartsev, A. P.; Tominaga, K.; Bisht, P. B.; Johnson, A. E.; Yoshihara, K., Dynamic Aspects of Ultrafast Intermolecular Electron Transfer Faster Than Solvation Process: Substituent Effects and Energy Gap Dependence. *The Journal of Physical Chemistry* **1995**, *99*, 653-662.

74. Nad, S.; Pal, H., Electron Transfer from Aromatic Amines to Excited Coumarin Dyes: Fluorescence Quenching and Picosecond Transient Absorption Studies. *The Journal of Physical Chemistry A* **2000**, *104*, 673-680.

75. Castner, E. W.; Kennedy, D.; Cave, R. J., Solvent as Electron Donor: Donor/Acceptor Electronic Coupling Is a Dynamical Variable. *The Journal of Physical Chemistry A* **2000**, *104*, 2869-2885.

76. Pal, H.; Nagasawa, Y.; Tominaga, K.; Yoshihara, K., Deuterium Isotope Effect on Ultrafast Intermolecular Electron Transfer. *The Journal of Physical Chemistry* **1996**, *100*, 11964-11974.

77. Albrecht, C., Joseph R. Lakowicz: Principles of Fluorescence Spectroscopy, 3rd Edition. *Anal Bioanal Chem* **2008**, *390*, 1223-1224.

78. Wan, Y.; Guo, Z.; Zhu, T.; Yan, S.; Johnson, J.; Huang, L., Cooperative Singlet and Triplet Exciton Transport in Tetracene Crystals Visualized by Ultrafast Microscopy. *Nature Chemistry* **2015**, *7*, 785-792.

79. Debnath, T.; Maity, P.; Banerjee, T.; Das, A.; Ghosh, H. N., Ultrafast Electron Injection, Hole Transfer, and Charge Recombination Dynamics in Cdse Qd Super-Sensitized Re(I)–Polypyridyl Complexes with Catechol and Resorcinol Moiety: Effect of Coupling. *The Journal of Physical Chemistry C* **2015**, *119*, 3522-3529.

80. Maity, P.; Debnath, T.; Chopra, U.; Ghosh, H. N., Cascading Electron and Hole Transfer Dynamics in a Cds/Cdte Core-Shell Sensitized with Bromo-Pyrogallol Red (Br-Pgr): Slow Charge Recombination in Type II Regime. *Nanoscale* **2015**, *7*, 2698-2707.

81. Aly, S. M.; Parida, M. R.; Alarousu, E.; Mohammed, O. F., Ultrafast Electron Injection at the Cationic Porphyrin-Graphene Interface Assisted by Molecular Flattening. *Chemical Communications* **2014**, *50*, 10452-10455.

82. Sperlich, A.; Liedtke, M.; Kern, J.; Kraus, H.; Deibel, C.; Filippone, S.; Luis Delgado, J.; Martin, N.; Dyakonov, V., Photoinduced C-70 Radical Anions in Polymer: Fullerene Blends. *Physica Status Solidi-Rapid Research Letters* **2011**, *5*, 128-130.

83. Guldi, D. M.; Prato, M., Excited-State Properties of C-60 Fullerene Derivatives. *Accounts of Chemical Research* **2000**, *33*, 695-703.

84. Koster, L. J. A.; Mihailetchi, V. D.; Blom, P. W. M., Ultimate Efficiency of Polymer/Fullerene Bulk Heterojunction Solar Cells. *Applied Physics Letters* **2006**, *88*, 093511.

85. Murali, B.; Labban, A. E.; Eid, J.; Alarousu, E.; Shi, D.; Zhang, Q.; Zhang, X.; Bakr, O. M.; Mohammed, O. F., The Impact of Grain Alignment of the Electron Transporting Layer on the Performance of Inverted Bulk Heterojunction Solar Cells. *Small* **2015**, *11*, 5272-5279.

86. Karg, S.; Riess, W.; Dyakonov, V.; Schwoerer, M., Electrical and Optical Characterization of Poly(Phenylene-Vinylene) Light Emitting Diodes. *Synthetic Metals* **1993**, *54*, 427-433.

87. Tang, C. W., Multilayer Organic Photovoltaic Elements. Google Patents: **1981**.

88. Halls, J. J. M.; Pichler, K.; Friend, R. H.; Moratti, S. C.; Holmes, A. B., Exciton Diffusion and Dissociation in a Poly(P-Phenylenevinylene)/C60 Heterojunction Photovoltaic Cell. *Applied Physics Letters* **1996**, *68*, 3120-3122.

89. Yu, G.; Gao, J.; Hummelen, J. C.; Wudl, F.; Heeger, A. J., Polymer Photovoltaic Cells - Enhanced Efficiencies Via a Network of Internal Donor-Acceptor Heterojunctions. *Science* **1995**, *270*, 1789-1791.

90. Park, S. H.; Roy, A.; Beaupre, S.; Cho, S.; Coates, N.; Moon, J. S.; Moses, D.; Leclerc, M.; Lee, K.; Heeger, A. J., Bulk Heterojunction Solar Cells with Internal Quantum Efficiency Approaching 100%. *Nature Photonics* **2009**, *3*, 297-302.

91. Scharber, M. C.; Mühlbacher, D.; Koppe, M.; Denk, P.; Waldauf, C.; Heeger, A. J.; Brabec, C. J., Design Rules for Donors in Bulk-Heterojunction Solar Cells—Towards 10% Energy-Conversion Efficiency. *Advanced materials* **2006**, *18*, 789-794.

92. Wang, H.-J.; Chen, C.-P.; Jeng, R.-J., Polythiophenes Comprising Conjugated Pendants for Polymer Solar Cells: A Review. *Materials* **2014**, *7*, 2411-2439.

93. Ye, L.; Jiang, W.; Zhao, W.; Zhang, S.; Cui, Y.; Wang, Z.; Hou, J., Toward Efficient Non-Fullerene Polymer Solar Cells: Selection of Donor Polymers. *Organic Electronics* **2015**, *17*, 295-303.

94. Chen, C.-C.; Chang, W.-H.; Yoshimura, K.; Ohya, K.; You, J.; Gao, J.; Hong, Z.; Yang, Y., An Efficient Triple-Junction Polymer Solar Cell Having a Power Conversion Efficiency Exceeding 11%. *Advanced Materials* **2014**, *26*, 5670-5677.

95. Dou, L.; You, J.; Hong, Z.; Xu, Z.; Li, G.; Street, R. A.; Yang, Y., 25th Anniversary Article: A Decade of Organic/Polymeric Photovoltaic Research. *Advanced Materials* **2013**, *25*, 6642-6671.

96. Chen, J.-D.; Cui, C.; Li, Y.-Q.; Zhou, L.; Ou, Q.-D.; Li, C.; Li, Y.; Tang, J.-X., Single-Junction Polymer Solar Cells Exceeding 10% Power Conversion Efficiency. *Advanced Materials* **2015**, *27*, 1035-1041.

97. Guo, X. et al., Bithiopheneimide–Dithienosilole/Dithienogermole Copolymers for Efficient Solar Cells: Information from Structure–Property–Device Performance Correlations and Comparison to Thieno[3,4-C]Pyrrole-4,6-Dione Analogues. *Journal of the American Chemical Society* **2012**, *134*, 18427-18439.

98. Farnum, D. G.; Mehta, G.; Moore, G. G. I.; Siegal, F. P., Attempted Reformatskii Reaction of Benzonitrile, 1,4-Diketo-3,6-Diphenylpyrrolo[3,4-C]Pyrrole. A Lactam Analogue of Pentalene. *Tetrahedron Letters* **1974**, *15*, 2549-2552.

99. Naik, M. A.; Patil, S., Diketopyrrolopyrrole-Based Conjugated Polymers and Small Molecules for Organic Ambipolar Transistors and Solar Cells. *Journal of Polymer Science Part A: Polymer Chemistry* **2013**, *51*, 4241-4260.

100. Chandran, D.; Lee, K.-S., Diketopyrrolopyrrole: A Versatile Building Block for Organic Photovoltaic Materials. *Macromolecular Research* **2013**, *21*, 272-283.

101. Wu, Y.; Zhu, W., Organic Sensitizers from D-[Small Pi]-a to D-a-[Small Pi]-A: Effect of the Internal Electron-Withdrawing Units on Molecular Absorption, Energy Levels and Photovoltaic Performances. *Chemical Society Reviews* **2013**, *42*, 2039-2058.

102. Qu, S.; Tian, H., Diketopyrrolopyrrole (DPP)-Based Materials for Organic Photovoltaics. *Chemical Communications* **2012**, *48*, 3039-3051.

103. Kanimozhi, C.; Yaacobi-Gross, N.; Chou, K. W.; Amassian, A.; Anthopoulos, T. D.; Patil, S., Diketopyrrolopyrrole–Diketopyrrolopyrrole-Based Conjugated Copolymer for High-Mobility Organic Field-Effect Transistors. *Journal of the American Chemical Society* **2012**, *134*, 16532-16535.

104. Dhar, J.; Venkatramaiah, N.; Anitha, A.; Patil, S., Photophysical, Electrochemical and Solid State Properties of Diketopyrrolopyrrole Based Molecular Materials: Importance of the Donor Group. *Journal of Materials Chemistry C* **2014**, *2*, 3457-3466.

105. McCusker, C. E.; Hablot, D.; Ziessel, R.; Castellano, F. N., Metal Coordination Induced Π-Extension and Triplet State Production in Diketopyrrolopyrrole Chromophores. *Inorganic chemistry* **2012**, *51*, 7957-7959.

106. Glusac, K.; Köse, M. E.; Jiang, H.; Schanze, K. S., Triplet Excited State in Platinum-Acetylide Oligomers: Triplet Localization and Effects of Conformation. *The Journal of Physical Chemistry B* **2007**, *111*, 929-940.

107. Liao, C.; Shelton, A. H.; Kim, K.-Y.; Schanze, K. S., Organoplatinum Chromophores for Application in High-Performance Nonlinear Absorption Materials. *ACS applied materials & interfaces* **2011**, *3*, 3225-3238.

108. Williams, J. G.; Develay, S.; Rochester, D. L.; Murphy, L., Optimising the Luminescence of Platinum (II) Complexes and Their Application in Organic Light Emitting Devices (Oleds). *Coordination Chemistry Reviews* **2008**, *252*, 2596-2611.

109. Baldo, M. A.; O'Brien, D. F.; You, Y.; Shoustikov, A.; Sibley, S.; Thompson, M. E.; Forrest, S. R., Highly Efficient Phosphorescent Emission from Organic Electroluminescent Devices. *Nature* **1998**, *395*, 151-154.

110. Costa, R. D.; Orti, E.; Bolink, H. J.; Monti, F.; Accorsi, G.; Armaroli, N., Luminescent Ionic Transition-Metal Complexes for Light-Emitting Electrochemical Cells. *Angewandte Chemie International Edition* **2012**, *51*, 8178-8211.

111. Zhao, Q.; Huang, C.; Li, F., Phosphorescent Heavy-Metal Complexes for Bioimaging. *Chemical Society Reviews* **2011**, *40*, 2508-2524.

112. Ma, D.-L.; He, H.-Z.; Leung, K.-H.; Chan, D. S.-H.; Leung, C.-H., Bioactive Luminescent Transition-Metal Complexes for Biomedical Applications. *Angewandte Chemie International Edition* **2013**, *52*, 7666-7682.

113. Zhao, Q.; Li, F.; Huang, C., Phosphorescent Chemosensors Based on Heavy-Metal Complexes. *Chemical Society Reviews* **2010**, *39*, 3007-3030.

114. Liu, Z.; He, W.; Guo, Z., Metal Coordination in Photoluminescent Sensing. *Chemical Society Reviews* **2013**, *42*, 1568-1600.

115. Williams, J. A. G., Photochemistry and Photophysics of Coordination Compounds: Platinum. *Topics in Current Chemistry* **2007**, *281*, 205-268.

116. Eckenhoff, W. T.; Eisenberg, R., Molecular Systems for Light Driven Hydrogen Production. *Dalton Transactions* **2012**, *41*, 13004-13021.

117. Langhals, H.; Limmert, M.; Lorenz, I. P.; Mayer, P.; Piotrowski, H.; Polborn, K., Chromophores Encapsulated in Gold Complexes: Dpp Dyes with Novel Properties. *European Journal of Inorganic Chemistry* **2000**, *2000*, 2345-2349.

118. McCusker, C. E.; Hablot, D.; Ziessel, R.; Castellano, F. N., Triplet State Formation in Homo-and Heterometallic Diketopyrrolopyrrole Chromophores. *Inorganic chemistry* **2014**, *53*, 12564-12571.

119. Liu, Y.; Jiang, S.; Glusac, K.; Powell, D. H.; Anderson, D. F.; Schanze, K. S., Photophysics of Monodisperse Platinum-Acetylide Oligomers: Delocalization in the Singlet and Triplet Excited States. *Journal of the American Chemical Society* **2002**, *124*, 12412-12413.

120. Guo, F.; Kim, Y.-G.; Reynolds, J. R.; Schanze, K. S., Platinum–Acetylide Polymer Based Solar Cells: Involvement of the Triplet State for Energy Conversion. *Chemical communications* **2006**, 1887-1889.

121. Schanze, K. S.; Silverman, E. E.; Zhao, X., Intrachain Triplet Energy Transfer in Platinum-Acetylide Copolymers. *The Journal of Physical Chemistry B* **2005**, *109*, 18451-18459.

122. Wu, W.; Sun, J.; Ji, S.; Wu, W.; Zhao, J.; Guo, H., Tuning the Emissive Triplet Excited States of Platinum(Ii) Schiff Base Complexes with Pyrene, and Application for Luminescent Oxygen Sensing and Triplet–Triplet-Annihilation Based Upconversions. *Dalton Transactions* **2011**, *40*, 11550-11561.

123. Hope, J. M.; Wilson, J. J.; Lippard, S. J., Photoluminescent DNA Binding and Cytotoxic Activity of a Platinum(Ii) Complex Bearing a Tetradentate Β-Diketiminate Ligand. *Dalton Transaction* **2013**, *42*, 3176-3180.

124. Li, H. et al., Design, Synthesis, and Optoelectronic Properties of Dendrimeric Pt(II) Complexes and Their Ability to Inhibit Intermolecular Interaction. *Inorganic Chemistry* **2014**, *53*, 810-821.

125. Goswami, S.; Winkel, R. W.; Alarousu, E.; Ghiviriga, I.; Mohammed, O. F.; Schanze, K. S., Photophysics of Organometallic Platinum(Ii) Derivatives of the Diketopyrrolopyrrole Chromophore. *The Journal of Physical Chemistry A* **2014**, *118*, 11735-11743.

126. Yersin, H.; Rausch, A. F.; Czerwieniec, R.; Hofbeck, T.; Fischer, T., The Triplet State of Organo-Transition Metal Compounds. Triplet Harvesting and Singlet Harvesting for Efficient Oleds. *Coordination Chemistry Reviews* **2011**, *255*, 2622-2652.

127. Aly, S. M.; Ho, C. L.; Fortin, D.; Wong, W. Y.; Abd-El-Aziz, A. S.; Harvey, P. D., Intrachain Electron and Energy Transfer in Conjugated Organometallic Oligomers and Polymers. *Chemistry–A European Journal* **2008**, *14*, 8341-8352.

128. Zhang, F.; Wu, D.; Xu, Y.; Feng, X., Thiophene-Based Conjugated Oligomers for Organic Solar Cells. *Journal of Materials Chemistry* **2011**, *21*, 17590-17600.

129. Bailey, J. A.; Hill, M. G.; Marsh, R. E.; Miskowski, V. M.; Schaefer, W. P.; Gray, H. B., Electronic Spectroscopy of Chloro(Terpyridine)Platinum(II). *Inorganic Chemistry* **1995**, *34*, 4591-4599.

130. Connick, W. B.; Henling, L. M.; Marsh, R. E.; Gray, H. B., Emission Spectroscopic Properties of the Red Form of Dichloro(2,2¢-Bipyridine)Platinum(Ii). Role of Intermolecular Stacking Interactions. *Inorganic Chemistry* **1996**, *35*, 6261-6265.

131. Li, Y.; Köse, M. E.; Schanze, K. S., Intramolecular Triplet Energy Transfer in Anthracene-Based Platinum Acetylide Oligomers. *The Journal of Physical Chemistry B* **2013**, *117*, 9025-9033.

132. Gould, I. R.; Farid, S., Dynamics of Bimolecular Photoinduced Electron-Transfer Reactions. *Accounts of Chemical Research* **1996**, *29*, 522-528.

133. Rosspeintner, A.; Lang, B.; Vauthey, E., Ultrafast Photochemistry in Liquids. *Annual Review Physical Chemistry* **2013**, *64*, 247-271.

134. Rosspeintner, A.; Angulo, G.; Vauthey, E., Bimolecular Photoinduced Electron Transfer Beyond the Diffusion Limit: The Rehm−Weller Experiment Revisited with Femtosecond Time Resolution. *Journal of the American Chemical Society* **2014**, *136*, 2026-2032.

135. Barbara, P. F.; Walker, G. C.; Smith, T. P., Vibrational Modes and the Dynamic Solvent Effect in Electron and Proton Transfer. *Science* **1992**, *256*, 975-981.

136. Wan, C.; Xia, T.; Becker, H.-C.; Zewail, A. H., Ultrafast Unequilibrated Charge Transfer: A New Channel in the Quenching of Fluorescent Biological Probes. *Chemical Physics Letters* **2005**, *412*, 158-163.

137. Cai, Y.; Wu, X.; Liu, H.; Fu, W.; Liu, Q., The Adsorption and Reconstruction of Strong Electron Acceptor Tetracyanoethylene (TCNE) on Si(001)-(2×1): A Density Functional Theory Investigation. *Surface Science* **2012**, *606*, 523-526.

138. Chiu, C.-C.; Hung, C.-C.; Chen, C.-L.; Cheng, P.-Y., Ultrafast Time-Resolved Broadband Fluorescence Studies of the Benzene-Tetracyanoethylene Complex: Solvation, Vibrational Relaxation, and Charge Recombination Dynamics. *The Journal of Physical Chemistry B* **2013**, *117*, 9734-9756.

139. Mohammed, O. F.; Vauthey, E., Simultaneous Generation of Different Types of Ion Pairs Upon Charge-Transfer Excitation of a Donor−Acceptor Complex Revealed by Ultrafast Transient Absorption Spectroscopy. *The Journal of Physical Chemistry A* **2008**, *112*, 5804-5809.

140. Connelly, N. G.; Geiger, W. E., Chemical Redox Agents for Organometallic Chemistry. *Chemical Reviews* **1996**, *96*, 877-910.

141. Jeanmaire, D. L.; Suchanski, M. R.; Duyne, R. P. V., Resonance Raman Spectroelectrochemistry. I. The Tetracyanoethylene Anion Radical. *Journal of the American Chemical Society* **1975**, *97*, 1699-1707.

142. Zlatkis, A.; Poole, C. F., Electron Capture: Theory and Practice in Chromatography. **1981**, *Elsevier Scientific Publishing Company, Amsterdam*.

143. Yamamoto, T.; Yamamoto, A.; Ikeda, S., Study of Organo (Dipyridyl) Nickel Complexes. I. Stability and Activation of the Alkyl-Nickel Bonds of Dialkyl (Dipyridyl) Nickel by Coordination with Various Substituted Olefins. *Journal of the American Chemical Society* **1971**, *93*, 3350-3359.

144. Powers, D. C.; Ritter, T., A Transition State Analogue for the Oxidation of Binuclear Palladium(II) to Binuclear Palladium(III) Complexes. *Organometallics* **2013**, *32*, 2042-2045.

145. Panattoni, C.; Bombieri, G.; Belluco, U.; Baddley, W. H., The Crystal and Molecular Structure of a Tetracyanoethylene Complex of Platinum. *Journal of the American Chemical Society* **1968**, *90*, 798-799.

146. Tanase, T.; Hamaguchi, M.; Begum, R. A.; Goto, E., Cyclic Dimerization of Tetracyanoethylene Promoted on Linear Triplatinum Centers Leading to Novel Nitrene-Bridged Pt3 Complexes. *Chemical Communications* **2001**, 1072-1073.

147. Tvrdy, K.; Frantsuzov, P. A.; Kamat, P. V., Photoinduced Electron Transfer from Semiconductor Quantum Dots to Metal Oxide Nanoparticles. *Proceedings of National Academy of Scieinces USA* **2010**, *108*, 29-34.

148. Mohammed, O. F.; Adamczyk, K.; Banerji, N.; Dreyer, J.; Lang, B.; Nibbering, E. T.; Vauthey, E., Direct Femtosecond Observation of Tight and Loose Ion Pairs Upon Photoinduced Bimolecular Electron Transfer. *Angewandte Chemie International Edition* **2008**, *47*, 9044-9048.

149. Koch, M.; Letrun, R.; Vauthey, E., Exciplex Formation in Bimolecular Photoinduced Electron-Transfer Investigated by Ultrafast Time-Resolved Infrared Spectroscopy. *Journal of the American Chemical Society* **2014**, *136*, 4066-4074.

150. Koch, M.; Rosspeintner, A.; Adamczyk, K.; Lang, B.; Dreyer, J.; Nibbering, E. T.; Vauthey, E., Real-Time Observation of the Formation of Excited Radical Ions in Bimolecular Photoinduced Charge Separation: Absence of the Marcus Inverted Region Explained. *Journal of the American Chemical Society* **2013**, *135*, 9843-9848.

151. Lakowicz, J. R., Principles of Fluorescence Spectroscopy. *Springer Science+Business Media, LLC, Singapore, third edn.,* **2006**.

152. Closs, G. L.; Miller, J. R., Intramolecular Long-Distance Electron-Transfer in Organic Molecules. *Science* **1988**, *240*, 440-447.

153. Tang, C. W., Two-Layer Organic Photovoltaic Cell. *Applied Physics Letters* **1986**, *48*, 183-185.

154. Opitz, A.; Wagner, J.; Brütting, W.; Salzmann, I.; Koch, N.; Manara, J.; Pflaum, J.; Hinderhofer, A.; Schreiber, F., Charge Separation at Molecular Donor–Acceptor Interfaces: Correlation between Morphology and Solar Cell Performance. *IEEE Journal of Selected Topics in Quantum Electronics* **2010**, *16*, 1707-1716.

155. Walter, M. G.; Rudine, A. B.; Wamser, C. C., Porphyrins and Phthalocyanines in Solar Photovoltaic Cells. *Journal of Porphyrins Phthalocyanines* **2010**, *14*, 759-792.

156. Zhou, R. et al., Enhancing the Efficiency of Solution-Processed Polymer:Colloidal Nanocrystal Hybrid Photovoltaic Cells Using Ethanedithiol Treatment. *ACS Nano* **2013**, *7*, 4846-4854.

157. Liu, Z.; Xu, F.; Yan, D., New Progress in the Device Physics of Polymer-Fullerene Solar Cells. *Acta Chimica Sinica* **2014**, *72*, 171-184.

158. Panda, M. K.; Ladomenou, K.; Coutsolelos, A. G., Porphyrins in Bio-Inspired Transformations: Light-Harvesting to Solar Cell. *Coordination Chemistry Reviews* **2012**, *256*, 2601-2627.

159. Harvey, P. D., What Can We Learn from Artificial Special Pairs? *Canadian Journal of Chemistry* **2014**, *92*, 355-368.

160. Krebs, F. C.; Spanggaard, H., Antibatic Photovoltaic Response in Zinc Porphyrin-Linked Oligothiophenes. *Solar Energy Materials and Solar Cells* **2005**, *88*, 363-375.

161. Regehly, M.; Wang, T.; Siggel, U.; Fuhrhop, J. H.; Röder, B., Electron Transfer in Oligothiophene-Bridged Bisporphyrins. *The Journal of Physical Chemistry B* **2009**, *113*, 2526-2534.

162. Fox, M. A.; Grant, J. V.; Melamed, D.; Torimoto, T.; Liu, C. Y.; Bard, A. J., Effect of Structural Variation on Photocurrent Efficiency in Alkyl-Substituted Porphyrin Solid-State Thin Layer Photocells. *Chemistry of Materials* **1998**, *10*, 176-177.

163. Fantacci, S.; Ronca, E.; Angelis, F. D., Impact of Spin−Orbit Coupling on Photocurrent Generation in Ruthenium Dye-Sensitized Solar Cells. *The Journal of Physical Chemistry* **2014**, *5*, 375-380.

164. Xu, Z.; Hu, B.; Howe, J., Improvement of Photovoltaic Response Based on Enhancement of Spin-Orbital Coupling and Triplet States in Organic Solar Cells. *The Journal of Applied Physics* **2008**, *103*, 043909.

165. Mei, J.; Ogawa, K.; Kim, Y.-G.; Heston, N. C.; Arenas, D. J.; Nasrollahi, Z.; McCarley, T. D.; Tanner, D. B.; Reynolds, J. R.; Schanze, K. S., Low-Band-Gap Platinum Acetylide Polymers as Active Materials for Organic Solar Cells. *ACS applied materials & interfaces* **2009**, *1*, 150-161.

166. Letrun, R.; Vauthey, E., Excitation Wavelength Dependence of the Dynamics of Bimolecular Photoinduced Electron Transfer Reactions. *The journal of physical chemistry letters* **2014**, *5*, 1685-1690.

167. Kalyanasundaram, K., Photochemistry of Water-Soluble Porphyrins: Comparative Study of Isomeric Tetrapyridyl- and Tetrakis(N-Methylpyridiniumyl) Porphyrins *Inorganic Chemistry* **1984**, *23*, 2453-2459.

168. Weiss, C.; Kobayashi, H.; Gouterman, M., Spectra of Porphyrins Part III. Self-Consistent Molecular Orbital Calculations of Porphyrin and Related Ring Systems*. *The Journal of Molecular Spectroscopy c.* **1965**, *16*, 415-450.

169. Lehrer, S., Solute Perturbation of Protein Fluorescence. Quenching of the Tryptophyl Fluorescence of Model Compounds and of Lysozyme by Iodide Ion. *Biochemistry* **1971**, *10*, 3254-3263.

170. Blinova, I. A.; Vasil'ev, V. V., Luminescence Properties of Water-Soluble Cationic Platinum(II) and Palladium(II) Porphyrins. *The Journal of Physical Chemistry* **1995**, *69, 995-999*.

171. Friedman, L.; Carpenter, P. G., Diffusion Velocity and Molecular Weight. I. The Limits of Validity of the Stokes--Einstein Diffusion Equation. *Journal of the Americal Chemical Society* **1939**, *61*, 1745-1747.

172. Zhong, D.; Zewail, A. H., Femtosecond Real-Time Probing of Reactions. 24. Time, Velocity, and Orientation Mapping of the Dynamics of Dative Bonding in Bimolecular Electron Transfer Reactions. *The Proceedings of the National Academy of Sciences USA* **1999**, *96*, 2602-2607.

173. Zhong, D.; Bernhardt, T. M.; Zewail, A. H., Femtosecond Dynamics of Dative Bonding: Concepts of Reversible and Dissociative Electron Transfer Reactions. *The Journal of Physical Chemistry A* **1999**, *103*, 10093-10117.

174. Segawa, H.; Shimidzu, T.; Honda, K.-i., Control of Π-Radical Anion State of Porphyrin with a Polymer Matrix. *Polymer Journal* **1988**, *20*, 441-446.

175. Maslov, V. G., Complexes of Anion Radicals of Porphyrins with Pyridine Anions and Reversibility of the Intracomplex Phototransfer of an Electron. *The Journal of Applied Spectroscopy* **1995**, *62*, 225-228.

176. Mosseri, S.; Nahor, G. S.; Neta, P., Radiolytic Reduction of Tetrapyridylporphyrins. *Journal of Chemical Society Faraday Transactions* **1991**, *87*, 2567-2572.

177. Houk, K. N.; Munchausen, L. L., Ionization Potentials, Electron Affinities, and Reactivities of Cyanoalkenes and Related Electron-Deficient Alkenes. A Frontier Molecular Orbital Treatment of Cyanoalkene Reactivities in Cycloaddition, Electrophilic, Nucleophilic, and Radical Reactions.. *Journal of the Americal Chemical Society.* **1976**, *98*, 937-946.

178. Farragher, A. L.; Page, F. M., Experimental Determination of Electron Affinities. Part 11. - Electron Capture by Some Cyanocarbons and Related Compounds. *Transactions of the Faraday Society* **1967**, *63*, 2369-2378.

179. Derouiche, H.; Miled, H. B.; Mohamed, A. B., Enhanced Performance of a Cupc: Pcbm Based Solar Cell Using Bathocuproine Bcp or Nanostructured Tio2 as Hole-Blocking Layer. *Physica Status Solidi A* **2010**, *207*, 479-483.

180. Ito, O., Photoinduced Electron Transfer of Fullerenes (C60 and C70) Studied by Transient Absorption Measurements in near-IR Region. *Research on Chemical Intermediates* **1997**, *23*, 389-402.

181. Ito, O.; D’Souza, F., Recent Advances in Photoinduced Electron Transfer Processes of Fullerene-Based Molecular Assemblies and Nanocomposites. *Molecules* **2012**, *17*, 5816-5835.

182. Worthington, P. et al., Reduction Potentials of Seventy-Five Free Base Porphyrin Molecules: Reactivity Correlations and the Prediction of Potentials. *The Journal of Inorganic Biochemistry* **1980**, *12*, 281-291.

183. Monnereau, C.; Gomez, J.; Blart, E.; Odobel, F.; Wallin, S.; Fallberg, A.; Hammarström, L., Photoinduced Electron Transfer in Platinum(Ii) Terpyridinyl Acetylide Complexes Connected to a Porphyrin Unit. *Inorganic Chemistry* **2005**, *44*, 4806-4817.

184. Guo, F.; Ogawa, K.; Kim, Y.-G.; Danilov, E. O.; Castellano, F. N.; Reynolds, J. R.; Schanze, K. S., A Fulleropyrrolidine End-Capped Platinum-Acetylide Triad: The Mechanism of Photoinduced Charge Transfer in Organometallic Photovoltaic Cells. *Physical Chemistry Chemical Physics* **2007**, *9*, 2724-2734.

185. Fukuzumi, S.; Ohkuboa, K., Long-Lived Photoinduced Charge Separation for Solar Cell Applications in Supramolecular Complexes of Multi-Metalloporphyrins and Fullerenes. *DaltonTransaction* **2013**, *42*, 15846-15858.

186. Cheng, Y.-J.; Yang, S.-H.; Hsu, C.-S., Synthesis of Conjugated Polymers for Organic Solar Cell Applications. *Chemical Reviews* **2009**, *109*, 5868-5923.

187. Wang, L.; Puodziukynaite, E.; Grumstrup, E. M.; Brown, A. C.; Keinan, S.; Schanze, K. S.; Reynolds, J. R.; Papanikolas, J. M., Ultrafast Formation of a Long-Lived Charge-Separated State in a Ru-Loaded Poly(3-Hexylthiophene) Light-Harvesting Polymer. *J. The Journal of Physical Chemistry Letters* **2013**, *4*, 2269-2273.

188. Mohebbi, A. R.; Yuen, J.; Fan, J.; Munoz, C.; Wang, M. F.; Shirazi, R. S.; Seifter, J.; Wudl, F., Emeraldicene as an Acceptor Moiety: Balanced-Mobility, Ambipolar, Organic Thin-Film Transistors. *Advanced Materials* **2011**, *23*, 4644-8.

189. Sun, J.; Yu, W.; Usman, A.; Isimjan, T. T.; Dgobbo, S.; Alarousu, E.; Takanabe, K.; Mohammed, O. F., Generation of Multiple Excitons in Ag2s Quantum Dots: Single High-Energy Versus Multiple-Photon Excitation. *The Journal of Physical Chemistry Letters* **2014**, *5*, 659-665.

190. Sardela, M., *Practical Materials Characterization*; Springer New York, **2014**.

191. Wang, Z. L., *Characterization of Nanophase Materials*; Wiley-VCH, **2000**.

192. Green, M. A., Solar Cell Fill Factors: General Graph and Empirical Expressions. *Solid-State Electronics* **1981**, *24*.

APPENDICES

A. Methods and Experimental Procedures

A.1 Chemicals

In this work, $PC_{71}BM$, $PC_{61}BM$ and $IC_{60}BA$ were purchased from Solarmer Energy and were used as received. PTB7-Th was purchased from 1-Material Inc. TCNE, N,N-Dimethylformamide (DMF, anhydrous, 99.8%), chlorobenzene (CB, anhydrous 99.9%) and dichloromethane (DCM, anhydrous, $\geq$99.8%) were purchased from Sigma-Aldrich and used as it is without further purification. TCNE was further purified by crystallization from DCM. Dielectric constant (ε) and viscosity (η) of the solvents used are 36.70; 0.92, 9.08; 0.45, and 9.93; 0.8 for DMF, DCM, and CB, respectively. 5,10,15,20-tetra(4-pyridyl)-porphyrin (TPyP) and 5,10,15,20-tetra(1-methyl-4-pyridino)-porphyrin tetra chloride (TMPyP) were supplied by Frontier Scientific. DPP was synthetized according to the literature.[188] DPP-Pt(acac) was synthetized according to scheme given below.

A.2 Synthetic Procedure of DPP-Pt(acac)

DPP-boronate ester (0.135 g, 0.121 mmol), Pt(acac) (0.135 g, 0.253 mmol) and THF(18 ml) were taken in a two-necked flask and deoxygenated with argon for 45 minutes. The catalysts, $Pd_2(dba)_3$ (6 mg, 0.007 mmol) and $Pd(P^tBu_3)_2$ (6.2 mg, 0.012 mmol), were added under strong flow of argon. A degassed 2 ml solution of K_3PO_4 (0.154 g, 0.725 mmol) was added promptly to the reaction mixture. Immediately the color of the solution changed to bluish green from pink. Afterwards, the reaction mixture was heated to reflux overnight. The solvent was evaporated to dryness under vacuum and methanol was added to obtain a dark green residue. The crude product was recrystallized from THF/diethyl ether solvent mixture to obtain the product as a shiny dark green solid (130 mg, 60%).

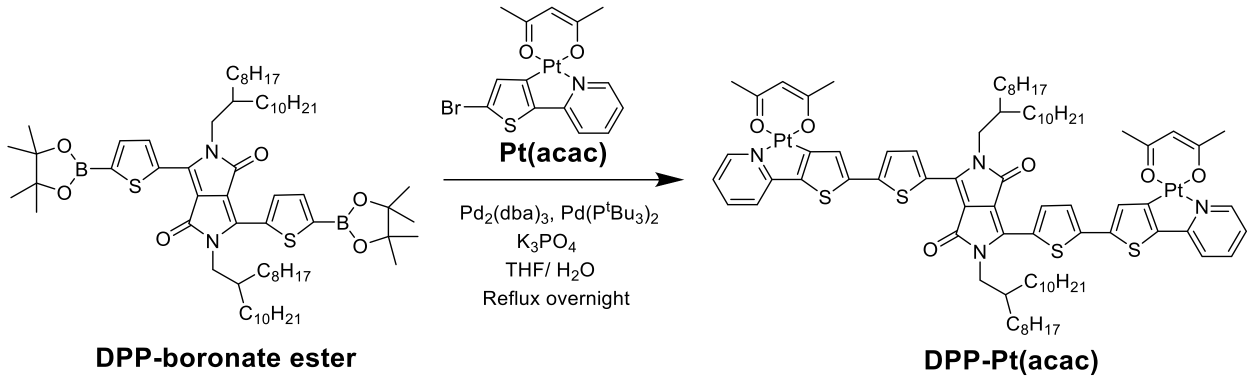

Figure A.1 Synthetic procedure of DPP-Pt(acac)

^{1}H NMR (500 MHz, CDCl$_3$): δ 9.02 (d, 1H), δ 8.78 (d, 1H), δ 7.68 (t, 1H), δ 7.33 (s, 2H), δ 7.23 (d, 1H), δ 6.91 (t, 1H), δ 5.53 (s, 1H), δ 4.07 (d, 2H), δ 2.06 (s, 1H), δ 2.03 (s, 1H), δ 2.02 (m, 1H), δ 1.28-1.24 (m, 32H), δ 0.87 (m, 6H). ^{13}C NMR (125 MHz, CDCl$_3$, δ): 185.4, 184.0, 161.5, 147.2, 138.5, 136.8, 128.1, 125.04, 118.4, 117.0, 102.8, 46.4, 38.0, 31.9, 31.3, 30.2, 29.7, 29.6, 29.4, 29.3, 28.1, 26.9, 26.4, 22.8, 14.2 (some of the quaternary carbons is difficult to observe). MALDI-TOF MS (*m/z*) [M]$^+$ Calcd for $C_{82}H_{110}N_4O_6Pt_2S_4$, 1766.21; found, 1766.66.

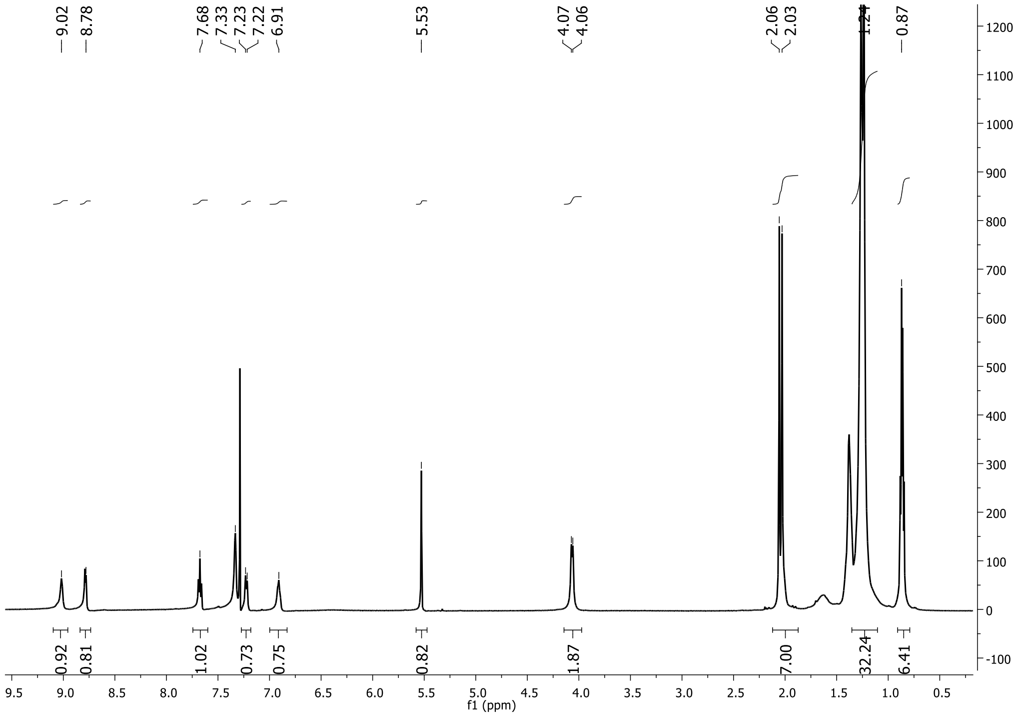

Figure A.2 ^{1}H NMR (500 MHz, $CDCl_3$) of DPP-Pt(acac).

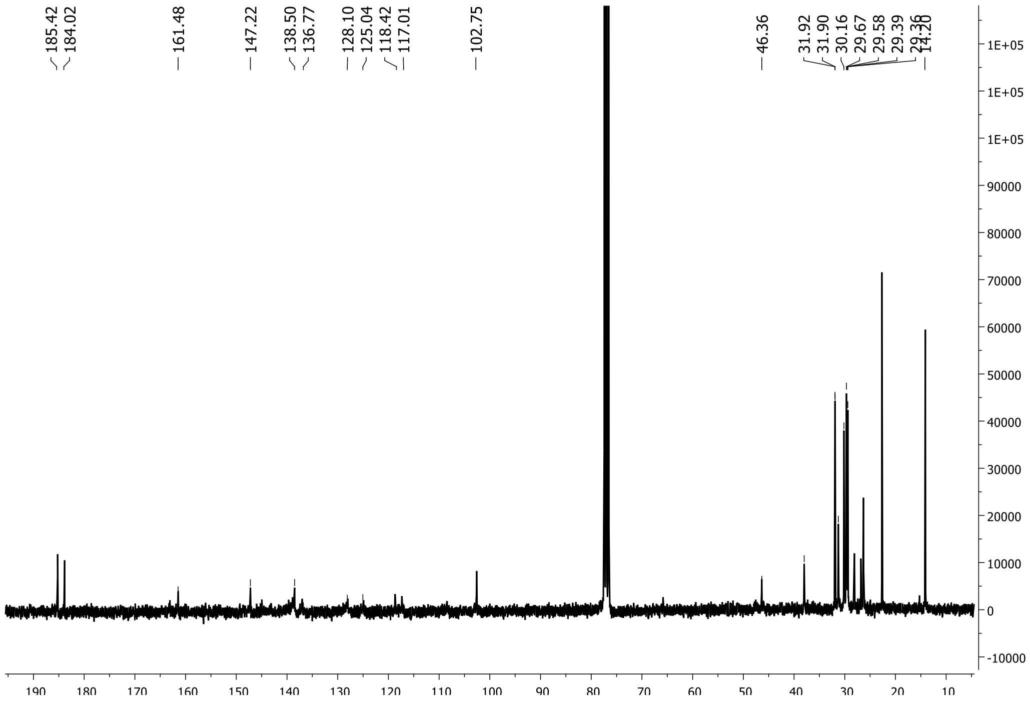

Figure A.3 ^{13}C NMR (125 MHz, CDCl3) of DPP-Pt(acac).

A.3 Spectroscopic Investigations

I. Steady-State Measurements

Steady-state absorption and emission spectra of the donor polymers with and without acceptors were recorded on a Cary 5000 ultraviolet-visible (UV-Vis-NIR) spectrophotometer (Agilent Technologies) and a Fluoromax-4 spectrofluorometer (Horiba Scientific), respectively. Measurements were conducted in a rectangular quartz cell with a 1-cm optical path. A fixed volume (2 ml) of the starting solution of donors in the corresponding solvent was placed in the cell, while aliquots of the quenchers dissolved in solvent were added consecutively. The concentration of the polymer donor was held constant during all of the measurements. A fixed volume of the quenchers was sequentially added into the donors' solution successively.

In the measurements in chapter 2, 2 ml of the starting solution of PTB7-Th in CB was placed in the cell, while aliquots of the FA quenchers dissolved in CB were added consecutively. The concentration of PTB7-Th was held constant at an optical density (OD) of 0.7, 0.55 and 0.53 in PTB7-Th/$PC_{71}BM$, PTB7-Th/$PC_{61}BM$ and PTB7-Th/$IC_{60}BA$ systems, respectively. Then, 0-2.61 mM $PC_{71}BM$ was sequentially added into the PTB7-Th solution, and 0-5 mM $PC_{61}BM$ and $IC_{60}BA$ were successively added to the donor solution. The fluorescence spectra were collected for the PTB7-Th polymer with each of the three FAs after excitation at 680 nm. However, in the study in chapter 3, the concentration of DPP for the DPP/TCNE system in DMF/DCM (4:1) was held constant at 7.5 µM, as determined by the optical density at the first exciton absorption peak within a 2 mm path length cuvette, and a range of 0–30.7 mM TCNE in DMF/DCM (4:1) was added successively to the solution. A similar approach was used for the DPP-Pt(II)(acac)/TCNE system, where the concentration was held constant at approximately 9.2-μM DPP-Pt(II)(acac) in a mixture of DMF and DCM(4:1), and a range of 0–30.7 mM TCNE was used in the DMF/DCM(4:1). Fluorescence spectra were collected after excitation at 490 and 600 nm for the DPP/TCNE and DPP-Pt(II)(acac)/TCNE systems, respectively. However, in the measurements in chapter 4, in the DPP-Pt(acac)/TMPyP system, a range of 0–0.14 mM TMPyP in DCM / DMF (1:1) was added successively to the solution of DPP-Pt(acac) in DCM:DMF mixture. Fluorescence spectra were collected after excitation at 660 in DCM/DMF (1:1).

II. Time-resolved Spectroscopy.

Femtosecond and nanosecond TA spectroscopy measurements (with time resolutions of 120 fs and 200 ps and detection limits of 5.5 ns and 400 μs, respectively) were measured with the HELIOS and EOS setups (Ultrafast Systems), respectively. Femtosecond broadband pump−probe spectroscopy was employed to excite and detect the wavelengths around a certain exciton absorption peak of the D. A schematic of the experimental setup used in this thesis for the ultraviolet (UV)/visible (vis) pump/NIR probe measurements is depicted in Figure A.4. The system constitutes a fundamental laser, which is provided by a home built Ti:Sapphire using a chirped pulse amplification scheme, producing 35 fs pulses at 800 nm with four mJ of energy/pulse and a repetition rate of 1 kHz. The absorption decays were measured with a pump-probe setup in which a white-light continuum probe pulse generated by a 2-mm-thick sapphire plate and spectrally pump tunable fs pulses (240–2600 nm; a few μJ pulse energy) generated in an optical parametric amplifier (TOPAS-C stage) selectively excite specific electronic transitions within a sample. The probe beam is routed *via* a computer-controlled delay line, adjustable pinholes, focusing lens, and variable neutral density filter to a crystal for white light continuum (WLC) generation. Then, the probe beam is directed to the sample *via* a focusing mirror. The delay between the pump and probe pulses can be varied to allow TA measurements within 5.8 ns (HELIOS) and 400 μs (EOS) time windows.

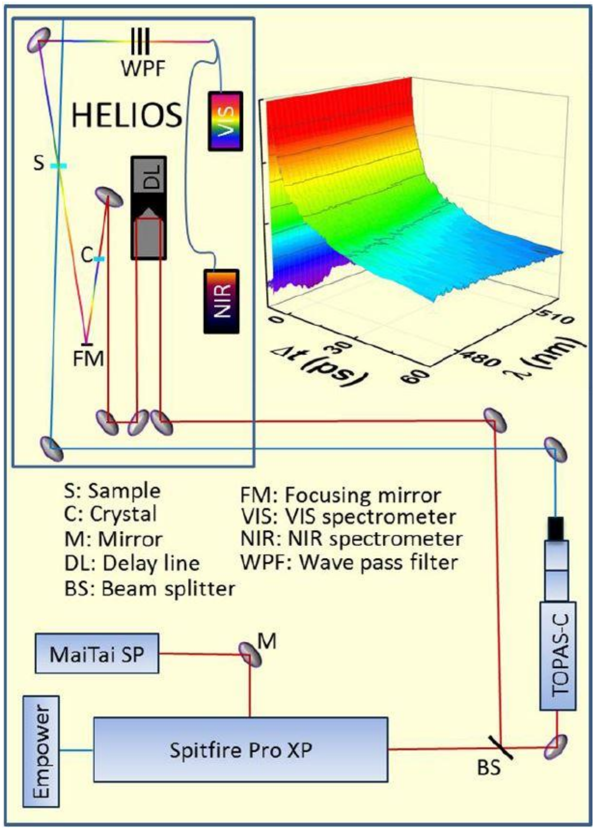

Figure A.4 Schematic representation of the main components found in our femtosecond transient absorption system.[189]

The pump and probe beams are adjusted to overlap spatially and temporally on the sample. Following interaction with the sample, the probe beam is directed towards a near-infrared spectrometer (InGaAs-NIR) covering the range of 800-1600 nm with 3.5 nm resolution at 7900 spectra/s or a visible spectrometer (CMOS VIS) covering the range of 350-800 nm with 1.5 nm resolution at 9500 spectra/s. The probe beam is collected by the chosen spectrometer after passing through wave pass filters that attenuate the white light around the Spitfire fundamental at 800 nm. For both the HELIOS and EOS systems, a two-channel probe (probe-reference) method is used. In this approach, the probe pulse is passed through a beam-splitter before reaching the sample to split the beam into two-channels (sample and reference). In this way, a portion is sent directly to the sample, while the other is directed to the detector to act as a reference. This technique allows dividing out any fluctuations in the probe beam intensity during the experiment. The TA spectra are usually averaged until the desired signal-to-noise ratio is achieved.

In the measurements in chapter 2, the pump and probe pulses were overlapped in a 2-mm-thick cuvette cell containing PTB7-Th (0.5 OD) in the presence and absence of 3 mM FAs ($PC_{71}BM$, $PC_{61}BM$ or $IC_{60}BA$) in CB and pumped at 760 nm. The transmitted probe light from the solution was collected and focused onto a broadband UV-Vis-NIR detector to monitor the transient absorbance change (ΔA).

In the experiments in chapter 3, to cover the transient spectra from a few hundred fs to ns time delays after photoexcitation, HELIOS and EOS detection systems

(Ultrafast systems) with time resolutions of 120 fs and 200 ps and detection limits of 5.5 ns and 400 µs, respectively, were employed. fs-TA and ns-TA measurements were conducted within a 2-mm-thick cuvette cell containing ≈ 0.08 mM DPP or DPP-Pt(II)(acac) in DMF/DCM (4:1) solution in the presence or absence of 0.02, 0.05, and 0.4 M TCNE and pumped at 560 nm and 500 nm for fs and ns TA system. The transmitted probe light from the solution was collected and focused on a broadband UV-Vis detector to monitor the change in transient absorbance (ΔA).

In chapter 4, the pump and probe beams were focused on DPP-Pt(acac) or DPP in DCM:DMF in the presence or absence of (0.05–0.4 mM) TMPyP (pumped at 680 nm), and the transmitted probe light from the samples was collected and focused on the broadband UV-visible detector to record the time-resolved transient absorption spectra.

All TA experiments were performed at room temperature, and the sample solutions were constantly stirred using a magnetic stirrer to ensure a fresh volume was available for each laser shot. Furthermore, the absorption spectrum of each sample was measured before and after the TA experiments to ensure the absence of any degradation. Usually, the TA spectra were averaged until the desired signal-to-noise ratio was achieved. Global analysis fitting procedures were then applied to extract the kinetics of dynamical processes from the TA spectra.

III. Time-Correlated Single-Photon Counting (TCSPC)

To monitor the excitation dynamics on the nanosecond time scale, we conducted TCSPC by employing a Halcyone ultrafast spectrometer (Ultrafast Systems, LLC).

Halcyone is an all-in-one box using a PMT detector with a spectral range of 200–700 nm, where the instrument response function (IRF) is about ~250 ps with a time window up to 200 µs. This unit was integrated into the existing laser system we described above. DPP in the presence and absence of 0.05 and 0.1 M TCNE after laser excitation at 500 nm were measured in a 2-mm-thick cuvette, and a magnetic stirrer was used to ensure a fresh volume of the sample.

IV. NMR spectra

NMR spectra were recorded using a Varian Inova-500 FT-NMR (for ^{1}H-500 MHz and for ^{13}C-125 MHz). Mass spectra analysis for DPP-Pt(acac) was recorded by Mass Spectrometry Services, which is located in house at the University of Florida.

A.4 Electron Microscopy

I. Transmission Electron Microscopy (TEM)

Transmission Electron Microscopy (TEM) is a useful technique to provide fundamental structural and crystallographic information about the sample. In brief, this technique adopts high-energy electrons to interact with an ultra-thin specimen.[190] The electron beam is created by an electron gun (*e.g.*, Lanthanum Hexaboride, LaB6) positioned at the top of the microscope and then focused on the sample by condenser lenses.[191] The transmitted beam is directed towards a magnification system which consists of several lenses upon interaction with the sample. A phosphor screen is used to convert the electron images into photo images, which are detected by a charge-coupled diode (CCD) camera to obtain digital images that enable data processing.[190-191]

High-resolution TEM uses directly transmitted beams and diffracted ones to produce an image of the sample that shows the periodicity of the lattice with high resolution (sub-Å level), which enables studying the atomic-level crystal structure and defects.[190]

In this work, high-resolution TEM measurements are carried out on a Tecnai F30 microscope operated at 300 kV and fitted with an energy dispersive X-ray analyzer. The TEM technique is used to collect evidence from samples that are sufficiently thin to allow the transmission of electrons. A monochromatic beam of electrons is amplified by a thin sample of 0.1 to 0.5 μm in transmission electron microscopy. Various diffracted beams exist in addition to the transmitted beam, and those are stimulated by an objective lens to form a point on the back focal plane near exit side of the specimen. This diffraction arrangement is magnified by the other two lenses.

II. Scanning Electron Microscopy (SEM)

In scanning electron microscopy (SEM), highly concentrated beams of electrons with high-energy are used to yield arrays of signals from the exteriors of solid specimens. The signals that are generated from electron-sample interactions would provide us with information from the sample that includes the chemical composition, external morphology (texture), crystalline structure and orientation of the materials making up the sample.

The working principle of SEM is the point at which the accelerated electrons in SEM transfer some energy, which is dispersed in various ways during electron-sample interactions when the incident electrons are decelerated in the solid sample. Secondary electrons, backscattered electrons, diffracted electrons, photons, visible light, and heat exist in these signals. Typically, secondary electrons and backscattered electrons are utilized to image sample substances to show the morphologies and topographies of samples. Secondary electrons are the most vital, and backscattered electrons are the most valued for the elucidation of contrasts in the compositions of multiphase samples.

A.5 Device Fabrication

I. Fabrication of the ZnO ETL

We emphasized how the structures and properties of RF-sputtered ZnO thin films can be used to optimize device statistics. The indium tin oxide (ITO) substrates were cleaned as follows: a) washed with detergent and rinsed with deionized (DI) water under ultrasonication, b) sonicated in acetone and isopropanol for 30 min each, c) and rinsed with DI-water and dried under N_2. The cleaned ITO substrates were treated with UV-ozone for 10 min before deposition of the ZnO films. The ZnO sputter target (3" dia x 0.125" thick) with a purity of 99.99% was procured from Plasmaterials, Inc., and ZnO thin films were processed at RT by RF sputtering under the working pressure of 5 mTorr operated at a cathode power of 120 W. Highly textured crystalline ZnO thin films of 100 nm were achievable with smooth surfaces (rms roughness $\leq$ 2 nm) on Angstrom Sciences sputtering cathodes for deposition at a constant deposition rate and under 1×10^{-6} mbar chamber pressure before purging 15 sccm Ar into the chamber.

II. Sputtering

Sputtering is one of the most globally used techniques allowing the deposition of various metallic films on wafers, such as molybdenum, aluminum, aluminum alloys, platinum, gold, and tungsten. Sputtering is a technology where the atoms dislocate from the surface of a material due to high-energy particle collisions. During the sputtering, the material is released from the source at a much lower temperature than evaporation. The substrate is placed in a vacuum chamber with the source material, called the target, and an inert gas (such as argon) is introduced at low pressure. The gas is struck by an RF power source causing the gas to become ionized. The ions are accelerated towards the target surface, causing the atoms of the source material to break off from the target in vapor form and condense on all surfaces comprising the substrate.

III. Active-layer blend formation

Each of the three blended active layers, PTB7-Th/$PC_{71}BM$, PTB7-Th/$PC_{61}BM$, and PTB7-Th/ICBA, were formed by dissolving 20 mg mL^{-1} of the PTB7-Th donor with one of the FAs, $PC_{71}BM$, $PC_{61}BM$ and ICBA, in CB at a ratio of 1:1.5 (by weight). A 5% by volume addition of 1-chloronaphthalene (CN) was stirred into the blend formation overnight at 60 °C to ensure that the adhesion properties would be retained on the ITO/ZnO substrates. The resultant solution was spin coated at 1200 rpm for 45 s to produce an ~80-nm-thick film. Three different batches of films were deposited with three FAs for the comparative device statistics.

IV. HTL and Electrode Metallization

The MoO_x (6 nm) HTL and the Ag (anode) metal contact (100 nm) were deposited in a vacuum thermal evaporator (Angstrom Sciences) run at 3 × 10^{-6} mbar pressure. The architecture of the device was as follows: ITO/ZnO/PTB7-Th:FA/MoO_x/Ag. It was completed by a positive electrode (Ag) and a negative electrode (ITO) to produce a device with an active area of 0.1 cm^2.

A.6 Device Performance: Current –Voltage (I-V) Measurements

A typical current density (J)-voltage (V) curve of a PSC device is shown in Figure A-5. The current density-voltage measurements were carried out with a KEITHLEY Source Measurement 2400 and an Air Mass 1.5 G solar simulator with an illumination intensity of 100 mW cm^{-2}. Tracer-2 software was used with the Newport solar simulator for PCE measurements. Calibration of the simulator's light intensity was performed by the reference KG5 filtered Si diode before device testing.

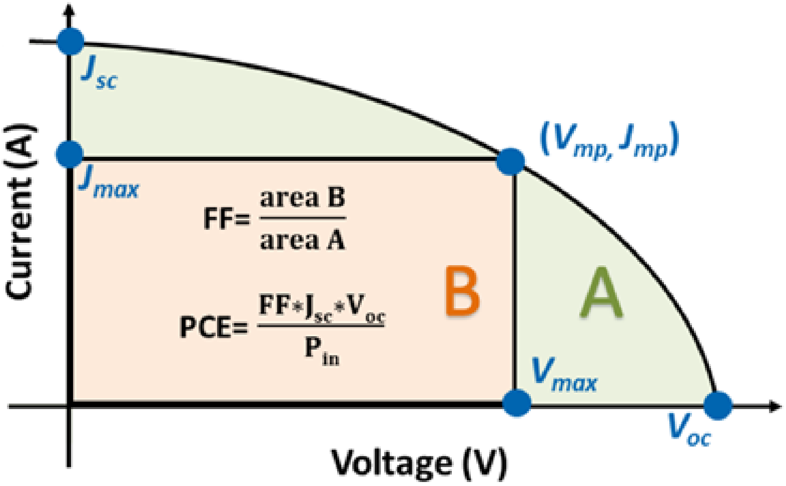

Figure A.5 Typical current density (J)-voltage (V) curve of PSCs.[92]

Under lighting, the J–V curve shifts down in an amount equal to the photocurrent, J, and the device can produce power. Under short circuit conditions (J_{SC}), the current flow is at its greatest, and there is no applied bias. Open circuit conditions (V_{OC}) typically have no current flow, and this is the point of the maximum electrochemical potential of the cell.[5] The power conversion efficiency (PCE, η) is the primary figure of merit for SCs. The PCE is the ratio of the maximum electrical power, P_m, produced by the device to the total incident optical power, P_{in}, and is defined according to equation (5):

$$(PCE, \eta) = \frac{P_m}{P_{in}} \times 100\% = \frac{V_{OC} \times I_{SC} \times FF}{P_{in}} \times 100\% \qquad (5)$$

where FF is the fill factor and is given by equation (6):

$$FF = \frac{J_{MP} \times V_{MP}}{J_{SC} \times V_{OC}} \qquad (6)$$

where J_{MP} and V_{MP} are the current density and the voltage at the maximum power point, respectively. The FF provides a sign of how effectively charges can be removed from a cell, and in the ideal case will have a value of unity.[192]

B. Supporting Information

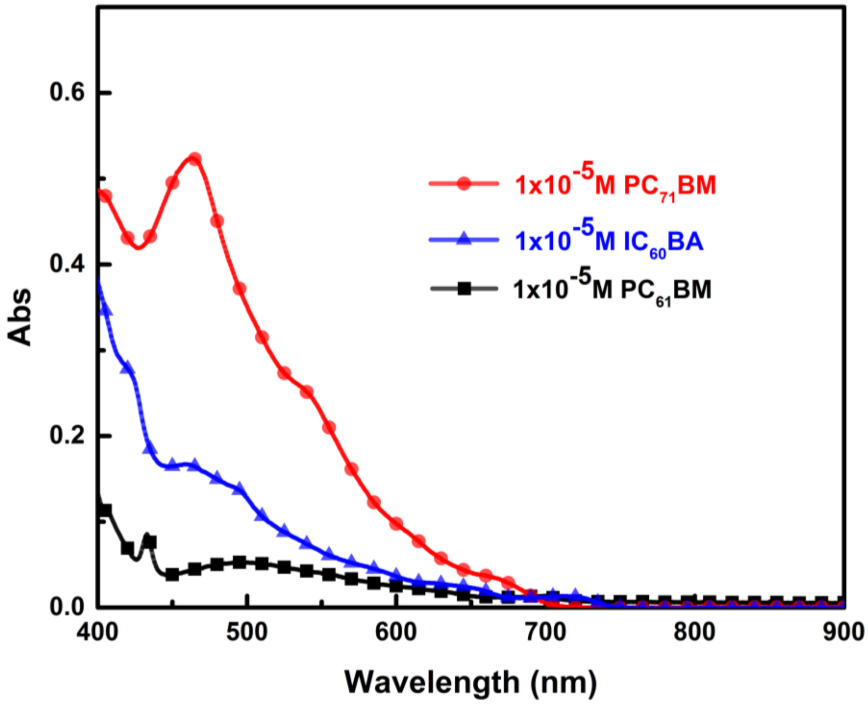

Figure SB.1 The absorption spectra of the three FAs.

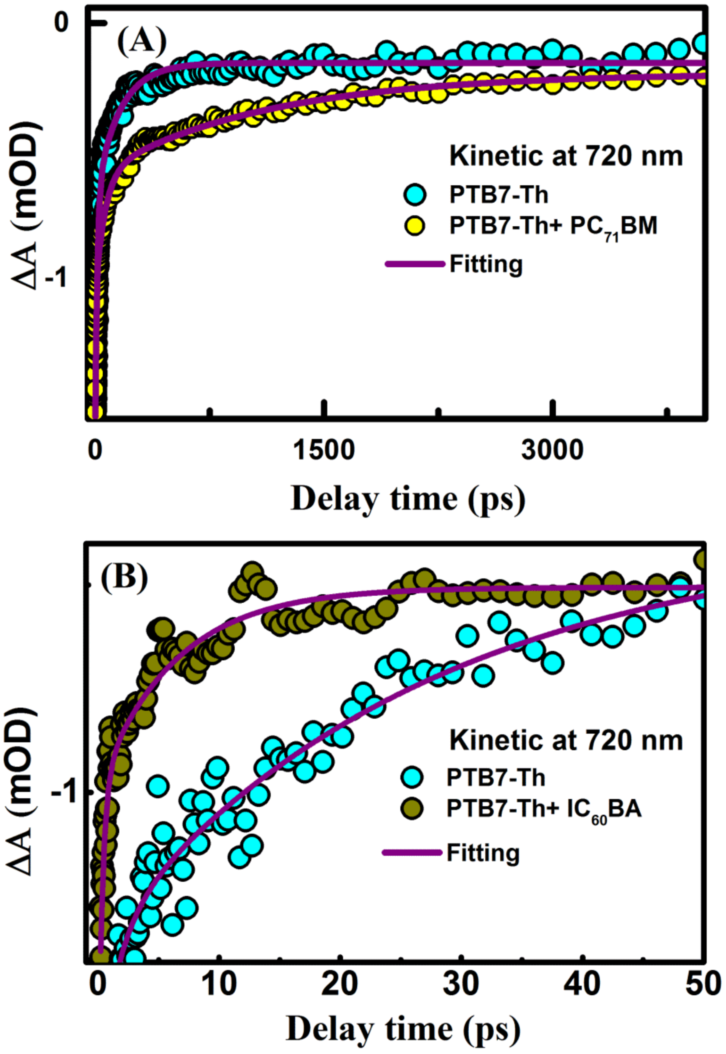

Figure SB.2 The dynamics of negative band recovery in the PTB7-Th thin film at 720 nm: (A) in the absence and presence of $PC_{71}BM$ and (B) in absence and presence of $IC_{60}BA$ early on (50ps). The solid lines are the best fits of the data points with two exponential functions for negative band recovery.

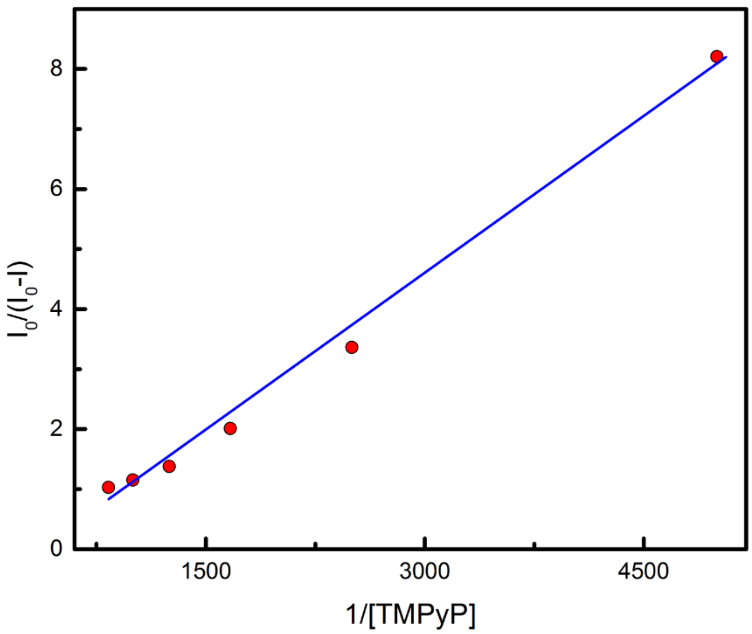

Figure SB.3 Modified Stern-Volmer plot for the fluorescence quenching of DPP-Pt(acac) using λ_{ex} = 660 nm with varying concentrations of TMPyP in dimethylformamide (DMF) / dichloromethane (DCM) [1/1].

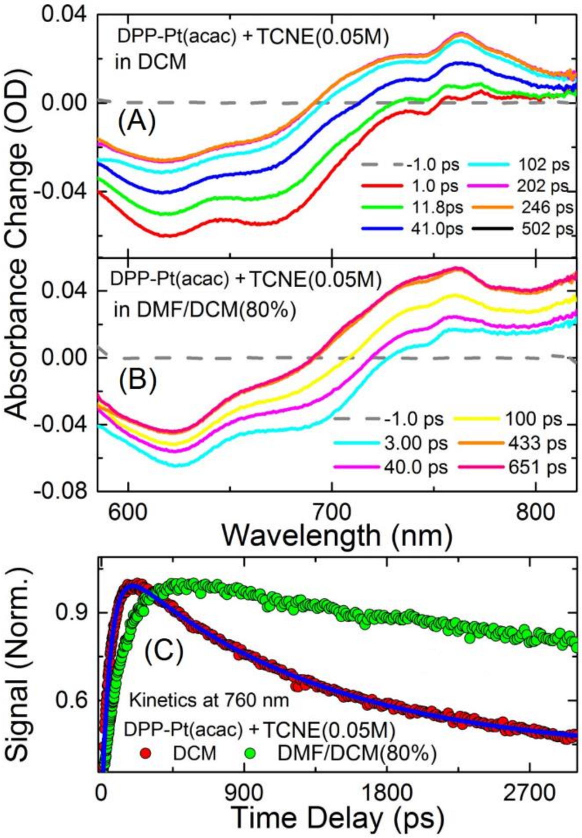

Figure SB.4 Transient Absorption after 560 nm pulse excitation of DPP-Pt(acac) + TCNE[0.05M] (A) in dichloromethane (DCM), (B) in dimethylformamide (DMF) / dichloromethane (DCM) [4/1] and (C) kinetic traces collected at 760 nm.

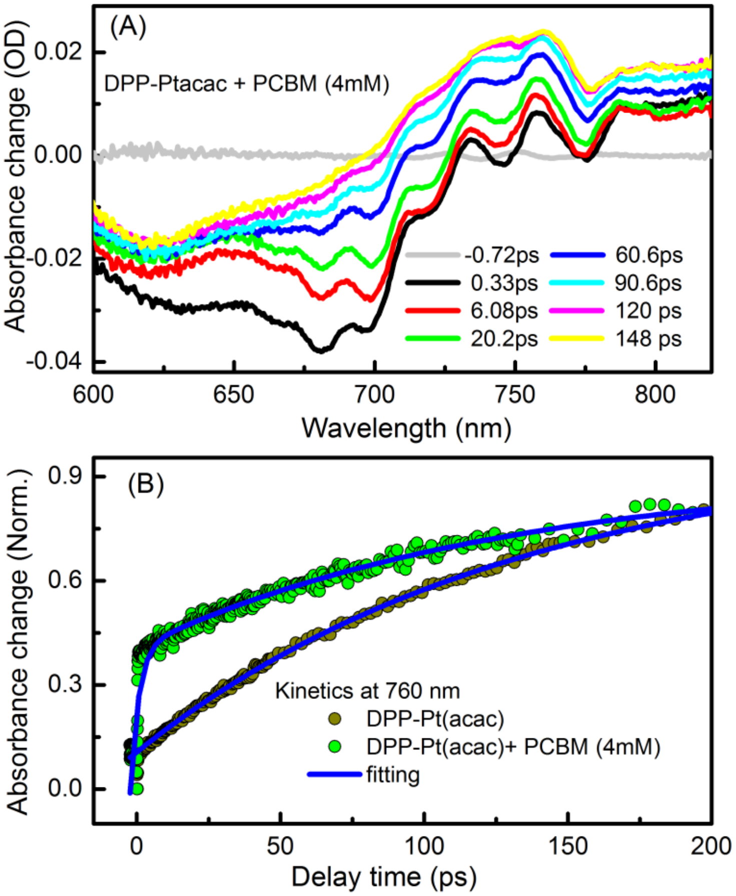

Figure SB.5(A) Transient Absorption after 570 nm pulse excitation of DPP-Pt(acac) + PCBM[4 mM] and (B) kinetic traces collected at 760 nm in dichloromethane (DCM).

C. List of Publications and Conferences

C1. This thesis is based on the work contained in the following papers:

1. **Alsulami, Q. A**.; Murali, B.; Alsinan, Y.; Parida, M. R.; Aly, S. M.; Mohammed, O. F., Remarkably High Conversion Efficiency of Inverted Bulk Heterojunction Solar Cells: From Ultrafast Laser Spectroscopy and Electron Microscopy to Device Fabrication and Optimization. *Advanced Energy Materials* **2016,** *6* (11), 1502356.

2. **Alsulami, Q. A**.; Aly, S. M.; Goswami, S.; Alarousu, E.; Usman, A.; Schanze, K. S.; Mohammed, O. F., Ultrafast Excited-State Dynamics of Diketopyrrolopyrrole (DPP)-Based Materials: Static versus Diffusion-Controlled Electron Transfer Process. *Journal of Physical Chemistry C* **2015,** *119* (28), 15919-15925.

3. Aly, S. M.; Goswami, S.; **Alsulami, Q. A.**; Schanze, K. S.; Mohammed, O. F., Ultrafast Photoinduced Electron Transfer in a π-Conjugated Oligomer/Porphyrin Complex. *The Journal of Physical Chemistry Letters* **2014**, 5 (19), 3386-3390.

C2. Another paper contribution:

1. Ghada H. Ahmed, Manas R. Parida, Alberto Tosato, Lina G. AbdulHalim, Anwer Usman, **Qana A. Alsulami**, Banavoth Murali, Erkki Alarousu. Osman M. Baker and Omar F. Mohammed., The impact of electrostatic interactions on ultrafast charge transfer at Ag29 nanoclusters-fullerene and CdTe quantum dots-fullerene interfaces. *Journal of Materials Chemistry C*, **2016**, 4, 2894-2900.

C3. CONFERENCES

1. Qana Alsulami et al., **(Poster Presentation)**. Remarkably High Conversion Efficiency of Inverted Bulk Heterojunction Solar Cells: From Ultrafast Laser Spectroscopy and Electron Microscopy to Device Fabrication and Optimization. European material research society (e-MRS) fall meeting, Warsaw, Poland, September **2016**.

2. Qana Alsulami et al., **(Poster Presentation)**. Ultrafast Excited-State Dynamics of Diketopyrrolopyrrole (DPP)-Based Materials: Static versus Diffusion-Controlled Electron Transfer Process. Collaborative Conference on 3D and Materials Research (CC3DMR), Incheon/Seoul, South Korea, June **2016**.

3. Qana Alsulami et al., **(Poster Presentation).** Solar cell: Ultrafast Charge Separation in Polymer/Fulleren systems. KAUST Solar Future Symposium, Thuwal, Saudi Arabia, October **2015**.